Ultrafast Microfluidic Immunoassays towards Real-time Intervention of Cytokine Storms

By

Yujing Song

A dissertation submitted in partial fulfillment
of the requirements for the degree of
Doctor of Philosophy
(Mechanical Engineering)
in the University of Michigan
2020

Doctoral Committee:

Professor Katsuo Kurabayashi, Chair
Professor Jianping Fu
Assistant Professor Yongqing Li
Assistant Professor Benjamin H. Singer
Professor Muneesh Tewari

Yujing Song

yujing@umich.edu

ORCID iD: 0000-0003-1448-3069

Acknowledgements

Writing a Ph.D. thesis is truly a gratitude time for me to sincerely thank all the support and people around me in the past six years which probably one of the best periods in my life, during which I won four tennis trophies, ran two full marathons within 3h30m, and was selected as Precision Health Scholar at U-M. First of all, I want to express my greatest appreciation to my advisor and life-long mentor, Prof. Katsuo Kurabayashi for his guidance and support during my entire graduate school time. In Dr. Kurabayashi's lab, I got a chance to have amazing collaborations with clinical doctors and researchers and was able to apply my engineering research to the "Front Line" of saving patients' lives during the global pandemic period COVID-19 which I can never imagine to have in other places. I was deeply influenced by Dr. Kurabayashi's strong emphasis on encouraging free discoveries in the lab, respecting student's ideas, and cultivating the student's leadership to drive their projects. I enjoyed my time in his office when we brainstormed research ideas for the next step or future proposals on his whiteboard. In addition, I would like to thank all my committee members: Profs. Muneesh Tewari, Jianping Fu, Benjamin H. Singer, and Yongqing Li for all the valuable discussions and inputs for my research. A phone call with Dr. Singer every day during the COVID-19 period to discuss the patient's data and conditions is one of the most memorable times for me. I would like to thank all my clinical collaborators: Profs. Sung Won Choi, Monalisa Ghosh, David Frame, Lenar Yessayan, David Humes, Drs. Scott Denstaedt, Erin Sandford, Yuzi Tian, Christopher Flora.

Secondly, I would like to express my strong gratitude to my exceptional lab mates and fellow-students for their great guidance and support. These people are: Drs. Pengyu Chen, Meng-

Ting Chung, who are both my mentors for overall research; Dr. Robert Nidetz, who is my mentor for the cleanroom fabrication; Drs. Young Geun Park, Bo-Ram Oh, Byunghoon Ryu, Mengxi Wu, Andrew Kozminski; Ms. Christina Rice; Mr. Brian Berger, Andrew Stephens, Nicolas Mesyngier. Lastly, many thanks to Mr. Keisuke Goto, Qingtian Yin, Shiuan-Haur Su, and outstanding undergraduate students: Zelin Linghu, Zhenhui Liu, Jingyang Zhao, Tao Cai, Yuxuan Ye who spent days and nights with me in the lab to make our device work!

Thirdly, I would like to thank all the friends around me, amazing undergraduate students in the heat transfer class that I was GSI for, and those tennis leagues that I played for: USTA, KOTEF, Overseas Chinese tennis clubs in Ann Arbor and Novi. I strongly believe tennis and research are the "game changers" of my life. Without them, Ann Arbor would just be a long cold winter place in my memory. I also feel thankful for my funding resources like U-M Precision Health, Cancer Research Institute, NSF, and NIH.

Finally, it is time for me to express my deepest love and thank to my parents Baomin Song, Jing Lyu, and my girlfriend/fiancee Tianying Lan. Their unconditional support is my greatest motivation to pursue a Ph.D. degree and make up my mind being on the frontline to fight against COVID-19 pandemic. My mom, Jing, who used to be the frontline head nurse back in 2003 for SARS patients in Beijing, is the role model that I am truly proud of. She provided me with valuable knowledge and experience on personal protection in handling COVID-19 patient samples. She, together with Dr. Min-Sheng Su (my labmate Shiuan-Haur's dad) shipped us crucial protection gears overseas. My girlfriend Tianying, my life-long soulmate, who accompanies me with love, understanding, and patience, is my strongest support to face any obstacles in my life.

Thank you all very much!

Table of Contents

List of Figures

monoclonal anti-CitH3 antibody (Ab) for neutralization of circulating CitH3 (double block, right panel) can suppress PAD-CitH3 pathway and promote survival. TLR: Toll-like receptor; MPO: Myeloperoxidase; MyD88: Myeloid differentiation primary response gene 88; WT: wild type; KO: Knockout. -p.148

List of Tables

List of Appendices

Abstract

Biomarker-guided precision medicine holds great promise to provide personalized therapy with a good understanding of the molecular or cellular data of an individual patient. However, implementing this approach in critical care uniquely faces enormous challenges as it requires obtaining "real-time" data with high sensitivity, reliability, and multiplex capacity near the patient's bedside in the quickly evolving illness. Current immunodiagnostic platforms generally compromise assay sensitivity and specificity for speed or face significantly increased complexity and cost for highly multiplexed detection with low sample volume. This thesis introduces two novel ultrafast immunoassay platforms: one is a machine learning-based digital molecular counting assay, and the other is a label-free nano-plasmonic sensor integrated with an electrokinetic mixer. Both of them incorporate microfluidic approaches to pave the way for near-real-time interventions of cytokine storms.

In the first part of the thesis, we present an innovative concept and the theoretical study that enables ultrafast measurement of multiple protein biomarkers (<1 min assay incubation) with comparable sensitivity to the gold standard ELISA method. The approach, which we term "pre-equilibrium digital enzyme-linked immunosorbent assay" (PEdELISA) incorporates the single-molecular counting of proteins at the early, pre-equilibrium state to achieve the combination of high speed and sensitivity. We experimentally demonstrated the assay's application in near-real-time monitoring of patients receiving chimeric antigen receptor (CAR) T-cell therapy and for longitudinal serum cytokine measurements in a mouse sepsis model.

In the second part, we report the further development of a machine learning-based PEdELISA microarray data analysis approach with a significantly extended multiplex capacity using the spatial-spectral microfluidic encoding technique. This unique approach, together with a convolutional neural network-based image analysis algorithm, remarkably reduced errors faced by the highly multiplexed digital immunoassay at low analyte concentrations. As a result, we demonstrated the longitudinal data collection of 14 serum cytokines in human patients receiving CAR-T cell therapy at concentrations < 10pg/mL with a sample volume < 10 μL and 5-min assay incubation.

In the third part, we demonstrate the clinical application of a machine learning-based digital protein microarray platform for rapid multiplex quantification of cytokines from critically ill COVID-19 patients admitted to the intensive care unit. The platform comprises two low-cost modules: (i) a semi-automated fluidic dispensing module that can be operated inside a biosafety cabinet to minimize the exposure of technician to the virus infection and (ii) a compact fluorescence optical scanner for the potential near-bedside readout. The automated system has achieved high interassay precision (~10% CV) with high sensitivity (<0.4pg/mL). Our data revealed large subject-to-subject variability in patient responses to anti-inflammatory treatment for COVID-19, reaffirming the need for a personalized strategy guided by rapid cytokine assays.

Lastly, an AC electroosmosis-enhanced localized surface plasmon resonance (ACE-LSPR) biosensing device was presented for rapid analysis of cytokine IL-1β among sepsis patients. The ACE-LSPR device is constructed using both bottom-up and top-down sensor fabrication methods, allowing the seamless integration of antibody-conjugated gold nanorod (AuNR) biosensor arrays with microelectrodes on the same microfluidic platform. Applying an AC voltage to

microelectrodes while scanning the scattering light intensity variation of the AuNR biosensors results in significantly enhanced biosensing performance.

The technologies developed have enabled new capabilities with broad application to advance precision medicine of life-threatening acute illnesses in critical care, which potentially will allow the clinical team to make individualized treatment decisions based on a set of time-resolved biomarker signatures.

Chapter 1

Introduction

1.1 Introduction and Research Background

1.1.1 Cytokines: Key Clinical Targets.

The immune system provides a critical mechanism for a living organism to protect itself against invasions of external pathogens due to bacterial and viral infections. Despite the conceptually clear role of the immune system, pathways underlying the defense mechanism are so complex and yet to be fully understood. The complexity of the immune defense system originates from dynamic functional interactions between biomolecules, cells, and organs over time. Among these players, cytokines are key biomolecules acting as mediators and modulators of the complex functional interactions and responses of the immune system (Figure 1.1) (1-3). They are soluble low-molecular-weight proteins secreted by immune cells and responsible for the regulation of host defense, tissue homeostasis, cell-to-cell communication, and inflammatory reaction. A tightly regulated balance of physiological actions between pro-inflammatory and anti-inflammatory cytokines is critically necessary to maintain the optimal immunity function. Systemic inflammation, which can be clinically manifested in various forms, including systemic inflammatory response syndrome (SIRS), sepsis, acute respiratory distress syndrome (ARDS), and auto-immune disorders (e.g., systemic lupus erythematosus), results from excessive production of

pro-inflammatory cytokines, such as IL-6 and TNF-α. These highly inflammatory responses are counteracted by certain anti-inflammatory cytokines, including IL-10, transforming growth factor (TGF-β), and IL-4, which attempt to restore immunological equilibrium. The multifaceted roles of cytokines in maintaining the tightly regulated balance of immunity have attracted enormous clinical interest in quantification of these biomolecules and its application for infectious disease treatment and drug development (4). Previous studies suggest that quantification of cytokine-based immune fingerprints provides a more accurate way of stratifying and diagnosing bacterial infections than conventional methods based on symptoms, initial clinical observations, and basic laboratory markers (5, 6).

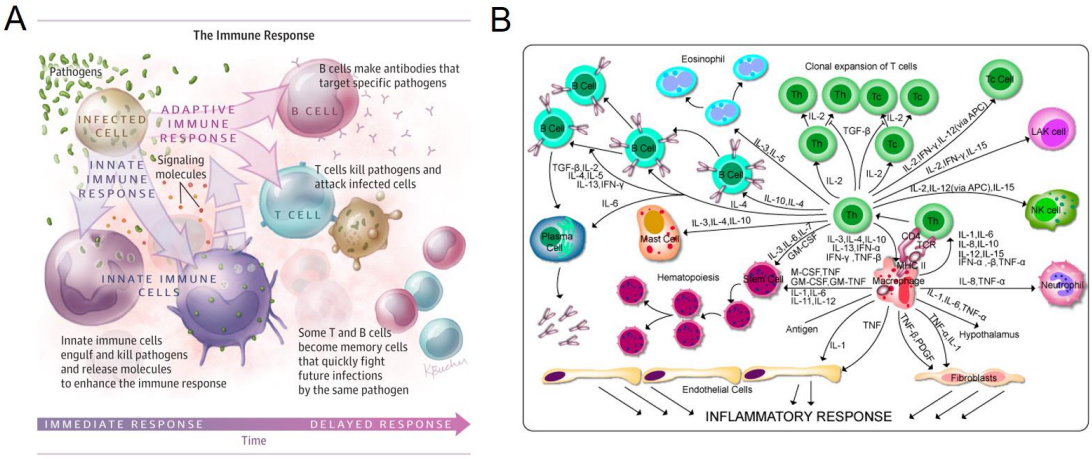

Figure 1.1 (A) Dynamic immune cellular response under pathogen attacks into the immune system. *http://jama.jamanetwork.com/article.aspx?articleid=2279715*. (B) A complex cytokine communicating network while addressing inflammatory response. *www.genecopoeia.com, Data Source: KEGG, BioCarta*

There has been an explosion in the use of immunotherapies for treating autoimmune diseases, infection (7), cancer (8), and other immune-related deficiencies (9, 10). Among these therapies, cytokine-targeted methods aiming to establish a normal balance of the cytokine network in the host have shown great promise for some inflammatory diseases, such as rheumatoid arthritis and Crohn's disease (11, 12). More recently, with the emerging global pandemic of the new coronavirus, COVID-19, FDA has approved the use of IL-6 receptor blocking antibodies, such as

tocilizumab (Actemra), sarilumab (Kevzara), and siltuximab (Sylvant) that are FDA approved for treating various pro-inflammatory conditions manifested by hospitalized critically ill patients with COVID-19-induced hypoxia (13). Quantifying cytokines secreted by isolated immune cells or circulating cytokines in whole blood allows immune responses to be monitored, providing clinically and immunologically useful information related to infectious diseases, cancer, autoimmune diseases, allergy transplantation, and drug discovery (14). Multiplexed detection of different cytokines in a single sample has been proven powerful for obtaining a more complete picture of immunity owing to the highly networked nature of their functions (15). A recent clinical study reveals that among 41 COVID-19 patients with pneumonia with abnormal findings on chest CT, distinctly higher plasma levels of 8 cytokines: IL-2, IL-7, IL-10, GSCF, 1P10, MCP1, MIP1A, and TNF-□ were observed for critically ill patients admitted to an intensive care unit (ICU) than for moderately ill non-ICU patients (16). This finding suggests that multiplexed detection of these cytokines may provide key information to precisely stratify patients and predict the trajectory of their illness levels, thus guiding efficient usages of limited resources of the ICU.

1.1.2 Current Challenges to Precision Medicine in Critical Care of Acute Illness.

Barack Obama, the former President of the United States, advocated scientific approaches to improving human health in his official statement in 2015 (17). Under his leadership, the country announced a research initiative to promote progress toward a new era of precision medicine. Precision medicine provides prevention and treatment strategies that take individual variability into account, based on large-scale biologic databases, such as proteomics, metabolomics, genomics, diverse cellular assays, and even mobile health technology, and computational tools for analyzing large sets of data. Cancer diagnosis/oncology is the medical field that has seen great benefits from the precision medicine approach since the research initiative. Researchers have

sought after the aspirational goal of distinguishing and treating highly specific biologic alterations in cancer, such as specific aberrations in gene structure or regulation, transcription, or post-transcription molecular pathways, to realize personalized therapy and improved outcomes. For example, Piccart-Gebhart et al. (18) demonstrated improved outcomes of breast cancer chemotherapy by using a monoclonal antibody, Trastuzumab, which targets the single gene mutation in the human epidermal growth factor receptor 2 (HER2) gene in breast cancer cells. Multiple other breakthroughs and innovations in diagnosis and treatment targeted to specific abnormalities have extensively benefitted patients with cancer (19, 20). Thus, a rosy future of precision medicine is foreseen with the successful completion of the Human Genome Project (21) and molecular subtyping of melanoma on BRAF, RAS, and NF1 mutations (22).

By contrast, it is notable that critical care medicine has not yet seen a tangible fruit of the precision medicine approach. Patients with acute, critical illness constitute a large and growing portion of healthcare consumers in the United States, driving over $80 billion in expenditures and over 13% of hospital costs (23). Despite the costs, morbidity and mortality of critical illness, however, many of the illnesses cared for in the intensive care unit (ICU) remain poorly defined without clear disease-specific therapies (24, 25). Apparently, major barriers to precision medicine exist in critical care. While testing and therapeutic plans for cancers and other chronic diseases are formulated over days to weeks, life-saving treatment for critically ill patients must be delivered in minutes to hours. The need for generating phenotype data that are adequately timely for a group or cluster of patients with the complexities of multi-morbidity poses significant challenges to implementing precision medicine in critical care. Additionally, without particular patterns of gene expression or biomarker profiles guiding therapies with a precise prediction of the trajectory of life-threatening illness, the current approach is forced to “passively” treat patients only when their

symptoms become obviously worsen. Such delays prohibit clinical interventions to prevent the development of organ failure and even mortality in the early stage of the illness. With molecularly targeted therapeutics failed, the field of critical care medicine now recognizes an urgent need for novel clinical trials designed to embrace and explore the heterogeneity of treatment during phases 2 and 3 (24, 25). The implementation of precision medicine in critical care surely requires a close partnership between medicine and engineering to provide innovative approaches leading to reduced costs, increased timeliness of patient screening and treatment, and facilitated data sharing.

1.1.3 Rapid, Sensitive, Accurate Biomarker Analysis.

One of the major factors leading to the aforementioned barriers is the lack of technologies permitting the timely and accurate acquisition of phenotypical and pathological data of patients. For example, the gold standard for the diagnosis of sepsis – a life-threatening illness caused by the body's response to an infection – has traditionally been a combination of physiologic vital signs and organ-specific blood parameters coupled with microbial cultures to identify the presence of sepsis and source of infection(26). However, a positive culture can take over 48 hours to incubate, and false-negative results are common due to the low density of blood bacteria at the early stage of infection. Other methods based on nucleic acid amplification also require a sample-to-answer time as long as 4–10 hours, and these often suffer poorer sensitivity and specificity than microbial cultures(27). A promising alternative method is sampling and analysis of blood circulating protein biomarkers that serve as inflammatory-based surrogate indicators of infection-induced inflammation, such as cytokines (28, 29).

Proteins in circulating blood often provide valuable biological signatures for disease diagnosis. Immunoassays are powerful techniques for protein biomarker analysis. They take advantage of the ability of an antibody developed by nature to recognize and bind a specific protein existing in a

complex mixture of macromolecules. The enzyme-linked immunosorbent assay (ELISA) is the gold standard biomarker detection method widely used in clinical diagnosis because of its high sensitivity and selectivity, but it generally lacks the speed to provide timely data for critical care. Continuing efforts have been undertaken to develop ultrafast immunoassays by employing methods, such as assay step simplification (30), label-free biosensing (31-35), surface-to-volume ratio enhancement (36-38), active protein mixing (39, 40) and molecular pre-concentration (41, 42). However, if a rapid assay is achieved with a reduced assay incubation time, the measurement normally experiences poor sensitivity. For a system with weak antigen-antibody affinity, where the protein binding kinetics is solely limited by the surface reaction rate (reaction limited regime(43)), there is no effective way to shorten the assay time using the aforementioned methods involving active mass transport enhancement by mixing, pre-concentrating, and miniaturizing. Additionally, the other methods become impractical owing to increased complexity and extensiveness required for nanomaterial synthesis, fabrication, and integration. The absence of a rapid immunoassay with high sensitivity prohibits the acquisition of the patient's accurate "real-time" biomarker profile information, which is critically needed for precision treatment of acute illnesses. Existing immunoassay methods also suffer other impediments, including limited multiplexity, the inability to deliver a near-bedside result, and increased complexity and cost resulting from sophisticated micro/nanofabrication or circuit designs for reagent mixing and pre-concentration. All together, these limitations pose major obstacles towards fulfilling the promise of biomarker-guided precision medicine in critical care.

1.2 Motivation and Objectives

The absence of rapid, sensitive, and accurate diagnostic methods renders treatment of critically ill patients highly empirical with no access to information allowing individualized selection and

use of appropriate drugs (44). Indeed, several review papers suggest that the failure of therapy could be attributed to the lack of appropriate techniques to monitor circulating blood biomarkers and host defense responses across highly heterogeneous patient cohorts during the course of disease development (45-49). The current technological gap prohibits the acquisition of the patient's accurate "real-time" biomarker profile information, which is critically needed for precision treatment of acute illnesses. This research is motivated by the urgent need for a new diagnostic tool for the timely personalized treatment of life-threatening acute illnesses.

Although critically important biomarkers, such as cytokines, may have high concentrations in tissues, their concentrations in the circulation may be low, requiring *sensitive* and *robust* measurement in addition to speed. Additionally, approaches to precision medicine in critical illness must be *flexible*. While assays for some biomarkers, such as the cardiac troponin in myocardial infarction (MI), have been refined over decades after obtaining gold-standard evidence of their importance, our understanding of biomarkers in complex, heterogeneous conditions in critical illness is undergoing rapid evolution (50). The high cost and difficulty of generating appropriate assays may lead to a stalemate in precision medicine for acute care: in the absence of validated biomarker-driven treatments, there is little market for new assays – but the absence of practical assays prohibits the clinical trials needed to study new treatments. In order to facilitate prospective clinical trials of biomarker-driven therapy, measurement technologies that can rapidly and inexpensively adapt to new analytes are needed. To meet these unmet needs, this thesis work aims to develop a novel immunoassay biosensor platform that enables near-the-patient concurrent quantification of circulating blood cytokine biomarkers.

This work is also motivated by the need for fundamental engineering knowledge. To fully understand the physics that determines the speed and sensitivity of biomarker analysis, this thesis

develops multi-physics models accounting for protein mass transport (forced convection and diffusion), protein surface reaction and binding kinetics, and biosensing signal transduction. These models guide us for the optimization of new rapid, sensitive immunoassay biosensing approaches that involve quenching pre-equilibrated antigen-antibody immune complex formation events, counting single-molecule digital signals, and label-free plasmonic protein biosensing with electrokinetically enhanced protein mass transport and surface binding. The models also provide a theoretical foundation of the scientific validity of our newly developed assay strategies. These strategies are theoretically validated for the biosensing performance that fully meets the stringent requirements for biomarker-guided timely and accurate personalized diagnosis and treatment of life-threatening acute illnesses. With the theoretically guided optimization, one of the biosensor technologies presented in this thesis achieves cytokine biomarker analysis at unprecedented levels of detectability with a limit of detection (LOD) of ~1 pg/mL (50fM) and speed leading to a sample-to-answer time of < 5 min. Another developed technology provides a maximum sensor response speed that can be fast enough to shorten the assay reaction incubation time as short as 30 sec, which is more than 200 times shorter than that of the conventional ELISA gold standard technique. Careful engineering design could achieve the system cost more than 10 times less than that of a bulky high-end system incorporating a fully automated robotic machine for sample/reagent handling (51).

Ultimately, the biomarker detection capability demonstrated in this thesis needs to be translated into wide clinical use to tailor the biomarker-targeted immunomodulatory therapy. Here, this study is motivated to develop biosensor systems that can serve as a broadly used technological platform to determine the optimal treatment approach and drug administration timing for a wide spectrum of severe life-threatening illnesses, such as sepsis, cytokine release syndrome (CRS), acute

respiratory distress syndrome (ARDS), systemic inflammatory response syndrome (SIRS), myocardial infarction (MI), post-cardiac arrest syndrome (PCAS), and trauma-induced acute immune disorders. The ability to achieve comprehensive real-time profiling of circulating blood biomarkers may open the door to novel clinical trials. In addition, the technology should find wider use owing to its general applicability to assays involving receptor-analyte interactions. The receptor types used in this technology may be further extended to a wide variety of antibodies, peptides, and oligonucleotides. This will allow this technology to be implemented for other biological assays than cytokine profiling, such as protein biomarker analyses, receptor-ligand assays, enzyme assays, and DNA assays. Thus, the technology will serve as a general and powerful tool in protein expression profiling, gene expression analysis, molecular-level analysis of infectious diseases, and human leukocyte antigen (HLA) testing.

1.3 Scopes of the Thesis

This thesis perceives the technological gap described above as an exciting opportunity for engineering researchers. A new cytokine biosensor technology filling the gap promises to advance precision medicine of life-threatening acute illnesses in many ways. For example, this will provide the time-changing profile of a panel of cytokine biomarkers in the patient in real-time and allow clinicians to determine precisely the timing, frequency, and dose of the drug specifically targeting the pathological origin. Here, the cytokine biosensor will play a pivotal role in the feedback system tightly regulating the delicate balance of cytokine levels within the immune system (Figure 1.2). For sepsis alone, establishing such a biosensor-enabled approach to feedback immune system control will save more than 250,000 lives a year in the U.S. In light of this vision, this research aims to develop novel biosensor systems enabling near-patient, real-time cytokine profiling with high seep, sensitivity, accuracy, and multiplexity while keeping the assay cost low. Towards this

end, this thesis work establishes two approaches termed: (1) the "pre-equilibrium digital enzyme-linked immunosorbent assay (PEdELISA) and (2) the "AC electroosmosis-enhanced localized surface plasmon resonance (ACE-LSPR) biofunctional nanoparticle imaging."

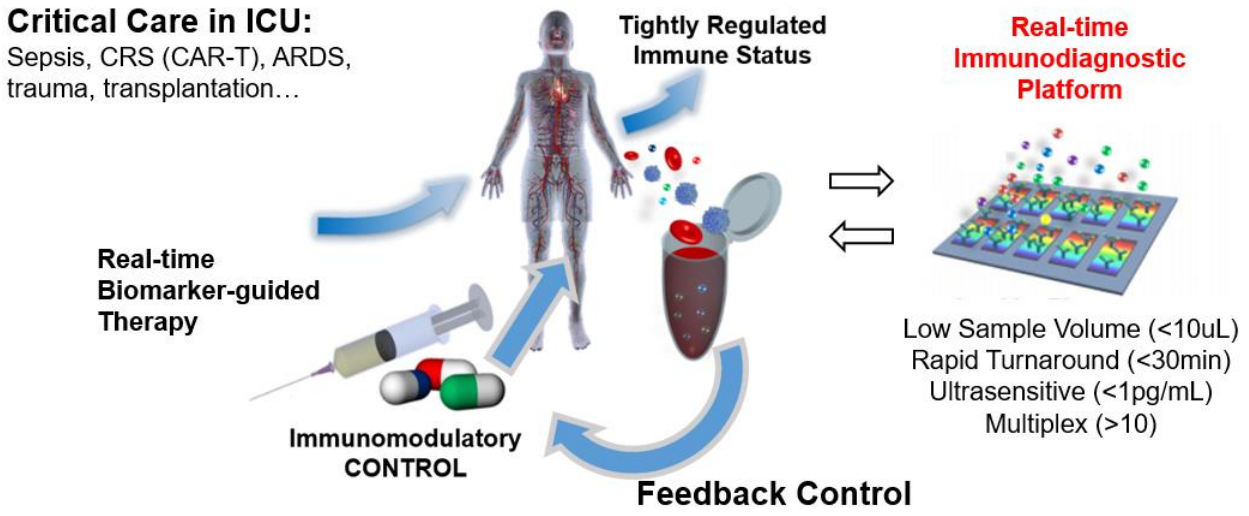

Figure 1.2 Concept of personalized immunomodulatory therapy for systemic inflammatory disease enabled by rapid cytokine-based immune status monitoring. This concept is analogous to feedback-loop system control theory used in system engineering that controls the behavior of a dynamical system with an input.

The PEdELISA method is a digital immunoassay based on single-molecule counting of antigen-antibody immune complexes at an initial state of their formation far from equilibrium, namely a "pre-equilibrium state," for cytokine biosensing. Digital immunoassay is an emerging technique for biochemical analysis of analytes in low abundance. Its single-molecule sensitivity originates from binary counting of On/Off signals amplified within various types of small sub-volume partitions (52-55). Conventional digital immunoassays typically require a long incubation time (hours) to ensure a sufficiently high signal-to-noise ratio for sub-fM detection (56, 57). In contrast, our approach applies single-molecule counting within a short (30-600s) incubation time for a system in which analyte molecules exist more abundantly by capturing a snapshot of pre-equilibrated reaction at its very early stage. The snapshot approach significantly extends the

digitally quantifiable range from fM to clinically relevant sub-nM, which is conventionally believed to be far outside the range permitted by single-molecule binary counting. PEdELISA is capable of achieving a sandwich immunoassay even for a system at the reaction limit regime nearly as fast as point-of-care glucose or pregnancy tests while retaining the regular ELISA-grade sensitivity. Here, the single-molecule counting condition is achieved by intentionally quenching the immunologic reaction.

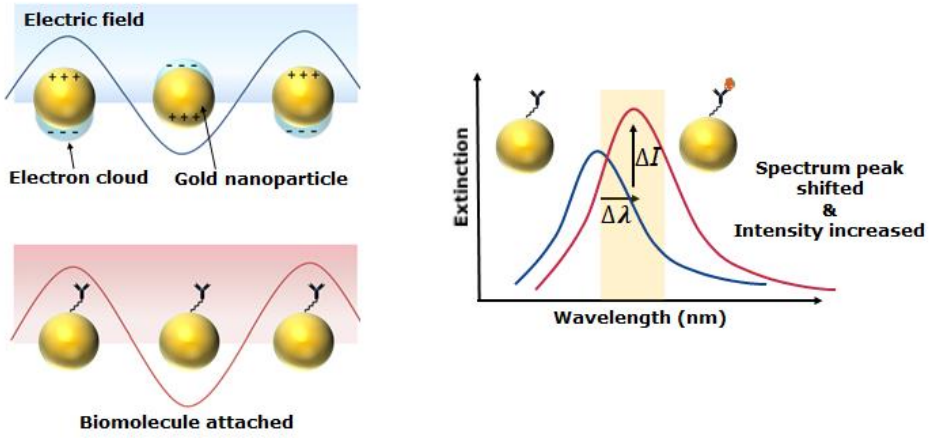

Figure 1.3 Principle of nanoparticle/nanostructure-based localized surface plasmon resonance.

In the ACE-LSPR biofunctional nanoparticle imaging technique, we employ a label-free gold nanorod (AuNR) plasmofluidic device coupled with AC electroosmosis (ACEO)-driven analyte flow. The device overcomes the physical barrier of the conventional diffusion-limited biosensors, thus achieving unprecedented sensing performance. Over the past years, researchers have perceived localized surface plasmon resonance (LSPR)-based biomolecular binding assay as an emerging biochemical analysis technique. In LSPR, metal nanoparticles/nanostructures in sub-wavelength size are excited by an external light source to generate surface plasmons in a localized space (Figure 1.3). Surface binging of analyte molecules onto the nanostructures yields a shift of the resonance in the plasmon-photon coupling. The resonance shift allows LSPR biosensors to

quantify the analyte concentration. This technique holds the great potential to replace current gold standard assay (e.g., ELISA) in real clinical applications because of its much more simplified procedure eliminating multiple laborious assay processes and sample sparing capability. However, such an assay still falls short of meeting speed and sensitivity urgently required for critical care medicine. To overcome these limitations, this thesis demonstrates an innovative bioanalytical method of coupling ACEO-enhanced analyte transport and analyte-receptor interactions with biofunctional nanoparticle imaging. This study theoretically and experimentally proves that the electrohydrodynamic enhancement can significantly improve nanoparticle-based plasmofluidic analyte detection capability and shows the promise of label-free LSPR biosensing as a powerful biochemical analysis approach to low-abundance biomarker detection.

1.4 Thesis Outline

Based on the research scope discussed above, this thesis consists of six subsequent chapters as follows:

Chapter 2 - Literature review: This chapter reviews the studies relevant to this thesis which mainly focus on ultrafast multiplex immunoassay technique towards near-bedside operation. After briefly introducing the gold standard immunoassay technology, the first part reviews the current advances of microfluidic cytokine immunoassay devices, and then the second part discusses the ultrasensitive single-molecule digital counting assays. Lastly, label-free nano-plasmonic immunoassay was reviewed and the current limitation is summarized.

Chapter 3 - Rapid Single-molecule Digital Detection of Protein Biomarkers for Near-real-time Monitoring of Systemic Immune Disorders: This chapter presents an innovative concept that enables near real-time measurement of multiple protein biomarkers (<1 min assay incubation) with comparable sensitivity to the gold standard ELISA method. The approach, which we term

"pre-equilibrium digital enzyme-linked immunosorbent assay" (PEdELISA) incorporates the instantaneous single-molecule digital counting of pre-equilibrium protein binding events to simultaneously realize speed and sensitivity. Here, we developed a theoretical model to validate that the 2-step transient assay format of PEdELISA can maintain a linear relationship between the analyte concentration and the assay readout regardless of the reaction time and predicted the minimum required incubation time for a desired detection limit. We also experimentally demonstrated the assay's application in near-real-time monitoring of protein biomarkers in patients manifesting post-chimeric antigen receptor (CAR) T-cell therapy cytokine release syndrome (CRS) with ~30 min serum sample to answer time and the longitudinal serum cytokine measurement in a mouse septic model.

Chapter 4 - Machine Learning-Based Cytokine Microarray Digital Immunoassay Analysis: This chapter further presents the development of a highly multiplexed microfluidic PEdELISA platform by incorporating both spatial-spectral microfluidic encoding and machine learning-based autonomous image analysis. This unique approach remarkably reduces errors facing the high-capacity multiplexing of digital immunoassay at low protein concentrations. As a result, the assay has achieved 16-plexed biomarker detection at concentrations < 10pg/mL with a sample volume < 10 μL, including all processes from sampling to data analysis within 30 min, while only requiring a 5-min assay incubation. Longitudinal data obtained for a panel of 14 serum cytokines in human patients receiving CAR-T cell therapy reveals the powerful biomarker profiling capability

Chapter 5 - An Automated Microarray Digital Assay towards Near-Realtime Personalized Intervention of Cytokine Storm among COVID-19 Patients: This chapter demonstrates the application of an automated machine learning-based PEdELISA platform for realtime multiplex quantification of cytokines from severe COVID-19 patients admitted to the ICU at the University

of Michigan Hospital. The low-cost automated platform comprises a 2-part module: an automated fluidic dispensing/mixing module that operates inside the biosafety cabinet to minimize the exposure of technician to the virus infection, and a 12-12-15 inch compact fluorescence optical scanner for the potential near-bedside operation. The PEdELISA platform enabled daily cytokine profiling with: high sensitivity (<0.4pg/mL), interassay precision (~10% CV), and near-realtime turnaround (10min assay incubation, ~30min total). A cytokine profiling test allowed us to observe clear interleukin -6 (IL-6) elevations after receiving tocilizumab (IL-6 inhibitor) while significant cytokine profile variability exists across all critically ill COVID-19 patients and to discover a weak correlation between IL-6 to clinical biomarkers, such as Ferritin and CRP.

Chapter 6 - AC Electroosmosis-enhanced Nano-plasmofluidic Detection of Ultra-low-Concentration Cytokine: In this chapter, we present a label-free nano-plasmofluidic device integrated with microelectrodes for rapid analysis of a low-abundance cell signaling protein, detected by AC electroosmosis-enhanced localized surface plasmon resonance (ACE-LSPR) biofunctional nanoparticle imaging. Applying an AC voltage to microelectrodes for active mixing while scanning the scattering light intensity variation of the nano-plasmonic biosensors results in significantly enhanced assay performance.

Chapter 7 - Conclusions and Future Work: The final chapter summarizes the two platforms developed in this thesis: The labeled PEdELISA platform and the label-free ACE-LSPR platform and their application towards near-realtime intervention of cancer immunotherapy, COVID-19 and sepsis induced cytokine storm. In the last section, several ongoing studies are discussed, including the building and translation of a fully integrated and automated PEdELSIA system for near-bedside ICU patients cytokine profiling, the development of a whole-blood assay system, and the application of the PEdELISA platform for real-time septic mouse model treatment.

Chapter 2

Literature Review

This chapter provides a review of previous studies related to this thesis work. The review gives insight into the motivations and applications of our research as well as analysis of competing technologies. This thesis work aims to develop microfluidic cytokine assay platforms achieving the combination of both rapidness and sensitivity. The review has four main sections related to this goal: (1) ELISA immunoassay technology as a gold standard of analytical biochemistry analysis, (2) microfluidic cytokine assay technologies, (3) digital immunoassay platforms, and (4) label-free plasmonic biosensors. Each section details why this review is relevant and discusses multiple previous work that studied the topic. The review will summarize the achievements and limitations of existing work and describe how to address these problems in this thesis work.

2.1 ELISA Immunoassay Technology

Proteins in circulating blood often provide valuable biological signatures for disease diagnosis. Immunoassays are powerful techniques for biomarker analysis. They take advantage of the ability of an antibody developed by nature to recognize and bind a specific protein existing in a complex mixture of macromolecules. The enzyme-linked immunosorbent assay (ELISA) is a widely used analytical biochemistry technique, first demonstrated by Engvall and Perlmann in 1971 (58). Now, this technique is the gold standard biomarker detection method widely used in clinical diagnosis.

The assay detects the presence of antigens in a liquid sample using antibodies specifically binding to them. ELISA is a well-established, well-proved immunoassay technique showing high sensitivity and selectivity, which has been used as a diagnostic tool in medicine, plant pathology, and biotechnology. However, involving sample incubation, detection antibody incubation, and labeling reagent incubation processes as well as multiple washing steps, commercial ELISA kits usually require a minimum assay time (primarily dominated by the incubation time after sample loading) of 3 - 8 hours, bulky optics and instrument in a current centralized clinical laboratory setting, and high assay costs as shown in Table 2.1. Certainly, such limited performances and high costs prohibit their use for critical care medicine that urgently needs cytokine profile data at a low limit of detection (LOD) reaching the 1 -10pg/mL level (59), speed permitting analyte analysis with a sample-to-answer time < 30 min and high frequency of test for continuous monitoring of the patient's immune status.

Table 2.1 Competing immunoassay diagnostic systems (*Total assay time includes analyte quantification, data acquisition, and analysis, but does not include sample preparation. Please also note that the assay and instrument cost of the commercial system is from their market price based on the best knowledge of the author, rather than the actual materials cost.)

Diagnostic System	Cost/96 Assays	Instrument Cost	*Assay Time	LOD (pg/mL)	Sample Volume (μL)	Plexity
Luminex	$3000	>$40,000	> 4 hours	0.1 -100	25-50	25-65
Colorimetric ELISA	$200	$5,000	> 4 hours	1-10	100	1
Quanterix SIMOA	$1000	>$200,000	45 min	0.002 - 1	100	6
PerkinElmer AlphaLISA	$1200	>$200,000	4 hours	1-100	50-100	4
Our Platform in Ch.3, 4, 5	**$50**	**<$5,000**	**< 30 min**	**0.1-5**	**5-10**	**16**

2.2 Microfluidic Cytokine Immunoassay Devices

Modern advances in microfabrication technologies have driven an increasing number of studies to integrate biosensors in a microfluidic platform with sophisticated on-chip fluidic channels, chambers, and valves. The microfluidic environment creates a short sample-to-sensor distance positioning analyte molecules in close proximity to receptors on the sensor surface. It reduces the time required for the molecules to reach the sensor receptors by diffusion. The small volume of the microfluidic environment generates strong convection at a small sample flow rate. The coupling of diffusion and convection in the microfluidic volume enhances analyte transport, and therefore resulting in efficient sample delivery and sample sparing capabilities for cytokine analysis (60).

Researchers have demonstrated several microfluidic immunoassay devices for cytokine analysis as summarized in Table 2.2. Performing cytokine immunoassay in a microfluidic platform leads to highly efficient sample purification, reagent loading, parallel reagent manipulation, parallel signal reading, and multiplexed analyte detection (61, 62). For example, the blood barcode chip reported by Fan et al. (63) demonstrates these advantageous microfluidic features. The chip achieved multiplexed detection of 12 protein biomarkers, including IFN-γ, TNF-α, IL-2, IL-1α, IL-1β, TGF-β1, IL-6, IL-10, IL-12, GM-CSF, MCP-1, and PSA, from 10 μL whole blood samples diluted to 90 μL with buffer (Figure 2.1).

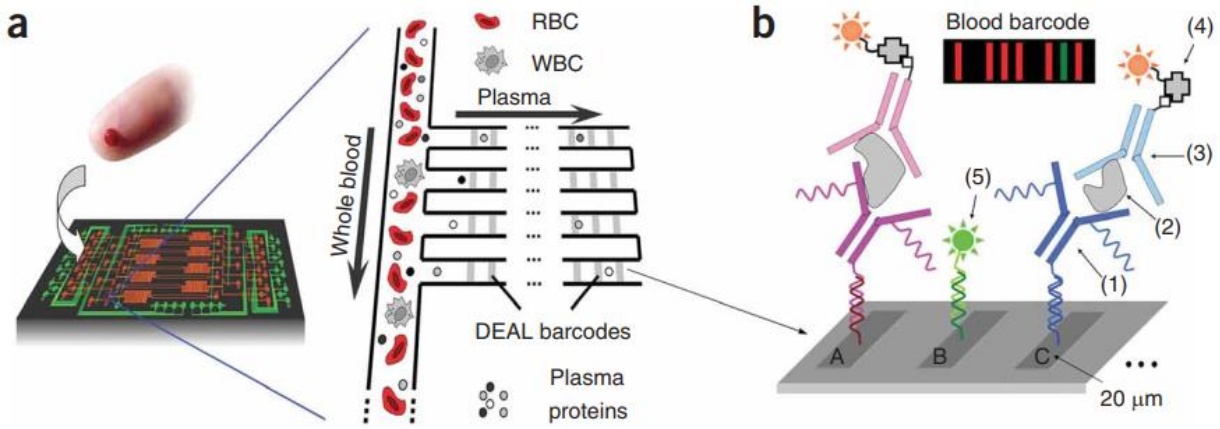

Figure 2.1 Blood barcode chip for microfluidic ELISA assay that involves (A) plasma separation from a finger prick of blood and (B) sandwich immunoassay of plasma proteins on DNA-coded barcode arrays in a microfluidic channel. Adopted from Fan et al. (63).

Table 2.2 Competing microfluidic systems for multiplexed cytokine immunoassay

Microfluidic system and publishing year	Biomarkers (analytes)	Sample type	Incubation Time (IL-6)	LOD (IL-6)	Ref.
Integrated blood barcode chip (2008)	IFN-g, TNF-a, (IL)-2, IL-1a, IL-1b, (TGF)-b1, IL-6, IL-10, IL-12, GM-CSF, (MCP)-1, PSA	Whole blood	> 60 min estimated	~10 pg/mL	Fan et al. (63)
Multiplexed magnetic bead assay (2012)	IL-4, IL-6, TNF-α	Purified buffer (BSA)	10 min 30 min	10 pg/mL 1 pg/mL	Sasso et al. (64)
Microcapillary film (MCF) (2014)	IL-1β, TNF-α, IL-6, IL-12, PSA	Whole blood, serum or buffer	10 min	30 pg/mL	Castanheira et al.(61)
Microfluidic multilayer array (2014)	TNF-a, IL-1b, IL-6, PSA	Human serum	150 min	16 pg/mL	Carcia-Cordero and Maerkl (65)
Microfluidic microarray immunoassays (2014)	IL-6, IL-β, TNF-α, PSA	Purified buffer (BSA)	120 min	43 pg/mL	Volpetti et al. (62)
Microfluidic droplet digital ELSIA (2019)	GM-CSF, IL-6	Human serum	>90 min estimated	0.004 pg/mL	Yelleswarapu et al. (66)
Our platform in Ch. 3, 4, 6	**IL-6, TNF-α, IL-2, IL-8, IL-13, IL-1α, IL-1β, IL-10, IL-12, IL-15, IL-17A, IFN-γ, GM-CSF, MCP-1**	**Human plasma serum, or whole blood**	**1-5 min**	**0.37 pg/mL**	**Song et al. (67)**

However, the biochemical process applied for these devices essentially remains the same as that of the standard ELISA, which involves time-consuming assay steps and an immunocomplex formation incubation process (> 1 hour). To speed up the ELISA analysis, recent studies have significantly cut down the incubation time for analyte biding (i.e., antigen-antibody immune complex formation) on the sensor surface. For example, Sasso et al. (64) demonstrated a commercial multiplexed magnetic bead assay (Luminex) for IL-6, and TNF-α in a microfluidic platform with an incubation time of 10 min. Similarly, Castanheria et al. (61) performed microfluidic ELISA to detect IL-1β, IL-6, TNF-α, and IL-12 simultaneously with an incubation time of 10 min. However, if a rapid assay is achieved with a reduced assay incubation time, the measurement normally experiences poor sensitivity. Although the LOD value found in the literature for the rapid microfluidic immunoassays is ~ 10 pg/mL, it simply means that cytokine levels above the value were considered positives. A low value of LOD is often misdealing, not guaranteeing reliable analyte measurement. The measurement does not guarantee reliable quantification of the analytes. Instead, limit of quantification (LOQ), which is the lower bound for the linear range in which a fold change occurs for the detection signal with the varying analyte concentration, is a better measure of the assay performance. LOQ values are often found to be more than an order of magnitude higher than LOD values for cytokines measured using these rapid microfluidic immunoassay devices (61).

Continuing effort has been undertaken to develop rapid microfluidic immunoassays by employing methods, such as assay step simplification (30), label-free biosensing (31-35), surface-to-volume ratio enhancement (36-38), active protein mixing (39, 40), and molecular pre-concentration (41, 42). However, for a system with weak antigen-antibody affinity, where the protein binding kinetics is solely limited by the surface reaction rate (reaction limited regime (43)),

there is no effective way to shorten the assay time using the aforementioned methods involving active mass transport enhancement by mixing, pre-concentrating, and miniaturizing. Furthermore, implementing active fluid manipulation mechanisms and non-ELISA-based biosensors found in these methods requires their integration into a microfluidic platform using sophisticated micro-/nanofabrication techniques and high-precision operations. This often brings poor repeatability to the measurement.

2.3 Single-Molecule Digital Counting Assays

Digital assays have attracted much attention from the research community with excitement for their ability to detect biomarkers with single-molecule sensitivity. These assays compartmentalize biological samples into millions of femtoliter-volumes and interrogate biochemical reactions individually. One can find a wide use of digital assays as a platform for the ultrasensitive detection of nucleic acids (68-70), proteins (52, 66, 71-75), single cells (76), and single exosomes (77) in the literature. Along with the high sensitivity, digital assays show stability and robustness, which is highly attractive for POC diagnostics. As such, incorporating the digital assay into a microfluidic format has enhanced the performance of immunoassays considerably to fulfill all of the following performance criteria: (i) low limit of detection (LOD, subpicomolar), (ii) high dynamic range (5 orders of magnitude or better), (iii) multiplexed biomarker analysis (4 or more), and (iv) compatible with ultralow volume (<5 μL) samples (78).

The most well established commercial implantation of an ELISA-based digital assay, namely digital ELISA (dELISA), is Quanterix's Simoa (51). However, this commercial system requires very bulky optics and fluid handling components to automate the entire process from sampling to data delivering, which leads to a very high instrumentation cost > $200,000 (see Table 2.1**)**. Some studies have implemented dELISA for cytokine detection with a portable platform

suited for bedside diagnosis. For example, Piraino et al. (78) demonstrated multiplexed detection of 3 different types of anti-Ebola IgG antibody in human serum at concentrations as low as 0.33 pg/mL using an integrated microfluidic chip device. They further developed a portable, low-cost diagnostic system incorporating the chip with an automated fluidic manipulation unit and a digital CMOS camera for POC operation (Figure 2.2). More recently, Yelleswarapu et al. (66) developed a smartphone-connected microfluidic platform for miniaturized dELISA detection of GM-CSF and IL-6 cytokines using parallel droplet generation/detection channels (Figure 2.3). The research team achieved a very low LOD of 0.004-0.007 pg/mL in their measurement. Despite their exciting performance and potential, this platform still requires a relatively long sample incubation time > 60 min, thus leading to a total sample-to-answer time > 2 hours. In general, the conventional digital assays for protein analysis face a similar issue whether they use the bulky commercial instrument or the POC platform. Unfortunately, direct implementation of these assays is not suitable for realizing precision medicine of critical illnesses.

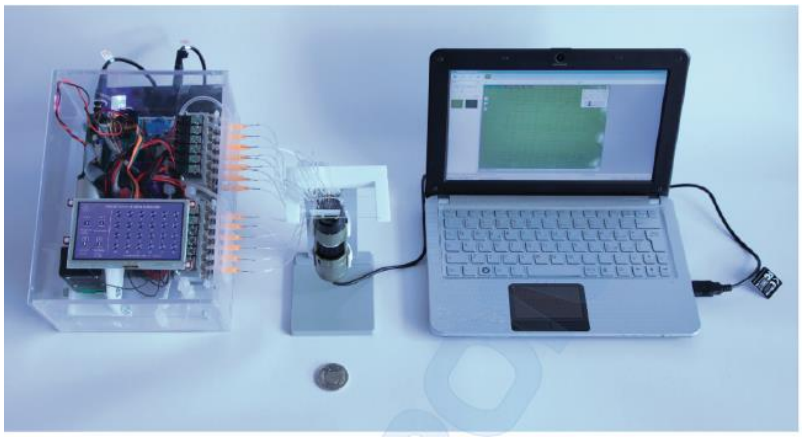

Figure 2.2 Image of the portable diagnostic system consisting of a microfluidic control system (box on the left), a fluoresce USB microscope , a dELISA microfluidic chip (center), and a laptop computer (rignt).Adopted from Piraino et al. (78)

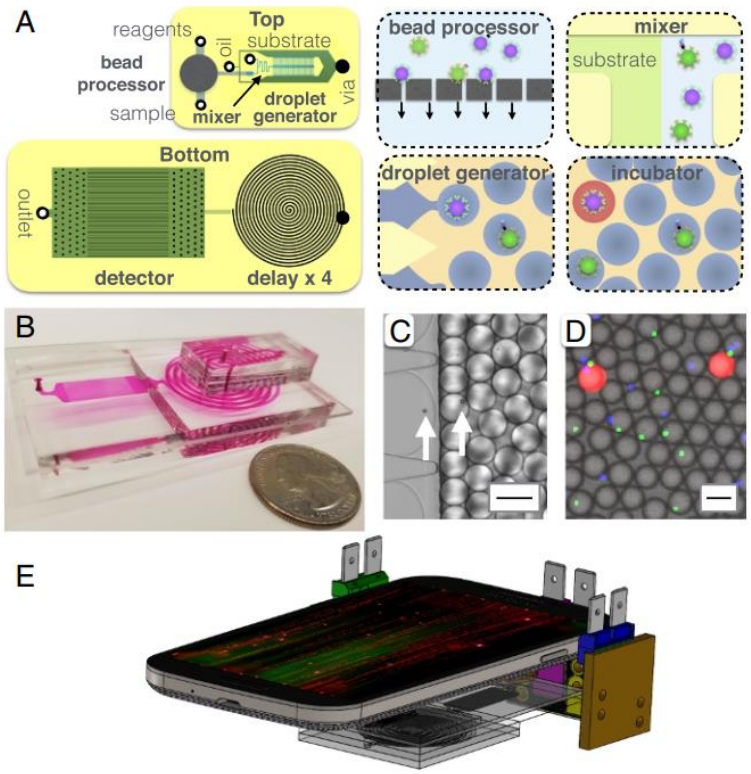

Figure 2.3 Integrated micro droplet dELISA platform. (A) Schematic of the assay chip (top and bottom views) (B) Photograph of the disposable assay chip. (C) Droplet generator encapsulating microbeads. (D) Fluorescence micrograph of the droplets. (E) Schematic of the platform with a mobile phone, three light sources, and the disposable chip. Adopted from Yelleswarapu et al. (66).

2.4 Label-Free Plasmonic Biosensors

Many of immunoassay methods use a fluorescence labeling process involving multiple washing steps prior to the analysis. The fluorescence technique is well established in life sciences but *only* provides the end output of the signal readout. As a result, these methods lack the ability to observe the time-course evolution of antigen-antibody complex formation processes. For this reason, we believe that introducing a label-free, real-time biosensing technique to immune cell function analysis will provide another promising approach to significantly advance scientific knowledge and disease diagnosis techniques.

Label-free biomarker analysis has been performed using various types of sensors, including

mechanical (microcantilever(79), acoustic wave(80), quartz crystal microbalance mass(81)), electrical (electrochemical impedance spectroscopy(82, 83), amperometric detection(83, 84), capacitive affinity detection(85), nanoelectronic field-effect transistors(33, 34, 86), optical (photonic crystal(87, 88), optical resonator(89, 90)), and plasmonic (surface plasmon resonance(91-93), localized surface plasmon resonance (LSPR) (94-99) sensors. Among these label-free sensors, plasmonic biosensors (100-106) are particularly advantageous for point-of-care (POC) measurements.

Over the last decade, plasmonic biosensors were extensively studied for various applications. As mentioned in the previous chapter, the principle of the plasmonic biosensors depends on the interaction of electromagnetic (EM) radiation on a noble metal in contact with surrounding dielectric medium. Coherent oscillations of free electrons near the metal surface called surface plasmons (SPs) resonate with incident excitation light frequency. SPs own the evanescence field at the boundary area between the metal and dielectric region and this field exponentially decays into a dielectric region. The resonance mode of SPs is sensitive to the local refractive index change and this change is induced by the adsorption of biomolecules in the metal-dielectric interface results in the alteration of the resonant condition of SPs. SP-based biosensing is found in two settings: (1) the surface plasmon resonance (SPR) setting, where SPs occur at the interface between a thin metal substrate and a dielectric medium; and (2) the localized surface plasmon resonance (LSPR) setting, where SPs are excited at the surface of subwavelength sized nanoparticle/nanostructure by an external light source (Figure 1.3).

The most widely used plasmonic biosensing technique for biological and chemical analyte detection is label-free SPR biosensing. Especially for the biomolecule sensing (e.g. biomolecule quantification), SPR biosensors can overcome the shortcomings of labeling-based conventional

techniques, such as long sample preparation time, complex processes, and large sample volume requirements, by eliminating tedious labeling processes. However, SPR detection suffers from several fundamental limitations while working as a biomolecule detection sensor due to its Kretschmann arrangement involving a bulky prism, and yielding a longer surface plasmon decay length (δ_d) than the LSPR technique. This SPR arrangement hinders sensor miniaturization and integration with other functional systems, such as point-of-care devices. Moreover, the longer surface plasmon decay length (δ_d) in SPR is typically on the order of half of the resonance wavelength (few hundreds of nm). This feature enables SPR biosensors to provide higher sensitivity to a bulk refractive index (RI) change, and is susceptible to background noise coming from bulk refractive index fluctuation. The sensitivity of SPR biosensors usually lies between 10^{-7} and 10^{-6} in refractive index unit (RIU) (107, 108) which represents the range of pM-nM detection limit for the target analyte detection. However, in clinical studies the small molecule such as cytokine molecule concentration falls around range of pM-fM (31). Thus, to overcome the sensitivity limitation, some of SPR sensing platforms involved using secondary antibodies or compounds to amplify the sensing signal.

Chou et al. demonstrated an SPR biosensor combined with a secondary antibody as a signal enhancer for detecting IL-6 in cell culture medium and achieved a detection limit around 1.3 ng/mL (109). Several studies further use nanoparticles to enhance the SPR signal. Martinez-Perdigueroa et al. and Law et al. developed a nanoparticle-based SPR biosensor by integrating gold nanoparticles and immunoassay technologies into SPR system to detect cytokines (Figure 2.4) (110, 111). In both studies, an evanescent field that was extended from the gold film to the gold nanoparticles induced plasmonic coupling, drastically enhancing the detection sensitivity. Approaches mentioned above introduce a secondary element to enhance the SPR signal and

provide better detection limit for the sensing. However, all these methods implemented additional assay steps, complicate overall procedures, and diminish the merits of label-free sensing by tagging labels to the target molecule.

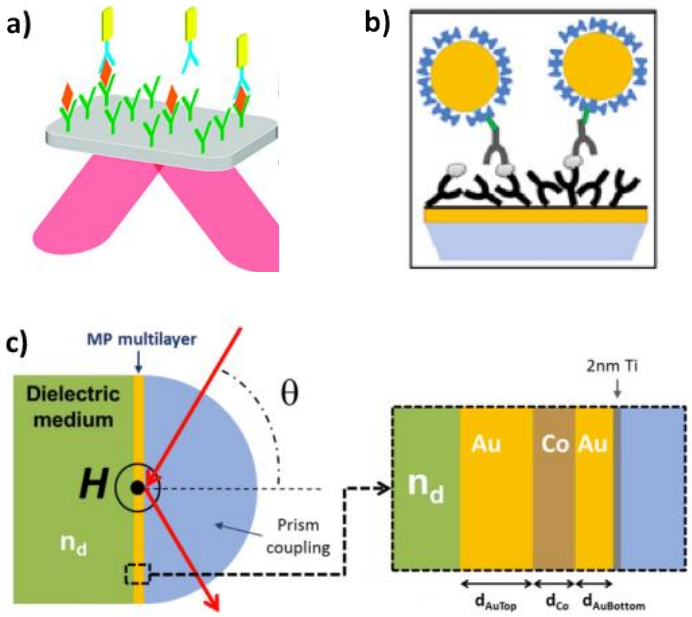

Figure 2.4 (A)-(B) SPR sensing introducing gold nanoparticles to enhance the SPR signal to increase sensitivity (110, 111). (C) Modified characteristics of metal thin film layer to improve SPR sensing capability (112).

Battaglia et al. explored alternative SPR excitation methods using fiber-optics to improve the sensing performance for SPR detection (93). In the study, IL-1, IL-6 and TNF-α in PBS solution was detected with fiber-optics and achieved sensitivity around 1 ng/mL, but failed to meet the sensitivity level of clinical requirements such as few pg/mL. Furthermore, improvements of the sensing capability of SPR biosensors were explored by improving the characteristics of the metal thin film layer (Figure 2.4C) or by altering the dielectric surrounding (112).

Recent advances in nanomaterials and nanofabrication processes open up the potential of LSPR plasmonic biosensing techniques for fast, real-time, label-free detection of biological species. The evanescence field surrounding LSPR sensors is directly excited by EM illumination

by free space optics. As a result, in LSPR, the bulky optics is not required and the system can be miniaturized and integrated with other systems. Furthermore, the EM field is highly confined to a local area near a metal nanostructure surface; biomolecules attached onto the nanostructure surface occupy a large fraction of the evanescence field volume. This leads to a significant change of the LSPR signal from the sensing substrate and result into high sensitivity that allows capability to detect small molecules.

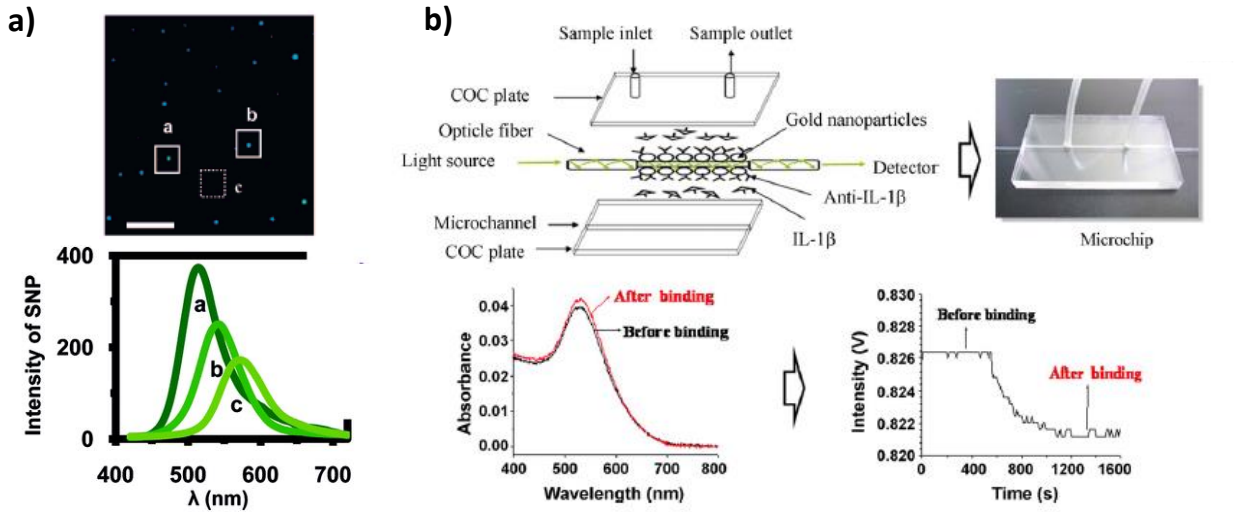

Figure 2.5 (A) A single silver nanoparticle-based nanoplasmonic biosensor for immunoassay detection (113). (B) Fiber-optics based rapid, sensitive LSPR biosensing platform (114).

Huang et al. demonstrated LSPR biosensors detecting TNF-α molecules using a silver nanoparticle (113). This biosensing technique offered an ultrasensitive platform which enables measuring single molecule level detection. But this sensing mechanism requires long analysis time for analyte binding to reach equilibrium, which hinders use of rapid immune diagnosis application. For more rapid sensing of cytokine molecules, Chiang et al. and Huang et al. measured IL-1β and TNF-α by providing few tens of pg/mL detection sensitivity within less than 10 min (114, 115). However, in these platforms the fiber probe should be dipped into a large volume of sample for signal measurement, which leads to practical limitations in its clinical applications. More recently,

Chen et al. developed a nanoparticle patterned microarray type of LSPR biosensing device detecting multiple cytokine species using few serum cytokine samples in a single device at the same time (31). In this study, instead of using a single nanoparticle, the patterned array of nanoparticles was used as sensing element and functionalized with six different probe antibodies for sensing. This platform allows high throughput analysis of cytokine biomarker in 1 μL serum sample to a detection limit around 10 pg/mL within 40 min.

Despite the recent advancements, the sensitivity of a majority of LSPR biosensors still falls short of matching that of ELISA and other non-label-free assay techniques. This warrants further exploration of new approaches to LSPR biosensing.

Chapter 3

Rapid Single-molecule Digital Detection of Protein Biomarkers for Near-real-time Monitoring of Systemic Immune Disorders

3.1 Introduction to the Study

The evolution of biomarker-guided precision-medicine therapies targeting specific pathological processes has advanced rapidly, based on a greater understanding of genomic, molecular, and cellular data of an individual patient (116, 117). However, implementing the precision medicine approach in critical care uniquely faces enormous challenges (118). In particular, timely diagnosis and treatment of a quickly evolving illness (119-121) require both fast and sensitive measurement of biomarkers as well as accessibility near the patient. Numerous efforts have been undertaken to develop rapid immunodiagnostics, including assay step simplification (30), label-free biosensing (31-35), surface-to-volume ratio enhancement (36-38), active analyte mixing (39, 40), and molecular pre-concentration (41, 42). Nonetheless, these methods generally sacrifice assay sensitivity and specificity, and face significantly increased complexity and cost resulting from sophisticated micro/nanofabrication. For a system with weak antigen-antibody affinity, where the protein binding kinetics are solely limited by the surface reaction rate (reaction-limited regime (43)), the aforementioned methods involving active mass transport enhancement or miniaturization become less effective for shortening the assay time.

Digital immunoassays are emerging techniques for biochemical analysis of analytes in low abundance. Their single-molecule sensitivity originates from binary counting of On/Off signals amplified within various types of small sub-volume partitions (52). The wide use of digital assays can be found in the literature as a platform for the ultrasensitive detection of nucleic acids (68, 70), proteins (52-54, 122-124), single viruses (125), and exosomes (126). The most well-established commercial implantation of an enzyme-linked immunosorbent assay (ELISA)-based digital assay, namely digital ELISA (dELISA), is Quanterix's Simoa (51). However, the high assay and instrumentation costs with the current bulky design in optics and fluid handling components prevent its application for near-bedside real-time diagnosis. Recently, Yelleswarapu et al. (122) developed a smartphone-connected microfluidic platform for miniaturized dELISA detection of cytokines using parallel droplet generation/detection methods. Despite the exciting performance and potential for point-of-care operation, this platform still requires a long sample incubation time > 90 min, thus leading to a total sample-to-answer time > 2 hours. In general, there is lack of a platform that can provide near-realtime protein biomarker profiling with a large clinically relevant dynamic range from fM to sub-nM. This is a critical bottleneck against fulfilling the promise of biomarker-guided precision medicine in time-sensitive critical care.

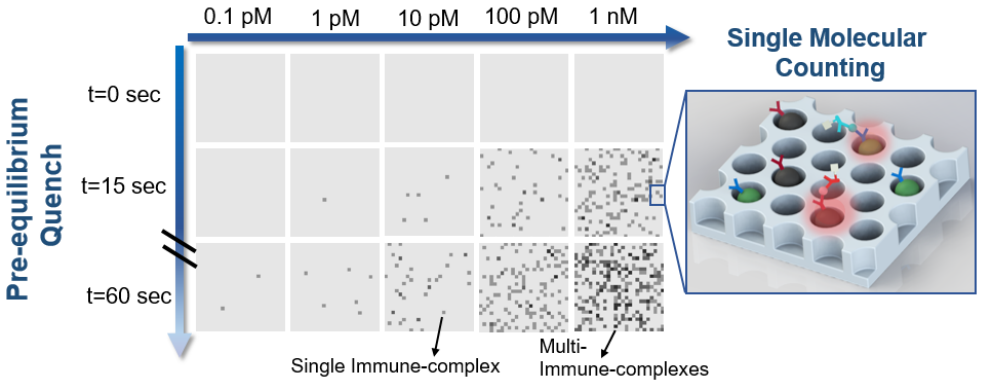

Figure 3.1 Schematic concept of instantaneous single-molecule binary counting of pre-equilibrium protein binding events. The combination of pre-equilibrium reaction quenching with single molecular counting can theoretically achieve an assay with a near-zero incubation time without losing linearity.

Herein, we introduce the concept of instantaneous single-molecule binary counting of non-equilibrium protein binding events to simultaneously realize speed and sensitivity – the two key combined features critically lacking in conventional technologies for acute illness. This concept provides the basis for the PEdELISA technique enabling a rapid, sensitive biomarker analysis with a significantly shorter (up to 10-fold) incubation time than the gold standard ELISA method. The technique captures the "snapshot" of a pre-equilibrated 2-step sandwich assay formation process quenched at its very early stage (within 15-300 sec) and applies single-molecule binary counting for biomarker quantification (Figure 3.1). In this study, we were surprised to find that this early quenching approach maintained a large assay linear dynamic range from fM to clinically relevant sub-nM, which is conventionally believed to be far outside the range permitted by single-molecule binary counting (56, 127). We developed a theoretical model to validate this concept and later demonstrated this concept with a digital assay that could uniquely performed in nearly real-time, longitudinal profiling of circulating protein biomarkers in septic mice for which the sample volume was highly limited, and in human patients treated with CAR-T therapy who were experiencing cytokine release syndrome (CRS). The captured temporal biomarker profiles manifested rapid feedback to the monoclonal antibody therapy, which may potentially guide individualized management of CRS under optimal intervention conditions.

3.2 Materials and Methods

3.2.1 Materials.

The mouse CitH3 capture antibody was generated by ProMab Biotechnologies, Inc. (Richmond, CA, USA). CitH3 detection antibody and HRP-conjugated secondary antibody were purchased from Abcam and Jackson ImmunoResearch. Human IL-6 capture and biotinylated detection antibodies were purchased from BioLegend. Human TNF-α, IL-2, and MCP-1 assay

were developed based on uncoated ELISA kits (including capture antibody, biotinylated detection antibody, and avidin-HRP) from Invitrogen. Dynabeads, 2.7μm-diameter carboxylic acid, and epoxy-linked superparamagnetic beads, QuantaRed™, an enhanced chemifluorescent HRP substrate, Alexa Fluor™ 488 Hydrazide, EDC (1-ethyl-3-(3-dimethylaminopropyl) carbodiimide hydrochloride), Sulfo-NHS (Sulfo-N-hydroxysulfosuccinimide), MES (2-(N-morpholino)ethanesulfonic acid) buffered saline, TBS StartingBlock T20 blocking buffer, and PBS SuperBlock blocking buffer were obtained from Thermo Fisher Scientific.

3.2.2 Finite Element Analysis of Transient Digital Assay.

The commercial FEA software COMSOL 5.4 Multiphysics was used to model the 2-step PEdELISA process involving molecular transport and bead surface reaction. Several model assumptions were made based on experimental conditions. First, we assumed that the magnetic beads were evenly distributed in the buffer solution by the orbital shaker mixing during the incubation process. As a result, the model only considered the half of a single bead surface within the "reaction volume," which is scaled by the sample volume divided by the number of the beads used. The cytokine diffusion profile was evaluated using the transient mass convection and diffusion equation as:

$$\frac{\partial c}{\partial t} = D \cdot \nabla^2 c - \vec{u} \cdot \nabla c + R \tag{1}$$

where c is the concentration, the convection term $\vec{u} \cdot \nabla c$ was omitted, and we adjusted the value of the diffusion coefficient D to reflect the mass transport under active mixing. The first step of the PEdELISA process was modeled by considering the simultaneous reactions between the capture antibody (Ab_1), antigen ligand (L), and the detection antibody (Ab_2). The derived kinetics equations using Langmuir isotherm are given as:

$$\frac{d[Ab_1L]}{dt} = k_{on1}([Ab_1]_0 - [Ab_1L])[L] - k_{off1}[Ab_1L] \quad (2)$$

$$\frac{d[Ab_2L]}{dt} = k_{on2}([Ab_2]_0 - [Ab_2L])[L] - k_{off2}[Ab_2L] \quad (3)$$

$$\frac{d[Ab_1LAb_2]}{dt} = k_{on1}([Ab_1]_0 - [Ab_1L])[Ab_2L] + k_{on2}([Ab_2]_0 - [Ab_2L])[Ab_1L] - (k_{off1} + k_{off2})[Ab_1LAb_2] \quad (4)$$

where k_{on} and k_{off} are the association/dissociation constants, and [ ] represents the concentration or surface density of the three agents. For simplicity, we assumed that the affinity of Ab_1 to L is the same as the affinity of Ab_2 to L ($k_{on1}=k_{on2}$, $k_{off1}=k_{off2}$). For the second step labeling process, the avidin-HRP conjugate and the immune-complex Ab_1LAb_2, were modeled as the "free ligand" and the surface immobilized capture agent, respectively. The kinetic equation for this process is given as:

$$\frac{d[Ab_1LAb_2HRP]}{dt} = k_{on3}([Ab_1LAb_2]_0 - [Ab_1LAb_2HRP])[avidinHRP] - k_{off3}[Ab_1LAb_2HRP] \quad (5)$$

Finally, to translate the molecular binding events into the digital assay readout, we used the Poisson distribution equation given as:

$$\lambda = -\ln(1 - P_{positive}) \quad (6)$$

where $P_{positive}$ is the fraction of fluorescence-activated "On" beads to the entire beads and λ is the mean expectation value, which represents the average number of immune-complexes per bead.

3.2.3 Definition of the Pre-equilibrium State.

Using the Langmuir adsorption model:

$$\frac{d[AbL]}{dt} = k_{on}[L]([Ab]_0 - [AbL]) - k_{off}[AbL] \quad (7)$$

where $[L]$ is volume ligand concentration, $[Ab]_0$ is initial surface antibody concentration, $[AbL]$ is the surface concentration of ligand-antibody complex, and k_{on} and k_{off} are respectively the on-rate and off-rate constants.

For simplicity, we assume the surface ligand concentration (cytokine concentration) $[L] = c_0 = Constant$ (not changing with time, perfect mass transfer). Then the above differential equation can be solved as:

$$BR = \frac{[AbL]}{[Ab]_0} = \frac{c_0}{c_0 + K_d}[1 - e^{-(k_{on}c_0 + k_{off})t}] \tag{8}$$

where BR is the surface binding ratio. By letting $t \to \infty$, we can obtain the asymptote:

$$BR_\infty = \frac{c_0}{c_0 + K_d} \tag{9}$$

In an increasing system, the time constant τ is the time for the system to reach $(1 - e^{-1}) \approx 63.2\%$ of its final asymptotic value (128). Therefore we can calculate:

$$\tau = \frac{1}{k_{on}c_0 + k_{off}} = \frac{k_{off}^{-1}}{1 + c_0/K_d} \tag{10}$$

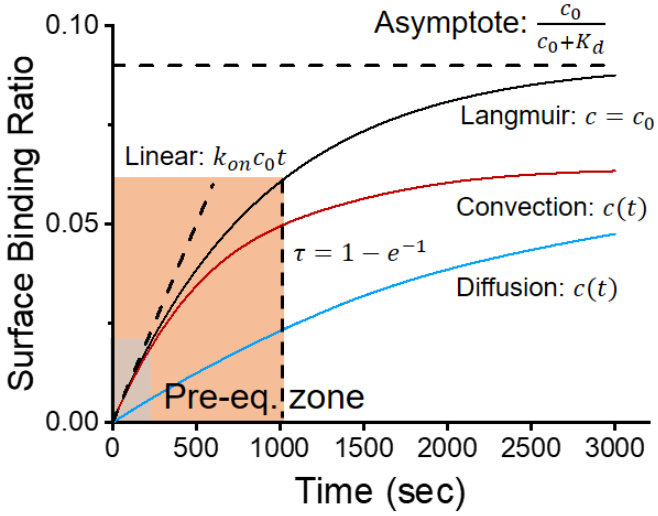

Figure 3.2 Theoretical binding kinetics of bead surface adsorption process. The pre-equilibrium state is determined by the time constant τ based on the Langmuir model.

The PEdELISA is operating at pre-equilibrium state: t<τ. To estimate the τ value, typical dissociation constant K_d for antibody to antigen is 1nM, with $k_{on} \approx 10^6$ $M^{-1}s^{-1}$ and $k_{off} <= 10^{-3}$ s^{-1}, and

clinical relevant cytokine detection concentration c_0 is generally from 10fM to 0.1nM. The time constant τ is estimated to be around 1000sec (16.7min).

In reality, the solution ligand concentration [*L*] is not a constant, but decreasing over time *c(t)* as the bio-reaction goes on and it also takes the time for the target molecules to diffuse to the sensor surface. Therefore, the real binding curve will look like the blue diffusion line as shown in Figure 3.2 (solved by a numerical solver COMSOL) or somewhere in the middle of the convection and diffusion line. Nonetheless, a simple time constant defined based on the ideal Langmuir binding curves is good enough to define a pre-equilibrium zone. After considering the diffusion and k_{off} less than 10^{-3} s^{-1} cases, this time constant will be longer than the estimated 16.7min. The incubation time of PEdELISA is in between 15-sec to 600-sec and it is operated at the early pre-equilibrium state.

3.2.4 Device Fabrication and Assembly.

The microwell structure and the microfluidic channel were fabricated in poly-dimethylsiloxane (PDMS, Dow Corning Sylgard 184) using the standard soft lithography technique. Firstly, two silicon molds, one for the microwell structure with a thickness of 4 μm (SU-8 2005, Micro-Chem), the other for the microfluidic channel with a thickness around 100 mm (SU-8 2050, Micro-Chem), were fabricated by photolithography. Secondly, a precursor of PDMS prepared at a 10:1 base-to-curing agent mass ratio was spin-coated onto the microwell silicon mold (300rpm, 1min) and poured over the microfluidic channel mold with a thickness around 4mm. Both of the molds were left on the flat surface overnight and then cured in an oven at 60 °C for 2h. The surface of the thin-film PDMS microwell layer cured on the silicon mold wafer was treated by oxygen plasma. The film was aligned using a custom-machined aluminum jig and bonded onto a pre-cleaned 75×50mm glass slide, and finally removed from the silicon wafer. The PDMS microfluidic channel layer was

cut and peeled off of its silicon mold and punched manually to form its inlet and outlet. After second oxygen plasma treatment, the top surface of the thin-film PDMS microwell layer was aligned with and bonded to the PDMS microfluidic channel layer. Finally, the entire chip was briefly baked at 60 °C and stored at room temperature before use.

3.2.5 Antibody Conjugation to Magnetic Beads.

The non-color encoded magnetic beads were prepared by conjugating epoxy-linked Dynabeads with the capture antibody molecules at a mass ratio of 6 μg (antibody): 1 mg (bead). To prepare the fluorescence encoded magnetic beads for multiplex detection, carboxylic acid-linked Dynabeads were first labeled with AF 488 dye, and then conjugated with the capture antibody molecules as follows: 100 μL of a bead stock solution (30 mg beads/mL) was washed with 25mM MES buffer at pH=5 for two times, mixed with 100 μL of a 1mg/mL EDC solution and 100 μL of a 1.13mg/mL sulfo-NHS solution (25mM MES buffer), and then incubated at room temperature on an orbital shaker at 1000 rpm for 30min. Then, the beads were washed two times with the MES buffer and mixed with a 1 μg/mL AF488 hydrazide solution for 30min. Then, the beads were washed 5 times with 0.5 mL PBS-T (0.1% Tween20) solution, resuspended in 300 μL of a PBS-T (0.05% Tween20) solution, and transferred into a new polypropylene tube. The AF488-encoded beads were washed two times with the MES buffer, reactivated with 100 μL of a 50 mg/mL EDC solution and 100 μL of a 50 mg/mL sulfo-NHS solution for 30 min, and then rinsed two times with the MES buffer. A 100 μL capture antibody solution was prepared and mixed with the activated beads at a mass ratio of 12 μg (antibody): 1 mg (bead) for 2h at room temperature. Then the beads were separated and washed 4 times with 0.5 mL PBS-T (0.1% Tween20) solution and stored at 10 mg beads/mL in PBS-T (0.05% T20 + 0.01% Sodium Azide) solution wrapped with aluminum foil at 4 °C. No significant degradation was observed within the 3-month usage.

3.2.6 Mouse CLP Preparation and Sample Collection.

Sepsis was induced by cecum ligation puncture (CLP) in male mice with age between 8-12-week-old. The peritoneal cavity was opened under inhaled isoflurane anesthesia. Cecum was eviscerated, ligated below the ileocecal valve using a 5-0 silk suture at three different points (50%, 75%, and 100%), and punctured through (two holes) with a 21-ga needle. The punctured cecum was squeezed to expel a small amount of fecal material and returned to the peritoneal cavity. The abdominal incision was closed in two layers with 4-0 silk suture. The Sham mouse was handled in the same manner, except that the cecum was not ligated and punctured. Around 15 μL blood was drawn through the tail vein every 4-5 hours after CLP. The blood was allowed to clot by leaving it undisturbed at room temperature for 30 minutes. The clot was then removed by centrifuging at 2000 × g for 15 minutes in a refrigerated centrifuge. The supernatant serum was used for the following PEdELISA assay. This protocol was approved by the University of Michigan (PRO00008861). All surgery was performed under anesthesia, and all efforts were made to minimize suffering.

3.2.7 Patient Blood Sample Collection and Preparation.

Subjects undergoing CAR-T therapy were recruited and samples collected with informed consent for each subject under the University of Michigan IRB protocol HUM00115179/UMCC 2016.051. Control samples were obtained from healthy volunteers with informed consent under University of Michigan IRB protocol HUM00092161. All blood samples were collected on-site at the University of Michigan Medical School Hospital. Venous blood was collected for serum into a vacutainer containing no anticoagulant. Blood samples were then transported to the lab, allowed to clot for at least 30 minutes, and processed for serum isolation. Samples were centrifuged at 1,200 × g for 15 minutes at room temperature. Serum was then removed by pipette and aliquoted

into 2 mL screw cap tubes. Serum aliquots were then transported fresh on wet ice for the PEdELISA assay or banked at -80 ºC.

3.2.8 PEdELISA Assay.

The capture antibody beads were first incubated with the TBS StartingBlock buffer (0.05% Tween20) for 30 min to block the beads surface and quench all the unreacted groups. Then the beads were washed once with a PBS-T buffer and divided into 96-well reaction tubes so that each tube has approximately 8×10^5 beads. The samples were diluted by the ELISA dilution buffer (1% BSA, 0.05% Tween20). The dilution ratio for CitH3 is 1:4. The dilution ratio for IL-2 and TNF-α is 1:2 due to their low abundance in serum and the dilution ratio for IL-6 and MCP-1 is 1:4 or 1:8 based on the potentially high level under severe CRS condition. The recombinant standards were diluted by an ELISA dilution buffer spiked with 25% fetal bovine serum. The diluted samples were temporarily kept on wet ice until use. In the two-step assay protocol, a mixture of 10 μL of the sample or standard and 10 μL of a biotinylated detection antibody (0.25 μg/mL) solution was loaded to the tube and incubated with the magnetic beads for a period of 60 sec to 300 sec. After a quick buffer exchange (1× PBS-T, 0.1% Tween20), the beads were then incubated with 40 μL of the avidin-HRP solution for 30 sec. After washing in a 2× PBS-T (0.1% Tween20) buffer solution 6 times, they were resuspended in 11 μL of a 1× PBS-T (0.1% Tween20) buffer solution. 10 μL of the bead solution was loaded into the premade microfluidic chip, which contains 16 separate channels for different samples. Each channel was then loaded with 20 μL of the enhanced chemifluorescent HRP substrate QuantaRed solution and subsequently sealed with 20 μL of fluorinated oil (HFE-7500, 3M). The inlets and outlets of the channels were covered by glass coverslips to prevent evaporation during the imaging process. A programmable motorized fluorescence optical microscopy system was used to scan the image of the bead-filed microwell

arrays on the microfluidic chip, identify the bead type (non-color vs. AF488 dyed), and detect the enzyme-substrate reaction activity. This system is composed of Nikon Ti-S fluorescence microscope, a programmable motorized stage (ProScan III), a halogen lamp fluorescence illumination source, a SONY full-frame CMOS camera (α7iii), and a custom machined stage holder. The motorized stage was pre-programmed to follow the designated path to scan the entire chip. The image process took about 20 sec to scan each channel (1 sample/channel, total 16 channels), following 3 sequential steps: 1. Scan the QuantaRed channel (532nm/585nm, excitation/emission) 2. Scan the AF488 channel (495nm/519nm, excitation/emission) 3. Scan the brightfield.

3.2.9 Data Analysis and Image Processing.

In the digital immunoassay, statistical analysis of the fraction of the fluorescence-activated "On" beads to the entire beads across 336,000 femtoliter-sized microwells per channel determined the analyte concentration value. A custom image processing MATLAB code was used to analyze scanned microwell-array images automatically with high speed and accuracy (Figure 3.3). Briefly, the code simultaneously captures the images from all of the AF488 (bead encoding dye), QuantaRed (labeling dye), and Brightfield channels and superimposes them. Then, it counts the numbers of the "On" and "Off" states for the two types of beads (AF488-encoded and non-color types) trapped in the microwells from the superimposed images. The code includes algorithms to avoid counting aggregated beads and to eliminate signals from false positives, imaging defects, and large fluorescence contaminations. The fraction of the "On" states were correlated with the analyte concentration from the standard curve.

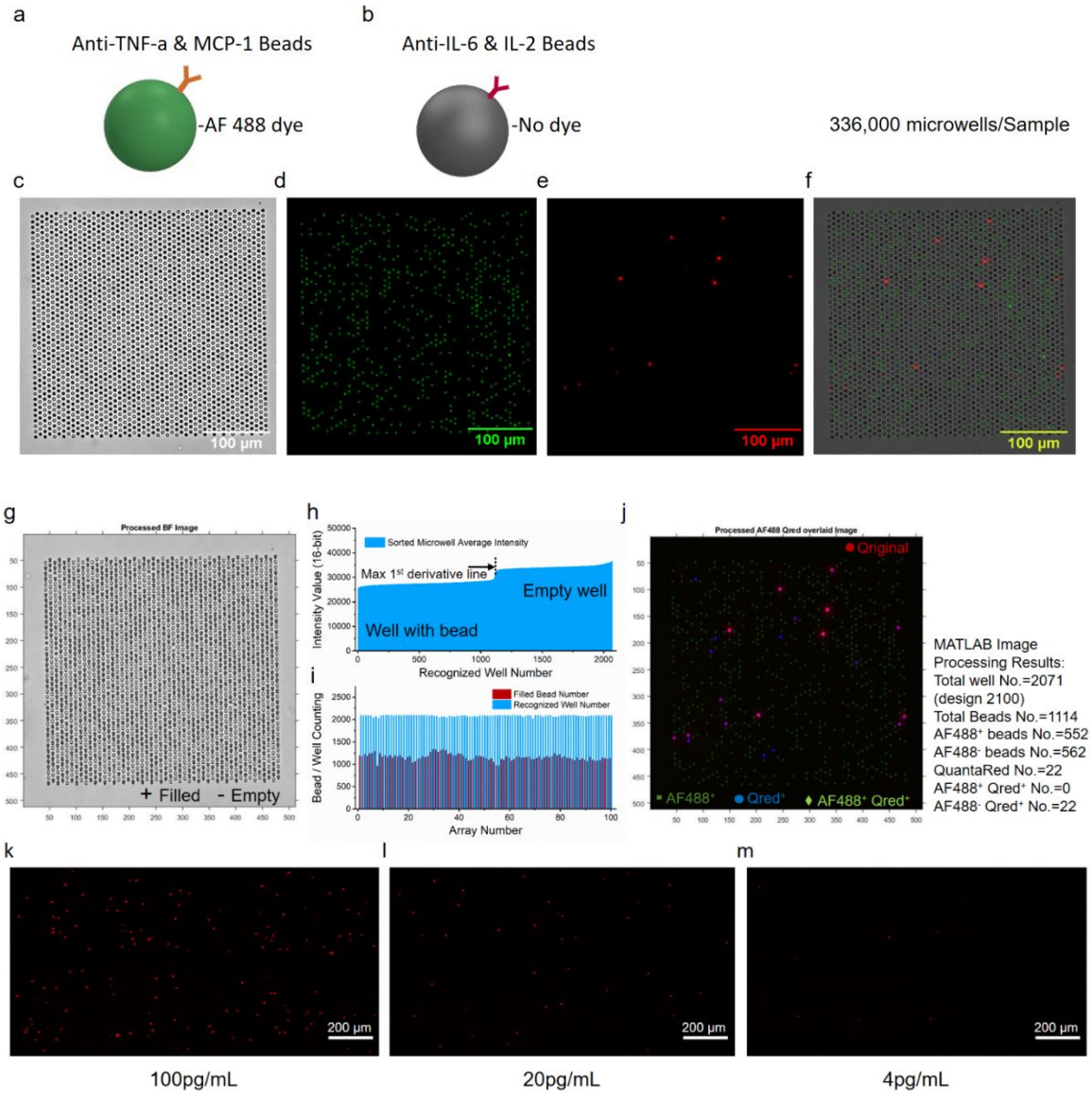

Figure 3.3 Dual-plex PEdELISA assay encoded using (a) 2.8 μm-diameter superparamagnetic beads first dyed with Alexa Fluor (AF) 488 and then conjugated with capture antibodies against TNF-α or MCP-1 and (b) 2.8 μm-diameter non-color superparamagnetic beads conjugated with capture antibodies against IL-6 or Il-2. Image of arrayed microwells in (c) bright field, (d) AF 488 channel, (e) QuantaRed (Qred) channel, and (f) three-channel (bright field + AF 488 + Qred) overlay modes . (g) MATLAB code-processed bright field image to determine the overall bead filling rate with filled (+) and empty (–) wells. (h) Sorted microwell intensity histogram. (i) Bead and microwell counting across 100 arrays of microwells. (j) MATLAB code-processed two-channel (AF 488 + Qred) overlay image for dual-color digital counting (dark green square: AF488-dyed bead, blue circle: non-color bead with Qred emission, light green diamond: AF488-dyed bead with Qred emission). Snapshot of Qred image showing enzyme active Qred "On" microwell spots with the presence of bead-bound analyte molecules (e.g., TNF-α and IL-2) at (k) 100 pg/mL, (i) 20 pg/mL, and (m) 4 pg/mL.

The detailed 4-step algorithm is summarized below:

Step 1: The code simultaneously reads all of the bright field (Figure 3.3c), Alexa Fluor (AF) 488 (Figure 3.3d), and QuantaRed (Qred) (Figure 3.3e) images and first identifies the locations of AF488-dyed beads based on fluorescence intensity thresholding (the method of image segmentation by creating binary images). Sub-algorithms identifying the area and signal intensity of beads are used to remove counts of defects like clusters of aggregated beads. If a defect is identified by a pre-defined value of aggregation severity, it is removed from the counts for the Qred and bright field images (similar in step 2 and 3).

Step 2: The Qred image is analyzed based on fluorescence intensity thresholding, size-based circle detection, and morphological dilation and erosion to identify the locations of all the enzyme active "On" (or Qred "On") microwells. Sub-algorithms identifying the total number, areas, signal intensities, inter-distances, and image boundaries of arrayed microwells are used to eliminate all false positives, image defects, and large fluorescence contaminations. Signal crosstalk is an issue uniquely found in the Qred image analysis. It is a type of false-positive counting that often happens when a microwell is so bright that a few of its nearest neighboring microwells in the hexagonal array arrangement are also brightened up to exceed the threshold intensity. In this case, these neighboring microwells are falsely counted as "On" signals even though they are not actually enzyme active. To mitigate this issue, we applied a distance pattern recognition algorithm, which first identified all the bright spots with their 6 nearest neighbors and then performed a second-round intensity check (high threshold) to determine if their neighboring microwells are true or false positives.

Step 3: The bright field image is analyzed to identify the areas of microwells using edge and pattern recognition algorithms based on the Sobel edge detection methods. Then, the microwell brightness

intensity is averaged over the identified area and its values are sorted for the entire arrayed microwells in the bright field image (Figure 3.3h). This microwell intensity sorting effectively helps divide the microwells into two distinct groups: those that contain (+) or do not contain (-) beads. The separation line was determined by the maximum intensity slope (first derivative) of the sorted intensity values. Sub-algorithms are subsequently used to eliminate local image areas with poor bead-to-well contrast, air bubbles, and large dust. Step 3 has intrinsic uncertainties due to image quality variances in focus adjustment during the image scanning process. To suppress error due to these uncertainties, the counting process is repeated and averaged over the repeats. For example, in Figure 3.3g, the original design of each array of microwells contains 2,100 microwell locations but our MATLAB program indicates that the number of recognized microwells is 2,071. Among them, 1,114 wells are identified to have beads inside. The numbers of counted beads and microwells are obtained and averaged across 100 arrays of microwells to determine the overall bead filling rate for our counting (Figure 3.3i).

Step 4: Finally, the code overlays the local images of the recognized AF488 positive beads on top of the Qred image to determine the numbers of Qred "On" microwells with and without an AF488-dyed bead inside (Figure 3.3j). Considering a potential misalignment in the image overlay process, each Qred "On" microwell is marked with a blue circle 1.4 times larger than its original size. Finally, dual-plex cytokine detection is achieved by determining the fractional population of the enzyme active Qred "On" microwells to the bead-filled (+) microwells for both the AF488 dyed and non-color bead types. Figure 3.3k-m show Qred image snapshots for a mixture sample of TNF-α and IL-2 both at a concentration ranging from 4 pg/mL to 100 pg/mL.

3.2.10 Statistics.

Experiments with synthetic recombinant proteins were performed 3 times (in independent tests) to obtain the error bar. Due to the extreme low sample volume (<7μL) obtained from the CLP mouse at each time point, the CitH3 PEdELISA assay was performed with no repeat. Either duplicate or triplicate PEdELISA measurement was performed for the CAR-T patient sample at a single time point of the near-real-time cytokine profile monitoring test. Conventional ELISA tests were conducted with no repeat for a few selected time points of the banked serum samples. Here, Pearson's R-value was used to quantify the PEdELISA to ELISA correlations. Group differences were tested using one-way ANOVA and comparing means with the Tukey test. A p-value of < 0.05 was considered to be statistically significant.

3.3 Results

3.3.1 Design of PEdELISA platform.

We designed the PEdELISA process to employ a 2-step semi-homogeneous format so that it only involves (1) mixing the capture antibody-coated magnetic beads with the analyte and detection antibody solution to form the capture antibody-antigen-detection antibody complex (Step 1) and (2) labeling with enzyme HRP (Step 2) (Figure 3.4A). To ensure accurate single-molecule counting at a wide range (10 fM-1 nM), which is relevant to clinical diagnosis, the process was designed to keep the population of fully labeled immune-complex molecules less than one per bead despite the original abundance of analyte molecules in each sample partition. In PEdELISA, this single-molecule counting condition is achieved by intentionally stopping the immunologic reaction in its pre-equilibrium state (see Figure 3.2 for the definition of the pre-equilibrium state).

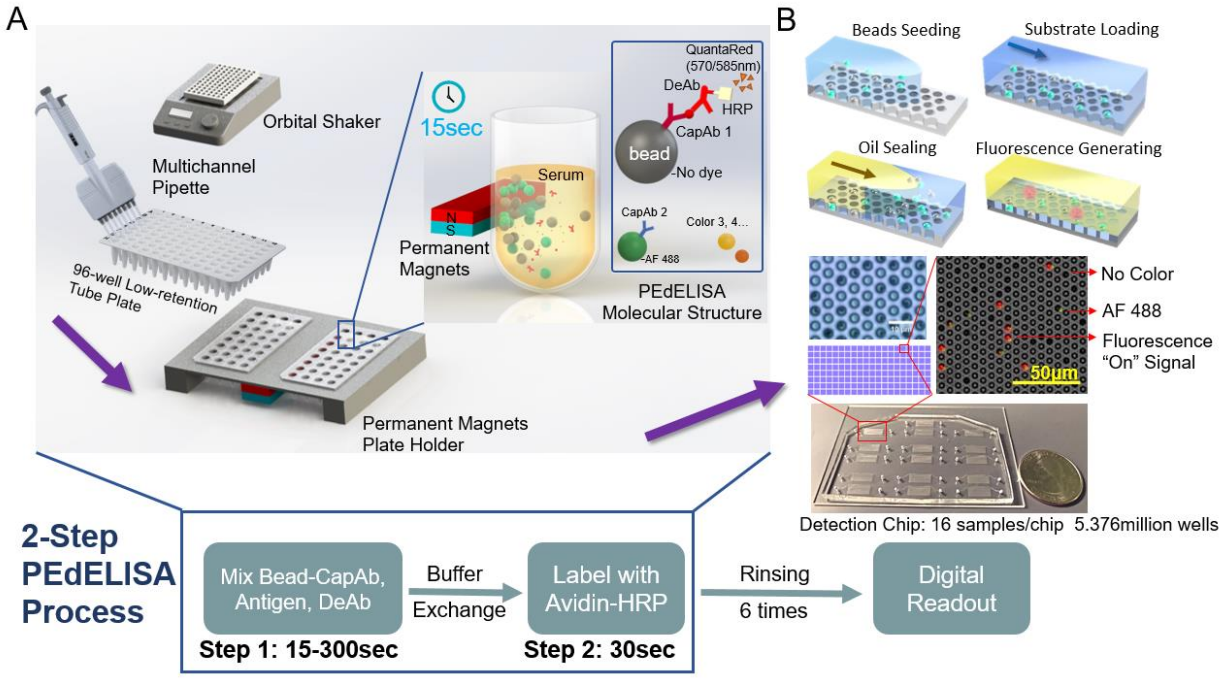

Figure 3.4 (A) Two-step ultrafast, dual-plex PEdELISA process for pre-equilibrated assay system, including short (15–300sec) two-color magnetic bead incubation for the formation of antibody-antigen-antibody immune-complexes (Step 1), buffer exchange, quick (30sec) avidin-HRP labeling (Step 2), and 6-repeated rinsing within 96-well low-retention tubes. (B) Digitization process that involves trapping of magnetic beads into on-chip microwell arrays, loading of HRP fluorescence substrate (QuantaRed), and sealing of beads with fluorocarbon oil. Digital signal readout by automated image scanning and counting of fluorescently activated "On"-state microwells. The two-layer (microwell layer, micro-chamber layer) PDMS-based microfluidic detection chip which contains a total of 5.376 million d=3.8 μm microwells can handle 16 samples per scanning. CapAb: capture antibody. DeAb: detection antibody.

For practical operation in PEdELISA, we designed a fluid manipulation system with a 96-well low-retention tube plate, a multichannel pipette, a plate holder with permanent neodymium magnets, and an orbital shaker (Figure 3.4A). The system enabled us to achieve precise time control, reduce the total sample volume to 10 μL, efficiently pull the magnetic beads to the sidewall of the plate holder for buffer exchange, and actively mix reagents in each reactor tube. We used fluorescence-color encoded beads that were conjugated with different capture antibodies to achieve multiplex measurement at high throughput (see Figure 3.3).

The reaction process was followed by a digital signal detection process (Figure 3.4B), in which a custom-designed microfluidic detection chip was used to isolate individual beads into sub-arrays of 336,000 fL-sized partition wells. HRP reaction with a fluorescent substrate was used to indicate which beads were bound to antigen complexes. Confining the HRP catalyzed fluorophores to the tiny fL-sized volumes significantly amplified the readout signal up to single-molecule sensitivity for the immune-complex formation detection. The wells with activated fluorescence were imaged by an inexpensive full-frame CMOS camera and analyzed by a customized MATLAB code (Figure 3.3). We estimated that the average cost for reagents and device fabrication was $0.69 per test (Table 3.1). The 2-step assay format incorporated the conventional enzyme labeling strategy using biotin-avidin linkages, which makes PEdELISA compatible with any commercially available ELISA reagents. We anticipate that the PEdELISA assay expenses are significantly reduced by scale-up production of the system. This would manifest competitive cost advantages of PEdELISA over the current commercial ELISA ($2-5/test) or Luminex technologies ($30/test) in any clinical lab that is equipped with standard epifluorescence microscope.

Table 3.1 Cost estimation of the PEdELISA assay

Disposables & Reagents	Price ($)	Total amount	Amount /test	No. of tests	Cost/ test ($)
Dynabeads® Antibody Coupling Kit (ThermoFisher 14311D)	534	60 mg	6 μg (~4×10^5 beads)	10^4	0.05
Dynabeads® M-270 Carboxylic Acid (ThermoFisher 14305D)	415	60 mg	6 μg (~4×10^5 beads)	10^4	0.05
Purified anti-human IL-6 Antibody (BioLegend 501110)	250	500 μg	36 ng	1.39×10^4	0.018
IL-6 (Or MCP-1, IL-2, TNF-α) Human Uncoated ELISA Kit (ThermoFisher 88-7066-88)	459	10×96 ELISA test	-	Min. 1.25×10^4	0.037
Detection Antibody	Kit included	500 μL (250×)	0.04 μL	1.25×10^4	-
Avidin HRP	Kit included	1.25 mL (100×)	0.03 μL	3.75×10^4	-
Recombinant protein standard	Kit included	10 vials	-	-	-
Blocking buffer (1% BSA)	Kit included	150 mL (5×)	-	-	-
96-Well Nonskirted PCR Plates (FisherScientific 14-230-232)	39.55	25×96 test	3	800	0.05
Plain Glass Microslides (FisherScientific 12-550C)	63.26	1 gross (144 slides)	16 test /slide	2304	0.027
Dow Corning Sylgard 184 Silicone Encapsulant Clear 0.5 kg Kit	50.36	500 g	1g	500	0.1
StartingBlock™ (TBS) Blocking Buffer (ThermoFisher 37579)	188	1L	100 μL	10^4	0.019
QuantaRed™ Enhanced Chemifluorescent HRP Substrate Kit (ThermoFisher 15159)	350	110 mL	10 μL	10^4	0.035
Others (pipette tips, microcentrifuge tubes, HFE Oil, washing buffers, Tween 20, cover slips, etc)	-	-	-	-	0.3
				Total	0.69

3.3.2 Theoretical study of "quench-and-snapshot" measurement.

To theoretically predict outcomes of PEdELSIA, we first carried out a finite element analysis (FEA) on biomolecular interactions in digital immunoassay and then performed a parametric analysis to optimize the assay conditions. Our analysis accounted for mass transport and surface reaction for a theoretical "reaction volume" with a bead placed in its center (Figure 3.5A). Assuming that the beads were evenly distributed in the buffer/sample solution, the quantity of the reaction volume was taken to be the total buffer/sample volume divided by the number of the beads used for the assay. We first modeled the simultaneous molecular interactions between the analyte molecules, the capture antibodies immobilized on the bead surface, and the detection antibodies freely floating in the reaction volume using the mass transport and Langmuir adsorption equations (Figure 3.5B and Method). For simplicity, we assumed the same affinity for the capture and detection antibody molecules. Then, the enzymatic labeling process was modeled for a biotin-avidin linkage with an affinity (129) of $k_{on}= 5.5\times10^{8}$ $M^{-1}s^{-1}$ and $k_{off}= 3.1x10^{-5}$ s^{-1} (Figure 3.5C).

Using the key model parameters listed in Table 3.2, we predicted the kinetics of the antibody-antigen-antibody immune-complex formation process in Step 1 of PEdELISA for the affinity value ($K_d= 10^{-10}$-10^{-9} M) of typical commercially available antibodies. We plotted the average number of immune-complexes formed on a single bead surface, λ, as a function of the incubation time for the immune-complex formation process (Step 1 incubation time) and the analyte concentration (Figure 3.5D, E). Here, our model shows that the kinetics of the immune-complex formation on the bead surface is non-linear with time due to the simultaneous interactions of the target analyte to both the capture and detection antibody molecules. Nonetheless, the model predicts a linear increase in the quantity of the formed immune-complexes with the analyte concentration independent of time, the analyte mass transfer type (forced advection or passive diffusion), and

the number of beads. This linear relationship allows the digital readout of PEdELISA to increase linearly with the analyte concentration even for a very short assay incubation time. This finding provides the theoretical foundation for securing both high sensitivity and a large linear dynamic range in our pre-equilibrium quenching approach.

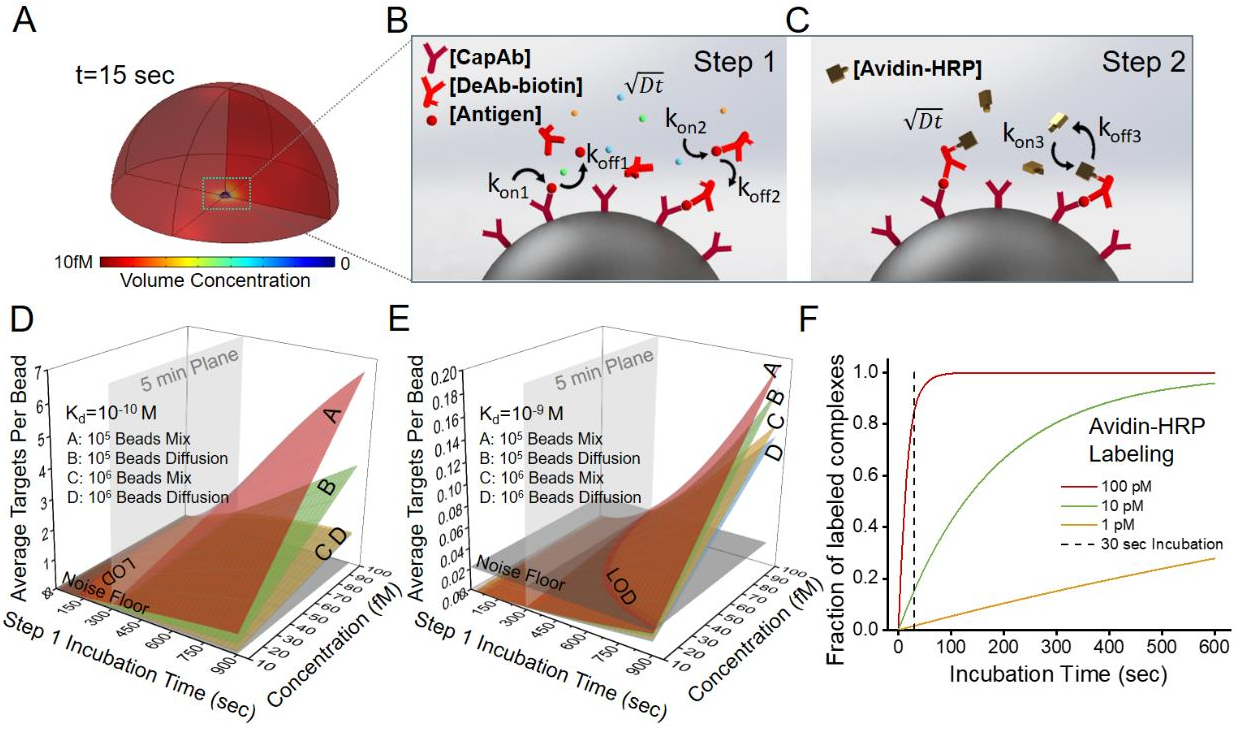

Figure 3.5 Finite element analysis of biomolecular interactions in the 2-step PEdELISA process. (A) Schematic of the theoretical sphere, namely the "reaction volume," used for modeling work, whose quantity is equal to the total sample volume divided by the number of beads. Reagent mass transport and binding kinetics are considered at the surface of a single magnetic bead placed in its center for half of the geometry due to symmetry. (B) Step1: immune-complex formation process involving the conjugation between target antigen molecules, capture antibodies immobilized on the bead surface, and detection antibodies freely floating in the reaction volume. (C) Step 2: avidin-HRP labeling process involving the conjugation of avidin-HRP with the biotinylated detection antibodies. The average number of targets (i.e., capture antibody-antigen-detection antibody immune-complexes) formed per bead, λ, is calculated as a function of the Step 1 incubation time and the analyte concentration at (D) $K_d = 10^{-10}$ M and (E) $K_d = 10^{-9}$ M. The model predicts that the PEdELISA readout linearly increases with the analyte concentration when λ is small (< 0.1). By accounting for the experimentally obtained noise floor, the LOD value can be theoretically determined for a given value of the Step 1 incubation time. (F) Predicted kinetics of the second step of the PEdELISA process. The fraction of the formation of HRP enzyme-labeled antibody-antigen-antibody immune-complexes is presented for three representative HRP concentrations of 1 pM, 10 pM, and 100 pM.

To optimize the assay conditions, we also evaluated the influence of several other crucial factors, such as the total number of beads per assay, the detection antibody concentrations, and the effect of sample-reagent mixing to enhance reagent mass transport. For a system with a large antibody affinity value (K_d=10^{-10} M, Figure 3.5D), the total number of beads and the mass transport both play crucial roles in determining the assay kinetics. In contrast, the Step 1 incubation time is the only dominant factor in determining the assay speed for a system with a weak affinity value (K_d=10^{-9}M, Figure 3.5E). The PEdELISA assay uniquely provides the means to shorten the assay time for a reaction-rate limited weak-affinity system, in which other existing ultrafast immunoassay methods primarily driven by mass transport enhancement through active mixing or surface-to-volume ratio enhancement fail to achieve this. Figure 3.5F shows the kinetics of the labeling process for three representative avidin-HRP concentrations and suggests that the concentration of 100 pM is sufficiently large to complete the process with the incubation time (Step 2 incubation time) of 30-sec.

Table 3.2 Key parameters for theoretical study

Antigen Concentration	**Detection Antibody Concentration**	**$k_{on1\&2}$**	**$k_{off1\&2}$**	**Diffusivity**
10 fM~10 pM	0.25-1 μg/mL	10^4~10^7 $M^{-1}s^{-1}$	10^{-3}~10^{-5} s^{-1}	10 $\mu m^2/s$
Time Step1	**Bead number**	**Sample volume**	**Antibody / bead**	**Bead radius**
0~900 s	10^5-~10^6	10 μL	(1.8~3.6)×10^5	1.4 μm
Time Step2	**Avidin-HRP Concentration**	**k_{on3}**	**k_{off3}**	
0~600 s	1-100 pM	5.5×10^8 $M^{-1}s^{-1}$	3.1×10^{-5} s^{-1}	

In addition, we further evaluated the influence of several other key assay parameters on the binding kinetics in Step1 reaction (Figure 3.6) to obtain optimal assay performance. Here, these

parameters include the detection antibody (DeAb) concentration, the number of magnetic beads used per sample, and the capture antibody binding site density (B_d). The parametric analysis was performed for different mass transport conditions with and without active mixing (diffusion only) with different on-rate association constant (k_{on}) values ranging from 10^4 to 10^7 $M^{-1}s^{-1}$, which represent different affinities of the antibody-antigen pair. We limited the detection antibody concentration to be < 1μg/mL in the calculation. This condition allows the assay to avoid experiencing high background non-specific adsorption in practice. We kept the magnetic bead amount above 10^5 per reactor (i.e., PCR tube) to ensure statistically significant digital counting. The number of the capture antibody conjugated per magnetic bead was estimated based on the experimental data provided by Dynabeads® Antibody Coupling Kit Manual (Thermo Fisher Scientific, Catalog number: 14311D).

For a case where the antibodies have a very weak affinity ($k_{on}=10^4$, Figure 3.6A), the immune complex formation kinetics is limited by the rate of surface reaction between the antigen and capture antibody molecules. The calculation indicates that neither mixing-driven mass transport enhancement nor the number of beads (equivalent to sample volume) will improve the assay performance in this "reaction-limited" regime. Although increasing the binding-site density (B_d) or detection antibody concentration helps increase the assay signal, it is impractical or costly to largely increase these two parameters. The average number of capture antibody conjugated per bead is almost invariant on the bead surface area. Meanwhile, blindly increasing the detection antibody concentration will generate a high level of background false positives due to non-specific surface adsorption.

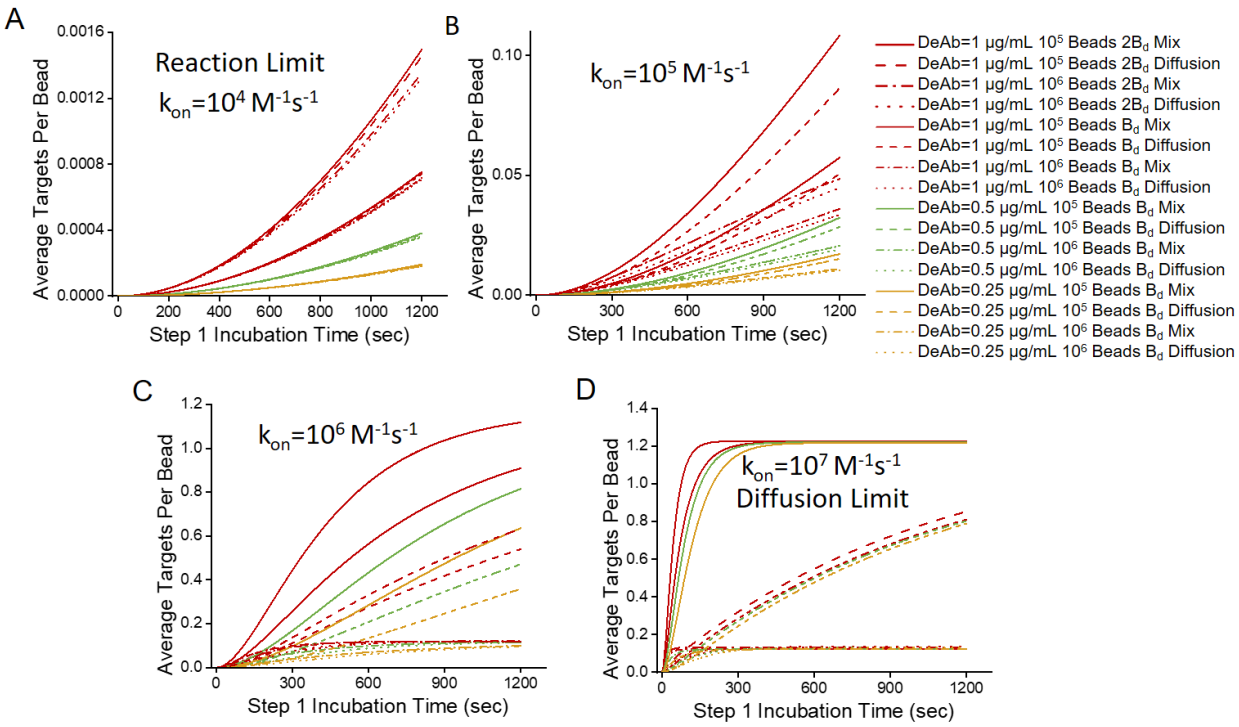

Figure 3.6 Impact of detection antibody (DeAb) concentration, number of magnetic beads per sample, capture antibody binding site density (B_d), and mass transport on immune complex formation kinetics of PEdELISA assay. Here the assay signal output is determined by the average number of targets (capture antibody-antigen-detection antibody immune-complexes) formed per bead as a function of the Step 1 incubation time for different antibody-to-antigen on-rate association constant values: (b) $k_{on} = 10^4\ M^{-1}s^{-1}$, (c) $k_{on} = 10^5\ M^{-1}s^{-1}$, (d) $k_{on} = 10^6\ M^{-1}s^{-1}$, and (e) $k_{on} = 10^7\ M^{-1}s^{-1}$.

For another extreme case where the antibodies have a very strong affinity to the analyte ($k_{on}=10^7$, Figure 3.6D), the immune complex formation kinetics is limited by the mass diffusion of the originally unbound antigen and detection antibody molecules. Compared to the incubation time, the mass transport condition, the number of beads, and the reaction volume size are more dominant factors affecting the assay readout in the "diffusion-limited" regime. For example, with a large number of beads (10^6) in a small sample volume (20µL), the reaction is shown to quickly reach the equilibrium state within 2 min due to the fast reaction rate and the small number of target molecules per bead. This is especially the case we wish to avoid in the digital immunoassay. In the "diffusion-limited" regime, a depletion region growing near the bead surface over time is the

primary factor limiting the transport of target molecules to the capture sites from the far-field. Enhancing mass transport of these molecules through active mixing helps reduce the depletion region growth.

Commercially available antibodies for cytokine detection generally have affinity values falling between those in the above two extreme cases(130). Based on our study here, we concluded that a strategy of preparing beads densely coated with capture antibody molecules, using a small number of these beads in a relatively large sample volume, and enhancing mass transport by active mixing would help achieve ultrafast PEdELISA assay without sacrificing its sensitivity.

3.3.3 Analytical validation of the assay.

To experimentally characterize the PEdELISA assay performance, we selected four signaling cytokine biomarkers involved in the progression of cytokine release syndrome (CRS), a significant complication of CAR-T that impacts morbidity and mortality (131, 132): IL-6; TNF-α; IL-2; and MCP-1. we first spiked four different types of buffers with 100pg/mL each cytokine: the 1x ELISA diluent (1% BSA, 0.05% Tween20), 10%, 25% and 50% fetal bovine serum (FBS), examining the impact of the different levels of background protein on the digital immunoassay signal pertaining to these fluids (Figure 3.7A-D). We calculated the signal-to-noise ratio (SNR), which is defined as the measured signal divided by the average blank signal + 3σ. In general, a larger surface blocking effect, perhaps, owing to the presence of albumin, was observed for serum media, which resulted in a slightly lower spike-in signal and background noise compared to the ELISA buffer. However, there is no significant difference in the SNR value between the different media groups ($P>0.1$ n=5-8, one-way ANOVA, Figure 3.7E). Therefore, we selected 25% FBS as the assay buffer for recombinant protein dilutions to mimic the serum detection background.

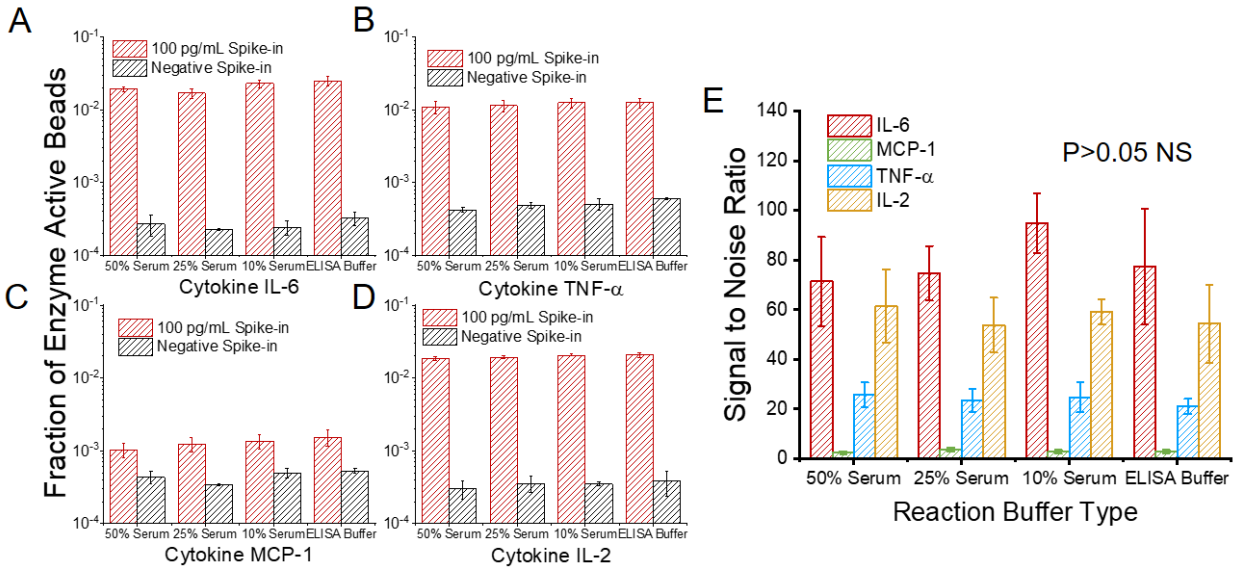

Figure 3.7 PEdELISA assay medium tests for 1x ELISA buffer, 10%, 25%, and 50% fetal bovine serum (FBS) spiked with 100 pg/mL of (A) IL-6, (B) TNF-α, (C) MCP-1, and (D) IL-2. All the tests were performed with the total assay incubation time of 5min+30s. (E) Signal-to-noise ratio (SNR) of IL-6, TNF-α, MCP-1, and IL-2 measurements in different media. The SNR value represents the ratio of the spike-in signal to the background (negative control) signal. The serum was diluted using the 1x ELISA buffer to prepare the 10%, 25%, and 50% serum media. In general, a larger surface blocking effect, perhaps, owing to the presence of albumin, was observed for serum media, which resulted in a slightly lower spike-in signal and background noise compared to the ELISA buffer. However, there is no significant difference in the SNR value between the different media groups (P>0.05 n=5-8, one-way ANOVA).

Figure 3.8A-D show standard curves for the four cytokines ranging from 0.32 pg/mL to 5 ng/mL in 25% FBS with the Step 1 incubation time varying from 60 to 300 sec while fixing the Step 2 incubation time at 30 sec. To push the limit of measurement speed, we even tested and succeeded the assay with 15-sec (Step 1) and 30-sec (Step 2) incubation times by simply mixing all three reagents (detection antibody, avidin-HRP, antigen) with magnetic beads (1-step assay format). As theoretically predicted, the digital readout (the fraction of fluorescence-activated "On" beads to the entire beads) is highly time-dependent and in general, linearly proportional to the analyte concentration. We observed a variation in the signal output depending on the cytokine species. This is likely due to the difference in the antibody pair affinity across the different

cytokines. Notably, the linearity of the assay was confirmed over a three-order-of-magnitude concentration range regardless of the analyte type and quite well maintained even for the 15-sec ultrafast PEdELISA assay of IL-6 (the primary mediator in CRS). Thus, quenching the extremely pre-equilibrated reaction does not compromise our measurement resolution, which makes PEdELISA suitable for practical clinical diagnosis.

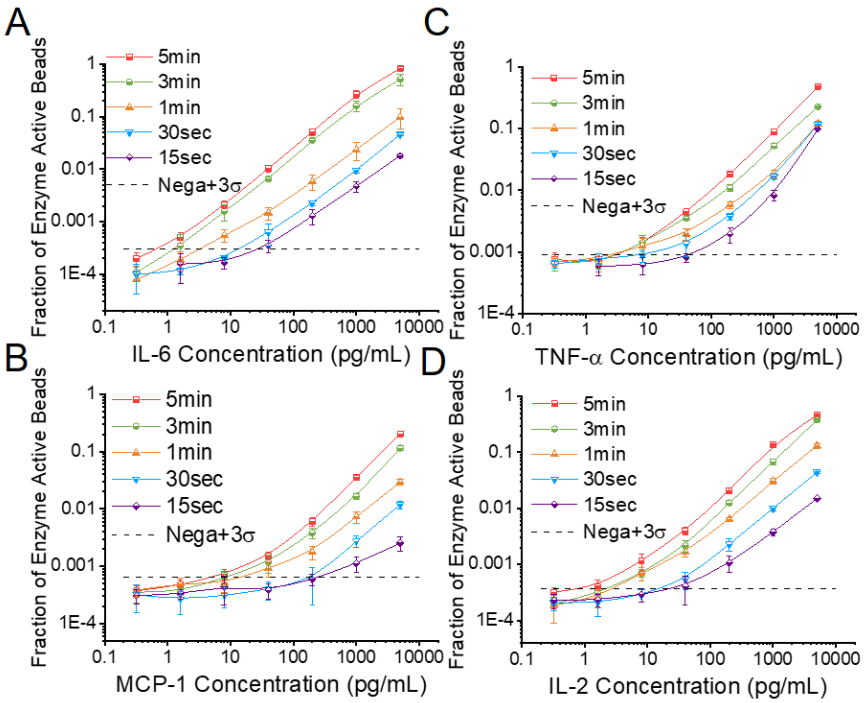

Figure 3.8 Characterization and optimization of PEdELISA assay. PEdELISA standard curves for the four cytokines: (**A**) IL-6, (**B**) MCP-1, (**C**) TNF-α and (**D**) IL-2, with the Step 1 incubation time varying from 60 sec to 300 sec and the Step 2 incubation time fixed at 30 sec. Due to the extreme under-labeled nature of the assay, the 15-sec and 30-sec assays were performed by merging the Step 1 and Step 2 process into a single step by mixing all required reagents. The LOD was determined by concentration from the reagent blank's signal + 3σ (dotted line).

We further validated the assay by comparing measurement results for spiked-in FBS samples between the conventional 3-step sandwich ELISA and PEdELISA with the Step 1 incubation time of 15-sec (Figure 3.9A) and 300 sec (Figure 3.9B). The ground truth (spike-in) value of the analyte concentration was set between 40pg/mL (2pg/mL) to 1000 pg/mL for the 15-sec (300-sec) assay.

We found good agreement between the two methods for both the 15-sec (R^2=0.92) and 300-sec (R2=0.96) assays.

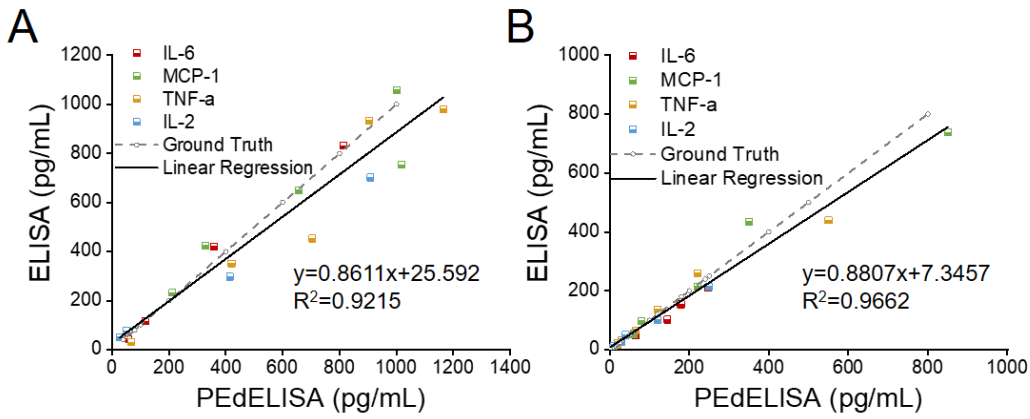

Figure 3.9 Correlation between PEdELISA and conventional sandwich ELISA tests for the four cytokines using spike-in recombinant proteins in 25% fetal bovine serum: (A) 15-sec PEdELISA incubation time (R^2=0.92), (B) 300-sec PEdELISA incubation time (R^2=0.97). The ground truth is plotted in dotted line with scattered pre-determined spike-in concentrations.

Table 3.3 Limit of detection (LOD) and standard root mean square coefficient of variance (RMS CV) of 15-sec and 5-min PEdELISA. The LOD was determined by reagent blank's signal + 3σ.

Cytokine Type	Patient Sample Volume (μL)	Assay Blank+3σ (%)	LOD 15-sec (pg/mL)	LOD 5-min (pg/mL)	Patient Assay standard RMS CV (%)
IL-6	5	0.03034	25.9	0.58	17.3
MCP-1	5	0.06402	333.2	8.29	27.5
TNF-α	10	0.09152	96.7	2.20	24.4
IL-2	10	0.03671	43.9	1.22	17.8

Considering the noise floor of our experimental setup, we theoretically predicted the minimum incubation time for a given target value of LOD using our model and compared it with our experimental data (Figure 3.10). An excellent match was found between the experimental data and the theoretical curves with the assumption of typical antibody affinities ranging from 10^{-9}-10^{-10} M. We observed and established a trade-off relationship between the LOD and incubation time of the digital assay. With an incubation time < 60 sec, it becomes difficult to precisely control the assay

timing, which tends to cause more error to our measurement. Therefore, we selected a 300-sec incubation time for the later CAR-T patient study to maintain a high sensitivity and reliability.

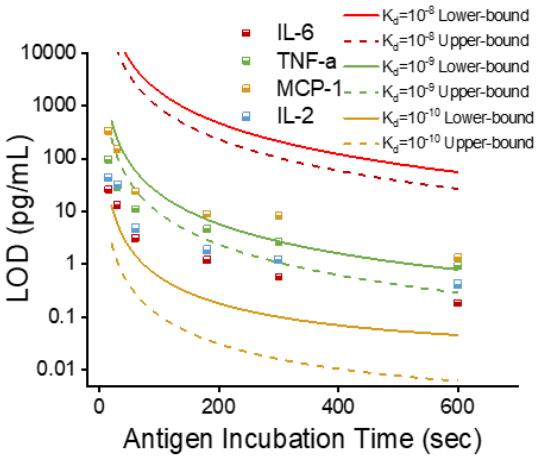

Figure 3.10 Theoretical (line) and experimental (scatter) LOD of PEdELISA as a function of the Step 1 incubation time for four cytokines.

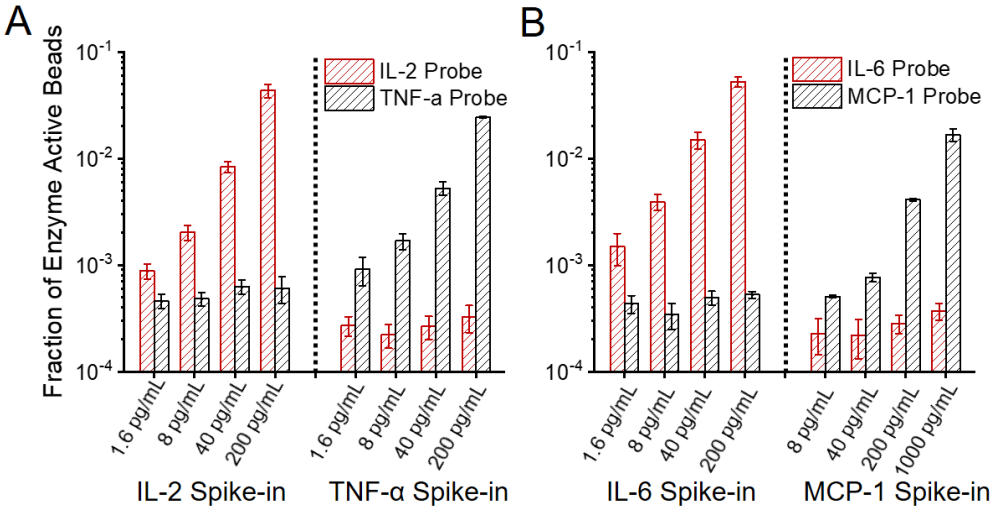

Figure 3.11 Dual-plex PEdELISA specificity determined for combinations of (a) IL-6 and MCP-1 (b) TNF and IL-2 with a 5-min incubation process. Only one type of cytokine was spiked-in into each medium and signals were measured for both probes in the dual-plex PEdELISA assay. Considering the relatively weak antibody-antigen affinity of MCP-1, the spike-in concentration of MCP-1 was set to be 5 times higher than those of the other three cytokines.

Additionally, we verified the dual-plex assay's specificity by quantifying the different antibody pair's cross-reactivity (Figure 3.11). The assay LODs and the root mean square coefficient of

variance (RMS CV%) accumulated over the titration experiments for the four cytokines are summarized in Table 3.3.

3.3.4 Longitudinal biomarker profile measurement for septic mice.

To demonstrate our sample-sparing capability (5 µL), we applied the PEdELISA assay to measure serum biomarkers in a mouse model of sepsis. Frequent, longitudinal monitoring of serum biomarkers in a living mouse is impossible with current gold-standard ELISA technology, as it requires ~0.5 mL of whole blood (for duplicate assay) for each time point, which exceeds the amount feasible to sample consistently and longitudinally from a single mouse. As a result, the conventional approach for such longitudinal studies is to sacrifice mice at each time point to collect sufficient blood, comparing across mice for different time points. For this test, we studied a mouse model of CLP-induced septic shock, which provides a clinically realistic model of sepsis involving polymicrobial infection. In this model, the cecum is ligated at 50, 75, and 100% of the total length (Figure 3.12A) (133) (see 3.2.6 Materials and Methods). We developed and validated a PEdELISA assay (Figure 3.12B) for quantifying the sepsis biomarker, citrullinated histone H3 (CitH3). Catalyzed by peptidylarginine deiminase (PAD), CitH3 has recently been identified as an early step in neutrophil extracellular traps (NETs)-induced immune cell death (NETosis) in response to infection (134). We monitored the dynamic variations of serum CitH3 in four mice with different CLP-induced septic shock severity over their lifetimes (Figure 3.12C). Blood samples were collected through the tail vein every 4-5 hours from 0, 1, 5, 10 hr until death. To minimize and control for any effects of repetitive tail vein blood sampling on disease progression, only 15 µL of whole blood was collected through a capillary tube at each time point, and samples from a sham mouse without CLP were analyzed following the same surgical procedure. Blood samples were processed to obtain 5-7 µL serum and were then subsequently quantified by the PEdELISA.

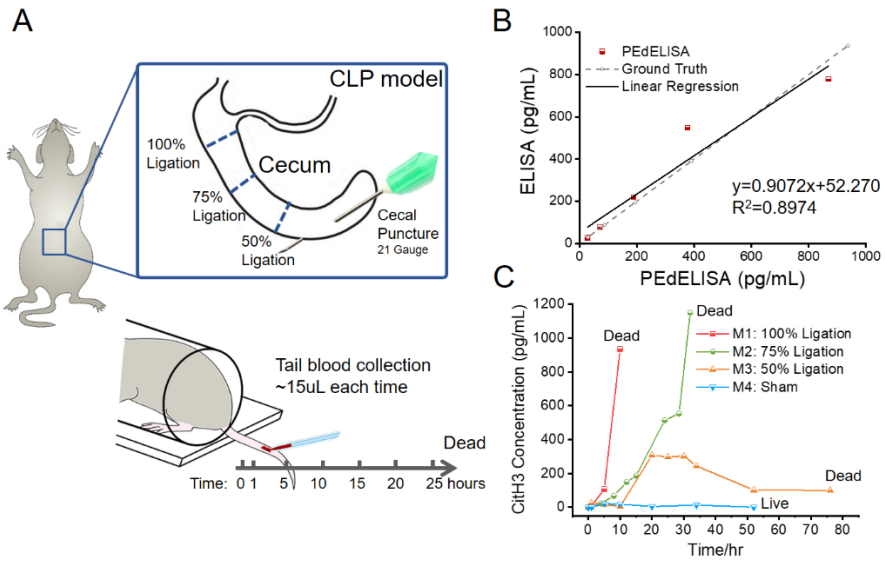

Figure 3.12 Fine-time monitoring of CitH3 on living mice (M1-4) with cecal ligation puncture (CLP). (A) CLP and mouse blood collection procedures. To induce different septic shock severity, the cecum was punctured and ligated at 100%, 75% and 50% of its total length. Around 15 µL of tail blood was collected at 0, 1, 5, 10, 15, 20 hr time points until the mouse's death. (B) Correlation between PEdELISA and conventional sandwich ELISA for the CitH3 assay using a 10% sham mouse serum spiked with recombinant peptide (C) longitudinal CitH3 profiles of the four mice: 100%, 75%, 50% ligation, and sham over their lifetimes.

For the 100% CLP mouse, a significant increase of CitH3 was observed at 5 hr time point (106.6 pg/mL) and the mouse was found dead within 12 hr. For the 75% CLP mouse, the increase of CitH3 was relatively delayed comparing to the 100% CLP mouse. But CitH3 continued to increase and reached a peak value of 1149.2pg/mL at around 32 hr when the 75% CLP mouse died. For the 50% CLP mouse, no significant increase of CitH3 was observed in the first 10 hr, but then it started to increase between 10 and 20 hr and reached its plateau (~300pg/mL) at 20-30 hr. We observed that the physical condition of the 50% CLP mouse recovered at 24 - 48 hr, and the CitH3 level went down during that period. However, its condition quickly became worse after 70 hr and was found dead at 76h. For the sham case, the CitH3 level stayed low < 21.5pg/mL and the mouse stayed alive during the entire experiment.

3.3.5 Near-real-time multiplexed cytokine monitoring of post-CAR-T cell infusion CRS.

Finally, we applied PEdELISA to real-time monitor the IL-6, TNF-α, IL-2, and MCP-1 profiles of hematological cancer patients showing severe (Patient A), moderate (Patient B), and mild (Patient C) CRS symptoms after CAR-T cell therapy following a pre-approved sample collection protocol (see Methods). CRS is a form of systemic inflammatory response accompanied by a high level of inflammatory cytokines released into the bloodstream by activated white blood cells. It can rapidly evolve (i.e., within 24-48 hours) from manageable constitutional symptoms (grade 1) to more severe forms (grade 2-4) (135), for which rapid and sensitive serum cytokine measurements could direct urgent interventions (136). Here, we performed real-time cytokine profile measurements within 2 hours after blood samples were freshly drawn in ICU with a serum sample to answer time in around 30 minutes (Figure 3.13A). To ensure the highest accuracy and sensitivity for these clinical measurements, we chose the total incubation time to be 300-sec (Step 1) + 30-sec (Step 2) in the 2-step assay format. We first assayed banked CAR-T patient serum samples (n = 23) with unknown analyte concentrations and validated them by ELISA (Figure 3.13B). The data between these two methods show an excellent linear correlation (R^2=0.96), which confirmed the accuracy of the 2-step PEdELISA assay for human biomarker detection. Then, we performed real-time measurements which captured the patients' complex immune responses to the immunomodulatory interventions manifested by the time-course variations of the cytokine profiles (see Figure 3.13C-E). The dynamic behavior of these responses vary from patient to patient and decisions for treatment of CRS in these patients were made solely based on clinical criteria (e.g., CRS grades) summarized in Appendix A, which did not involve any serum cytokine data.

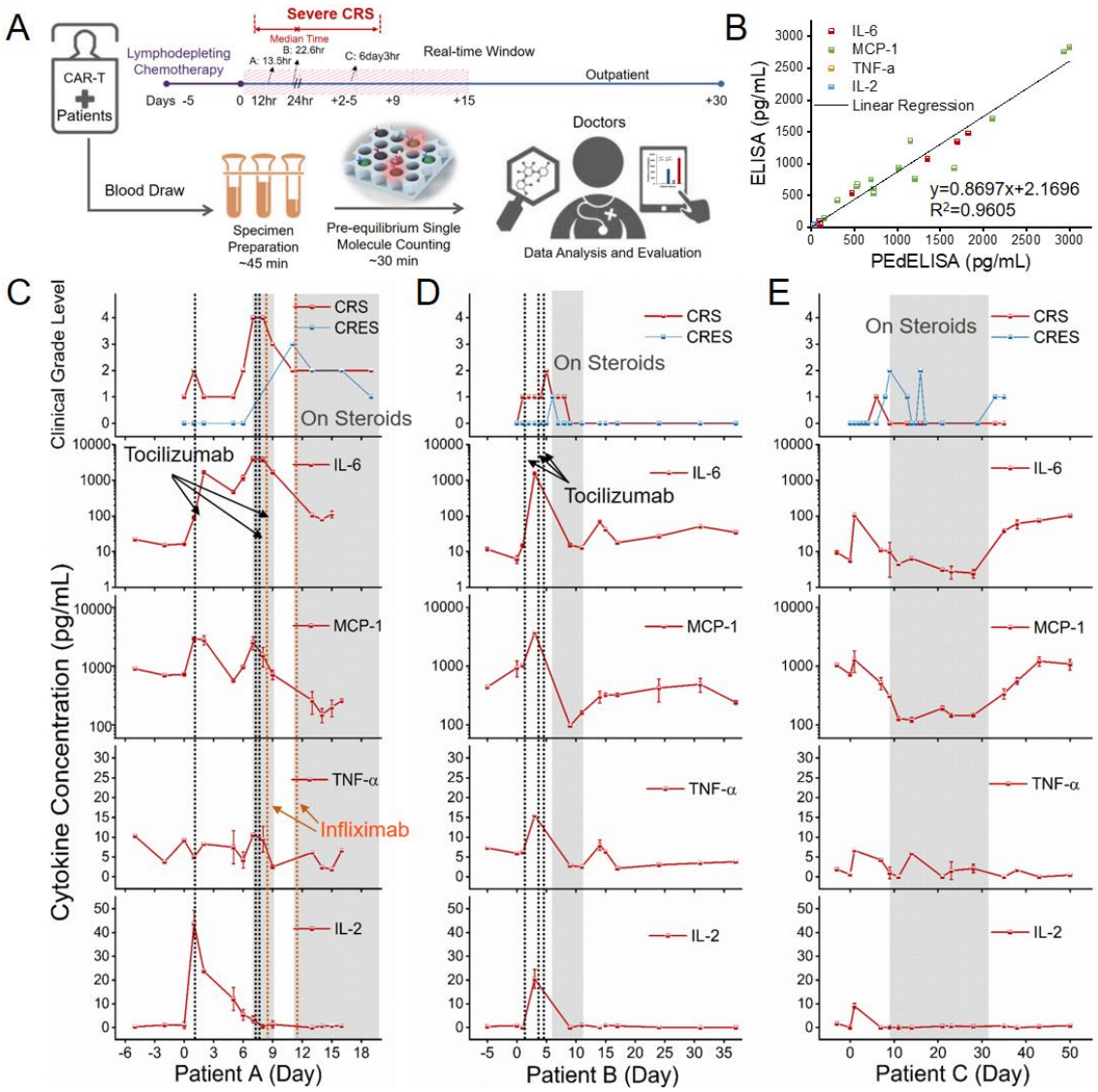

Figure 3.13 Near-real-time molecular monitoring of multi-cytokines of hematological cancer patients under CAR-T cell therapy. (A) Timeline of the hematological cancer patients received CAR-T cell therapy. Daily blood draw in general started five days before the infusion for baseline collection until the patient was discharged. For the real-time monitoring, the sample was first processed within 45 min of blood draw to extract serum and then tested by the PEdELISA within an hour. The data typically became available for clinicians within 2-3 hours from the initial point of patient blood collection. The initial onset of CRS and the development of neurotoxicity of three patients were labeled along the timeline. (B) Good agreement (R^2=0.96) between 300-sec PEdELISA and ELISA was found for measurements of selected unknown CAR-T patient samples at different time points for four cytokines. Time-series profiles of CRS and CRES grade, IL-6, MCP-1, TNF-α, and IL-2 for (C) Patient A (grade 4 severe CRS), (D) Patient B (grade 2 mild CRS) and (E) Patient C (grade 0-1 very mild-CRS). Day 0 represents the day of CAR-T cell infusion. Data before Day 0 represents the baseline. The dotted line represents the time point when anti-cytokine drug tocilizumab (Anti-IL-6R), infliximab (Anti-TNF-α) were administered. The shaded region marks the period that the patient was received dexamethasone (corticosteroid). These data do not account for a time lag of a few hours (or occasionally 8-12 hours) between the points of CRS grade recording and blood draw.

For Patient A, who had a high tumor burden, the time to initial onset of CRS was as short as 13.5 hours. We found that the MCP-1 and IL-2 levels rose rapidly and reached the peak values (MCP-1 2947pg/mL; IL-2 39.72pg/mL) within 24 hours after CAR-T infusion, which is correlated with the patient's grade 2 CRS accompanying the fever (39.3 ℃) on Day 1 (Figure 3.13C). We also observed the continuous rise of IL-6 transiently after the first tocilizumab administration (Day 1) from 89.9pg/mL (Day 1) to its peak level of 1676 pg/mL through Day 2. A similar trend was also noted for Patient B (Figure 3.13D), who received the first dose on Day 2 with grade 1 CRS, and the peak (1546 pg/mL) was detected on Day 3. Patient A later developed grade 3-4 life-threatening CRS on Day 6-9 and was readmitted into the ICU. During this period, the IL-6 level was found to approach an extremely high level of 4383pg/mL (Day 7) and 4189pg/mL (Day 8), and MCP-1 also reached its second peak 2103pg/mL, despite the fact that Patient A was administered with multiple immunosuppressing agents (see Appendix A). Interestingly, we did not see a significant rise of TNF-α and IL-2 during the second CRS peak. Later, the patient was diagnosed with grade 3 CRES (CAR-T cell-related encephalopathy syndrome) on Day 11. For Patient B (Figure 3.13D), one peak for all four cytokines was observed during the first eight days after CAR-T cell infusion, which is correlated with the patient's clinical symptoms during this period (Grade 1-2 CRS). Patient C did not develop CRS until 6 days after the CAR-T cell infusion, although a slight elevation for all four cytokines was observed on Day 1 (Figure 3.13E). However, Patient C developed prolonged neurotoxicity starting from Day 8 and was therefore on steroids from Day 9 to Day 33. During this period, all four cytokines stayed at low levels. After steroids were stopped, Patient C's IL-6 and MCP-1 levels rose back from Day 35 to Day 50 and grade 1 neurotoxicity relapsed. We sorted the time-series cytokine data in Figure 3.13 all combined for the three CAR-T patients into non-CRS and CRS (grade 1 or higher) groups (Figure 3.14). We found

a clear group difference among IL-6, MCP-1 (P<0.001) and IL-2 (P=0.0059) concentration levels, even including the time points when CRS-suffering patients were put on steroids or immunosuppressive agents. However, for TNF-α, we did not observe a significant statistical difference (P = 0.142) and the data show a consistently low level of TNF-α for both groups across all the three patients.

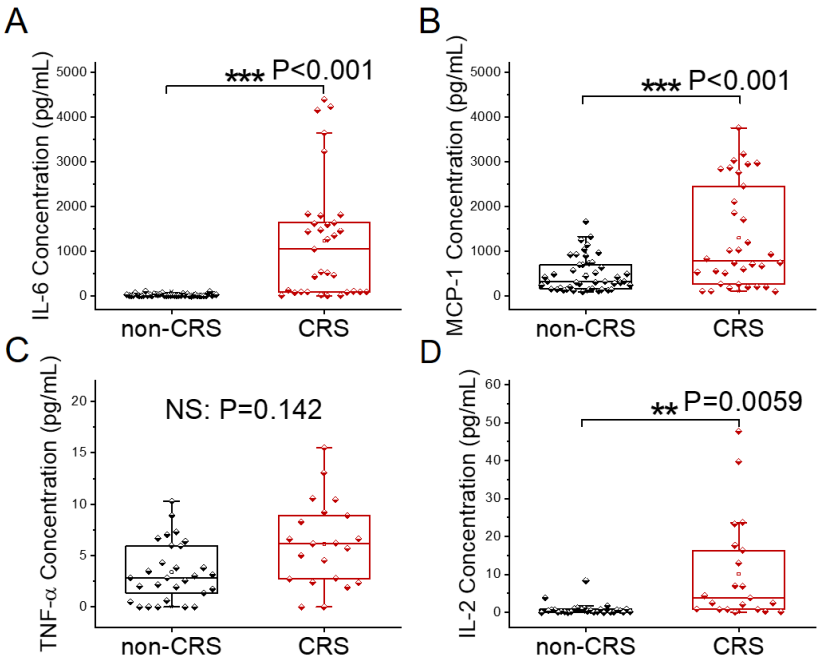

Figure 3.14 Group comparison (non-CRS vs CRS) of the three CAR-T cell therapy patients for (**A**) IL-6, **(B**) MCP-1, (**C**) TNF-α, and (**D**) IL-2. The statistical analysis between the two data groups was performed by one-way ANOVA comparing means with the Tukey test. IL-6 (P<0.001), MCP-1 (P<0.001) and IL-2 (P=0.0059) levels were significantly higher in CRS condition than in non-CRS condition. TNF- α level was not significant (P=0.142). Note that the data include those obtained at the time points when CRS-suffering patients were put on steroids or immunosuppressive agents (tocilizumab, infliximab).

3.4 Discussion

While precision medicine approaches for cancer and genetic diseases have been remarkably successful (116, 117, 137), the area of clinical care of acute, severe systemic immune disorders has seen highly limited benefits, owing in part to the lack of sufficiently accurate, sensitive and clinically practical biomarker measurement technology (118). Real-time monitoring of acute

immune responses in patients over time poses significant technical challenges. In addition to a need for high speed and sensitivity, it requires the ability to capture temporal cytokine profiles varying over a wide concentration range between 10 fM and 1 nM for various cytokines. Meeting such stringent requirements, PEdELISA shows promise to enable early detection and intervention of the inflammatory response accompanying sepsis and CRS. Unlike conventional ultrafast immunoassay approaches, PEdELISA achieves high speed by applying single-molecule counting for an antibody-antigen-antibody immune-complex formation quenched at an early pre-equilibrium state. As a result, total assay incubation time has been shortened from a few hours to a few minutes while achieving high sensitivity and linearity at a clinically relevant dynamic range. Our multi-physics FEA modeling analysis validated that the 2-step transient assay format of PEdELISA can maintain a linear relationship between the analyte concentration and the assay readout regardless of the snapshot acquisition timing. Additionally, the modeling predicted very well the minimum required incubation time for the desired detection limit, which guided the digital assay design. For IL-6, the primary mediator of CRS, we experimentally showed that the entire assay incubation time can be as short as 15 sec with a LOD of 25.9 pg/mL while maintaining a 4-order dynamic range up to 10 ng/mL. To our knowledge, the immunoassay demonstrated here is faster than any current ELISA-based assays with comparable sensitivity.

Using the PEdELISA platform, we successfully demonstrated two applications: (i) longitudinal measurement of the protein biomarker CitH3 in the same, live animal (i.e., without need for mouse sacrifice) in a mouse model of sepsis with a serum volume as small as 5 μL, and (ii) rapid, high-sensitivity, near-real-time multiplex monitoring of CRS relevant circulating cytokines (IL-6, TNF-α, IL-2, and MCP-1) for three hematological cancer patients showing severe and moderate CRS symptoms after CAR-T cell therapy. With conventional ELISA or Luminex

methods, time-course biomarker measurement is only achieved by retrospective tests using banked samples. In contrast, PEdELISA continuously provided real-time data for blood samples freshly collected from mice and human patients with a high time-resolution limited only by blood sampling frequency (1-5 hr for mice and 24 hr for humans, over most of the course of our studies).

Our study using the CLP septic mice demonstrated the utility of the PEdELISA in a setting where blood sample volume is extremely limited. The demonstrated sample-sparing capability enabled us to longitudinally monitor the distinct characteristics of the CitH3 biomarker profiles in mice experiencing different illness severities (Figure 3.12C). CitH3 is shown to be a common mediator in various inflammation signaling pathways that trigger the neutrophil response to microbial infection (138, 139). Thus, temporal CitH3 profiles have the potential to indicate the progression and severity of infection-induced septic shock. Interestingly, we observed a decrease in the CitH3 level in the late phase of the measurement for the mouse with 50% ligated-cecum, which represents a condition for inducing a low-severity state of sepsis. The reason remains unknown but may potentially be revealed by a finer blood draw in the later phase of sepsis progression. In addition to sepsis, the technology enables longitudinal serum biomarker research on a broad range of mouse models of disease, and is also relevant to critical care of infants or pediatric patients, from whom only limited blood volumes can be drawn.

The PEdELISA test for human patients (Figure 3.13C-E) captured two CRS peaks after the CAR-T infusion for Patient A with severe CRS who had high tumor burden. The significantly elevated IL-6 and MCP-1 levels appearing at the second peak were associated with the severe, Grade 4 CRS experienced by the patient. Specifically, upon the first administration of tocilizumab (anti-IL-6R), we observed a temporary increase and then an eventual decline in serum IL-6 level for Patient A and B. In the future, such data if obtained from studies of larger numbers of patients,

could reflect pharmacodynamic information regarding the drug's activity in inhibiting IL-6 receptors (40), and potentially be used to predict treatment outcome. Interestingly, no elevation was observed for both TNF-α and IL-2 in Patient A during the second CRS grade peak. The reason remains unknown, although it could be partially attributed to the heavy dose of the general immune-suppressive corticosteroids the patient had received during this period. The mismatch between the detected low level of TNF-α and the clinical timing of infliximab treatment (anti-TNF-α) opens up the possibility of biomarker-guided therapy to administer the correct targeted therapy at the optimal timing. We envision real-time cytokine profile data enabled by the PEdELISA method may in the future facilitate the early identification of patients with evolving CRS, to allow for more targeted and timely anti-cytokine treatment, as well as providing real-time feedback regarding cytokine levels after initiating treatment.

Moving forward, further development of several aspects of our pre-equilibrium digital assay technology will be important for enabling direct implementation in the clinical setting. First, the manual sample preparation, handling, and washing procedures of the assay could be automated and integrated. All the processes of our test from the initial blood draw to the end result delivery currently takes up to 2 hours, including sample preparation and transportation. Our future work will integrate a finger-pricked inlet, an on-chip plasma separation unit, and a precisely controlled sample/reagent handling automation system into the PEdELISA platform for near-bedside operation. This would allow the whole test to be completed with a blood draw-to-answer time < 30 min and truly enable "real-time" biomarker detection. Second, the current multiplex capacity could be extended by microfluidics-based assay miniaturization and operation. Multiplex measurement to screen multiple cytokines and other biomarkers at different time points would allow us to capture a full picture of the complex pathophysiology of sepsis and CRS over time.

Chapter 4

Machine Learning-Based Cytokine Microarray Digital Immunoassay Analysis

4.1 Introduction to the Study

Over the past few years, the approach of providing personalized treatment for severely ill patients based on their individualized molecular profiles has received considerable attention as a next step to advance critical care medicine (118, 140, 141). Progress has been made in identifying predictive and prognostic protein biomarkers in critical care which holds great promise in patient stratification (120, 142), disease monitoring (143, 144), and therapy development (141, 145). For example, Huang et al (16) tested patients infected with the 2019 novel coronavirus (COVID-19) and reported that a panel of eight plasma cytokines showing significantly hightened levels allowed them to distinguish a group of severely ill patients from a group of mildly ill patients. However, even with the discoveries of these biomarkers, the medical community still falls behind with adopting the precision medicine approach to treat life-threatening acute illnesses, such as cytokine release syndrome (CRS), acute respiratory distress syndrome (ARDS), which are frequently associated with the 2019 novel coronavirus (COVID-19) (16, 146), due to the lack of a sensitive molecular profiling tool to quickly guide clinical decisions or interventions with a near-real-time assay turnaround (140). Additionally, to monitor the highly heterogeneous and time-pressing illness conditions, high multiplex capacity is equally important as sensitivity and speed for

improving diagnosis and prognosis accuracy with rich, comprehensive information on multiple biomarker profiles (16, 131, 132, 140). Currently, the commonly used clinical tools for multiplex serum/plasma protein analysis (147), including the bead-based assay coupled flow cytometry and the western blot, fall short of achieving the performance needed for critical care as they require a long assay time (>4 hrs), and laborious steps with limited sensitivity.

Researchers have developed rapid (37, 39, 105, 148), point-of-care (32, 36, 149), multiplex (31, 63) immunoassays powered by microfluidics. Nonetheless, it is still challenging for these assays to simultaneously achieve a combination of high multiplexity and sensitivity with a rapid assay turnaround time in a clinical setting. By counting single-molecule reactions in fL-nL-volume microwells or droplets (52, 122, 124), digital immunoassays can provide unprecedented sensitivity (sub-fM detection) for biomarker analysis. Contrary to the conventional belief based on Possion distribution theory (56), our recent study (67) demonstrated that it is feasible to extend the single-molecule counting approach to achieve near-real-time protein biomarker profiling at a clinically relevant pM-nM range by quenching reagent reaction at an early pre-equilibrium stage with an incubation process as short as 15-300 sec. However, existing digital immunoassay platforms (150) have limited multiplex capacity (up to 6-plex). The current method (122, 151) utilizes fluorescence dye-encoded beads to identify different analytes. Unfortunately, the nature of binary-based statistical counting brings a few critical challenges to multiplexing digital immunoassays with this method. First, the assay typically requires a large number of beads (e.g. Simoa uses 100,000 beads per plex (150)) for reliable analyte quantification. Mixing and counting such a large number of multi-color-encoded beads tends to cause false signal recognition due to optical crosstalk or non-uniform color coating. Second, increasing multiplexity while keeping the assay's sensitivity and accuracy additionally requires a large number of microwell arrays to accommodate the large

number of beads. This becomes impractical with the current platform as it demands a significantly increased assay device footprint and an image area size. Third, the assay also encounters a significant bead loss during the digitization process partitioning the beads into sub-volumes after the initial reaction process performed for bulk reagent volume in a cuvette (100 μL). All of these issues prohibit the translation of a cheap, robust, point-of-care multiplexed digital assay platform into near-patient applications, thus necessitating a new strategy.

Here, we have developed a highly multiplexed digital immunoassay platform, termed the "pre-equilibrium digital enzyme-linked immunosorbent assay (PEdELISA) microarray." The PEdELISA microarray analysis integrates on-chip biosensors with a small footprint to minimize the number of images that are needed to read and fully automates the signal counting process, both of which are critically necessary for overcoming the bottlenecks against multiplexing digital assays. The analysis incorporates a powerful microfluidic spatial-spectral encoding method and a machine learning-based image processing algorithm into multi-biomarker detection. The spatial-spectral encoding method confines color-encoded magnetic beads into the arrayed patterns of microwells on a microfluidic chip. The locations of the microwell patterns on the chip indicate which target analytes are detected by trapped color-coded beads. In contrast to the existing digital immunoassay protocol, the fully integrated microfluidic architecture allows the assay reaction to be performed entirely on-chip (no bead loss) at an early pre-equilibrium state, which only requires a sample volume < 10 μL, a 5-min assay incubation and a 75 mm × 50 mm chip size. Based on a convolutional neural network (CNN), the machine learning algorithm permits unsupervised image data analysis while resolving false signal recognition accompanying the multiplexing of digital immunoassays. Employing these biosensing schemes, the PEdELISA microarray platform allows us to simultaneously quantify a large panel of biomarkers in half an hour without sacrificing the

accuracy. We used the platform to obtain longitudinal data for blood samples from human patients experiencing cytokine release syndrome (CRS) after chimeric antigen receptor T cell (CAR-T) therapy. The data signify the time-course evolution of the profiles of 14 circulating cytokines over illness development. With its near-real-time assay turnaround and analytical power, the platform manifests great potential to enable acute immune disorder monitoring that guides timely therapeutic interventions.

4.2 Materials and Methods

4.2.1 Materials.

We purchased human IL-6, TNF-α, IL-2, IL-8, IL-13 capture, and biotinylated detection antibody pairs from Invitrogen™, and IL-1α, IL-1β, IL-10, IL-12, IL-15, IL-17A, IFN-γ, GM-CSF and MCP-1 from BioLegend. We obtained Dynabeads, 2.7μm-diameter carboxylic acid, and epoxy-linked superparamagnetic beads, avidin-HRP, QuantaRed™ enhanced chemifluorescent HRP substrate, Alexa Fluor™ 488 Hydrazide, EDC (1-ethyl-3-(3-dimethylaminopropyl) carbodiimide hydrochloride), Sulfo-NHS (Sulfo-N-hydroxysulfosuccinimide), MES (2-(N-morpholino)ethanesulfonic acid) buffered saline, bovine serum albumin (BSA), TBS StartingBlock T20 blocking buffer, and PBS SuperBlock blocking buffer from Thermo Fisher Scientific. We obtained Phosphate buffered saline (PBS) from Gibco™, Sylgard™ 184 clear polydimethylsiloxane (PDMS) from Dow Corning, and Fluorocarbon oil (Novec™ 7500) from 3M™.

4.2.2 Antibody Conjugation to Magnetic Beads.

We prepared the non-color encoded magnetic beads by conjugating epoxy-linked Dynabeads with the capture antibody molecules at a mass ratio of 6 μg (antibody): 1 mg (bead). The Alexa Fluor™ 488 (AF488) encoded magnetic beads were prepared by first labeling carboxylic acid-

linked Dynabeads with AF 488 Hydrazide dye and then by conjugating the beads with capture antibody at a mass ratio of 12 μg (antibody): 1 mg (bead) using standard EDC/sulfo-NHS chemistry. Detailed protocol has been described in the previous chapter (67). We stored the antibody-conjugated magnetic beads at 10 mg beads/mL in PBS (0.05% T20 + 0.1% BSA + 0.01% Sodium Azide) buffer wrapped with an aluminum foil sheet at 4 °C. No significant degradation of these beads was observed within the 3-month usage.

4.2.3 Microfluidic Chip Fabrication and Spatial-Spectral Encoding.

The first step of the PEdELISA microarray chip fabrication involved the construction of three different PDMS layers (Figure 4.1). The first PDMS layer has arrays of hexagonal biosensing patterns with microwell (d=3.4 μm) structures (multi-array biosensor layer). The second one has bead settling flow channels of 2500 μm in width, 70 μm in height, and 65 mm in length (bead setting layer). The third one has channels of 4500 um in width, 90 μm in height, and 30 mm in length for the detection of analytes in loaded samples (sample detection layer). First, we constructed SU-8 molds for these three PDMS layers on separate oxygen plasma treated silicon wafers by standard photolithography. This process involved depositing negative photoresist (SU-8 2005, SU-8 2050, MicroChem) layers at different spin coating speeds to form the designed thicknesses for the PDMS microstructure patterns. Subsequently, a precursor of PDMS was prepared at a 10:1 base-to-curing-agent ratio. To construct the multi-array biosensor layer, we deposited a thin PDMS precursor film (~300 μm) onto the microwell-patterned SU-8 mold by spin coating, baked it overnight (60 °C), and then attached it to a pre-cleaned 75×50mm glass substrate through oxygen plasma treatment. We made both of the bead settling layer and the sample detection layer by pouring the PDMS precursor over the other SU-8 molds in a petri dish and then baked overnight (60 °C).

The second step involved the settlement of beads in the microwells of each hexagonal patter on the multi-array biosensor layer. We first aligned and attached the bead setting layer to the multi-array biosensor layer on the glass substrate. Then, we prepared 7 sets of a 25 uL mixture of AF488 encoded beads (anti-cytokine 1) and non-color encoded beads (anti-cytokine 2) at the concentration of 1mg/m in vials for the 14-plex detection. This was followed by loading each of the 7 mixtures into one of the microfluidic channels in the bead settling layer (Figure 4.1A). After waiting for the beads to settle in the microwells for 5 min, we washed the bead settling channels with 200 uL PBS-T (0.1% Tween20) to remove the unstrapped beads thoroughly. At this step, we ensured that the microwells were filled with the beads at a sufficient rate (typically above 50%) using an optical microscope. (If not, the bead mixture solution was reloaded and washed again.)

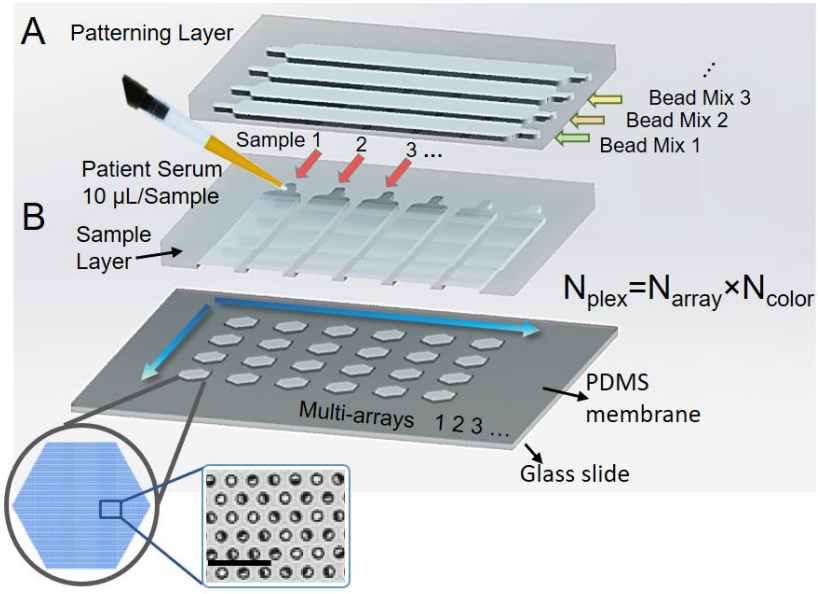

Figure 4.1 Multiplexing the digital immunoassay by constructing a PEdELISA microarray chip based on the concept of microfluidic spatial-spectral encoding: (A) Trapping beads into microwells of the arrayed biosensing patterns on the multi-array biosensor layer. Mixtures of fluorescently encoded beads of N_{color} colors are loaded to the microfluidic channels on the bead settling layer. (B) Peeling off the bead settling layer from the multi-array biosensor layer, and attaching the sample loading layer on the multi-array biosensor layer. The 90º orientation of the sample loading channels permits each channel to contain an array of biosensing patters of N_{array} types. Loading serum samples to the channels of the sample detection layer with pipettes. The chip arrangement yields a total of $N_{color} \times N_{array}$ plex for the analysis of each sample.

The third step involved the assembly of the chip with the multi-array biosensor and sample detection layers. After the bead setting channels were dried by sucking out the washing buffer using a pipette, we peeled off the bead settling layer from the multi-array biosensor layer and replaced it with the sample detection layer. Here, the sample detection layer was aligned and attached to the multi-array biosensor layer so that its channels were oriented perpendicular to the direction of the channels of the bead settling layer. We then slowly loaded the sample detection channels with Superblock buffer to passivate the PDMS surface and incubate the whole chip for at least 1 hour before the assay to avoid non-specific protein adsorption. The sample detection layer was punched to form inlets and outlets for its channels. The chip was tape cleaned and covered before the assay usage. Finally, serum samples were loaded to the sample detection channels from their inlets (Figure 4.1B).

4.2.4 Patient Blood Sample Collection and Preparation.

Blood samples were collected from patients receiving CAR-T cell therapy and was performed with informed consent under the University of Michigan Institutional Review Boards (IRB) protocol HUM00115179/UMCC 2016.051. Venous blood was collected into a vacutainer containing no anticoagulant on-site at the University of Michigan Medical School Hospital and transported it to a biological lab. After allowing the sample to clot for a minimum of 30 minutes at room temperature, we isolated serum by centrifuging the vacutainer at 1200 × g, for 15 minutes at room temperature. The serum was removed by a pipette, aliquoted into screw cap tubes, and then stored at -80 ºC prior to the assay.

4.2.5 14-plex PEdELISA assay.

All assay reagents were prepared in 96-well plate low retention tubes and kept on ice until use. The reagent preparation involved preparing a mixture of the biotinylated detection antibody (up to

14 cytokines for CAR-T study) in a carrier protein buffer (0.1% BSA, 0.02% Sodium Azide) and storing it at 4C, and preparing an Avidin-HRP solution in a superblock buffer at 100 pM. For the PEdELISA chip calibration, we prepared a mixture of recombinant proteins in 25% fetal bovine serum (standard solution), which was 5x serially diluted from 2.5 ng/mL to 0.16 pg/mL. Prior to the assay, we diluted patient serum samples (5uL) two times with PBS (5uL) to prepare a sample solution. As the first step of the assay, we mixed the sample solution (10 μL) and the biotinylated detection antibody solution (10 μL) (sample mixture) and mixed the 5 titrated standard solutions (10 μL) and the biotinylated detection antibody solution (10 μL) (standard mixtures). Then, we loaded these sample and standard mixtures into the detection channels in parallel and incubated the chip for 300 sec. The signals obtained from the standard mixtures were used for calibrating the biosensors of the chip. The microfluidic channels were then washed with a PBS-T (0.1% Tween20) solution at 50 uL/min by a syringe pump for 2 min. 40 μL of the avidin-HRP solution was then loaded into the channel and incubate for 1 min. The chip was washed again with the PBS-T (0.1% Tween20) solution at 50 uL/min for 5 min. To reduce the interference between Tween20 and the enhanced chemifluorescent HRP substrate (QuantaRed substrate), we exchanged the PBS-T solution remaining in the channes with a 1x PBS solution. After loading 30 μL of the QuantaRed substrate solution, the channels were sealed with 35 μL of fluorinated oil (HFE-7500, 3M). The inlets and outlets of the channels were covered by glass coverslips to prevent evaporation during the imaging process. A programmable motorized fluorescence optical microscopy system was used to scan the image of the bead-filed microwell arrays on the microfluidic chip, identify the bead type (non-color vs. AF488 dyed), and detect the enzyme-substrate reaction activity. This system is composed of a Nikon Ti-S fluorescence microscope (10x objective), a programmable motorized stage (ProScan III), a mercury lamp fluorescence illumination source, a SONY full-

frame CMOS camera (α7iii), and a custom machined stage holder. The motorized stage was pre-programmed to follow the designated path to scan the entire chip (160 images) in 3 sequential steps: 1. Scan the QuantaRed channel (532nm/585nm, excitation/emission) 2. Scan the AF488 channel (495nm/519nm, excitation/emission) 3. Scan the brightfield. It typically took around 5-7 min to scan the entire chip for 10 samples in 16-plex detection.

4.2.6 Training of the Dual-pathway Convolutional Neural Network.

Figure 4.2 shows the training process of our dual-pathway CNN algorithm, which involves data set preparation and 2-step neural network training. We first developed pre-stage neural networks trained with a data set of 3,000 representative locally-cropped (32×32 pixel) images. For each of these images, two types of images (6,000 in total) only showing the labeling information, which are called "masks" were generated by thresholding and manual labeling (Figure 4.2A Labeled). In the pre-stage mask for Pathway 1, all the target pixels representing "On" (Qred+) microwell sites and other sites (defects or background) were labeled as '1' and '0', respectively. In the pre-stage mask for Pathway 2, the defects and other sites were labeled as '1' and '0', respectively. The pre-trained networks were able to identify and segment the labeled objects to some degree of accuracy (i.e., 60-80% "On" wells). But they still lacked the accuracy to extract more in-depth features of the object, such as its shape and fluorescence intensity variations of the objects, and other defects that were hard to identify with the small-scale images.

To further improve the accuracy, we built three second-stage parallel CNN networks to identify AF 488+ pixels, Qred+ pixels, and defects that were trained with 256×256-sized images (around 200 images per network). The labeling masks to be used to train the second-stage networks were generated by the pre-stage neural networks with human correction (see Figure 4.2Bii). By taking into account that the sizes of lithographically patterned microwells and beads were predetermined,

we trained the second-stage networks to accurately recognize these objects independent of their image intensity variations. Additionally, we selected 30 images for each error source caused by optical crosstalk, carefully determined the intensity threshold to set a clear boundary between adjacent microwells for each of these images, and generated second-stage labeling masks.

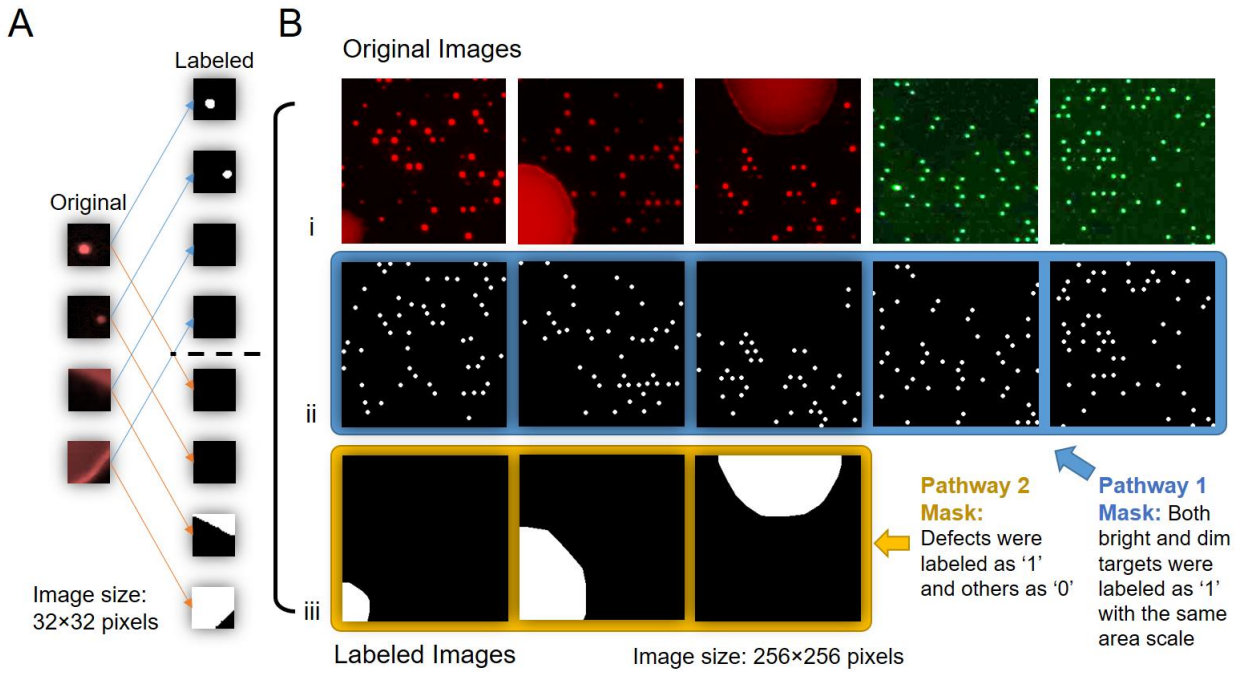

Figure 4.2 Training process of the dual-pathway convolutional neural network (CNN) with semantic segmentation. (A) The data library was carefully pre-selected based on 3000 representative images (32×32 pixels) to pre-train the CNN. The images were first labeled based on global thresholding and segmentation (GTS) and then manually modified based on human supervision. (B) The pre-trained CNN was then used to label a new data library which contains around 200 larger images (256×256 pixels) to further improve the feature extraction and classification accuracy.

As for training the defect recognition-network, we first enhanced the image brightness and contrast to recognize even low-intensity regions. We then applied image dilation for the defect location to ensure the generated mask area is large enough to cover the entire defect area as shown in Figure 4.2iii. Here, only defect locations were labeled as '1' and all others were labeled as '0'. The region labeled as '1' was eventually removed from the total analyzed area to eliminate it from the fluorescence signal counting.

Our neural network contains 5 classes: Qred+ class, AF488+ class, Qred defect class, Qred background class, and AF488 background class. Before training the neural network with the labeling masks above, we also added weight information to each class to further enhance the pixel identification accuracy. We used the inverse frequency weighting method which gives more weights to less frequently appearing classes. The class weight was defined as

$$\text{Classweight} = \frac{N_{image\ total\ pixels}}{N_{class\ pixels}}$$

where $N_{image\ total\ pixels}$ is the number of total image pixels of 256×256 = 65,536, and the $N_{class\ pixels}$ is the number of pixels for each class. This class weighting strategy was added into the neural network training process because the number of $Qred^+$ or $AF488^+$ class pixels were significantly smaller than the number of their total background pixels.

4.2.7 Statistics.

Experiments with both synthetic recombinant proteins (for assay standard curves) and CAR-T patient samples at each time point were performed 3 times (in independent tests) with two on-chip repeats. The standard deviation was calculated to obtain the error bar. Group differences were tested using a two-tailed unequal variance t-test. A p-value of < 0.05 was considered to be statistically significant.

4.3 Results and Discussion

4.3.1 Multiplexed Digital Immunoassay with CNN Image Processing.

The PEdELISA microarray analysis used a microfluidic chip fabricated using polydimethylsiloxane (PDMS)-based soft lithography. The chip contains parallel sample detection channels (10-16) on a glass substrate, each with an array of hexagonal biosensing patterns. The hexagonal shape allows each biosensing pattern to densely pack 43,561 femtoliter-sized

microwells, which fits into the entire field of view of a full-frame CMOS sensor through a 10x objective lens (Figure 4.3**)**. Prior to the assay, we deposited magnetic beads (d = 2.8 μm) encoded with non-fluorescent color (no color) and those with Alexa Fluor® 488 (AF 488) into physically separated microwell arrays. These beads were conjugated with different capture antibodies according to their colors and locations on the chip. In the current design, the arrangement of 2 colors and 8 arrayed biosensing patterns in each detection channel allows the PEdELISA microarray chip to detect 2 × 8 = 16 protein species (16-plex) at its maximum capacity for each sample loaded to the detection channel. Compared with a single color-encoded method, this combination greatly reduces potential optical crosstalk and fluorescence overlap during a signal readout process. The pre-deposition ensures a fixed number of beads to target each biomarker, which allows more accurate digital counting for each biomarker. It also eliminates bead loss during the conventional partition process and achieves nearly a 100% yield in the signal readout for enzyme active QuantaRed^{TM} (Qred)-emitting beads ("On" beads or "Qred+" beads). The microwell structure (diameter: 3.4 μm and depth: 3.6 μm) was designed to generate sufficient surface tension to hold beads in the microwells. This kept false signals resulting from physical crosstalk between the trapped beads at a negligible level.

There is another challenge unique to applying the digital assay approach for near-real-time cytokine profiling with high multiplex capacity. The assay needs to provide a truly rapid and trustful data analysis (without human supervision) originating from ~7 million microwells per chip. Additionally, the signal counting process needs to distinguish precisely between images of multi-color bead-filled and empty microwells and to identify signals accurately while subjected to a large fluorescence intensity variance, occasional image defects due to reagent mishandling, and image focus shifts. These challenges make the conventional image processing method with the

thresholding and segmentation (GTS) scheme inaccurate and require human supervision for error correction in handling digital assay images. Mu et al. (152, 153) showed that the use of machine learning algorithms would provide promising solutions to significantly improve the accuracy of digital assay image processing. However, this approach is only applied for single-color images with a small number of microreactors (a few thousand) with 1080×1120 pixels, which is impractical for high-throughput analysis. To address these challenges, we developed a novel dual-pathway parallel-computing algorithm based on convolutional neural network (CNN) visualization for image processing.

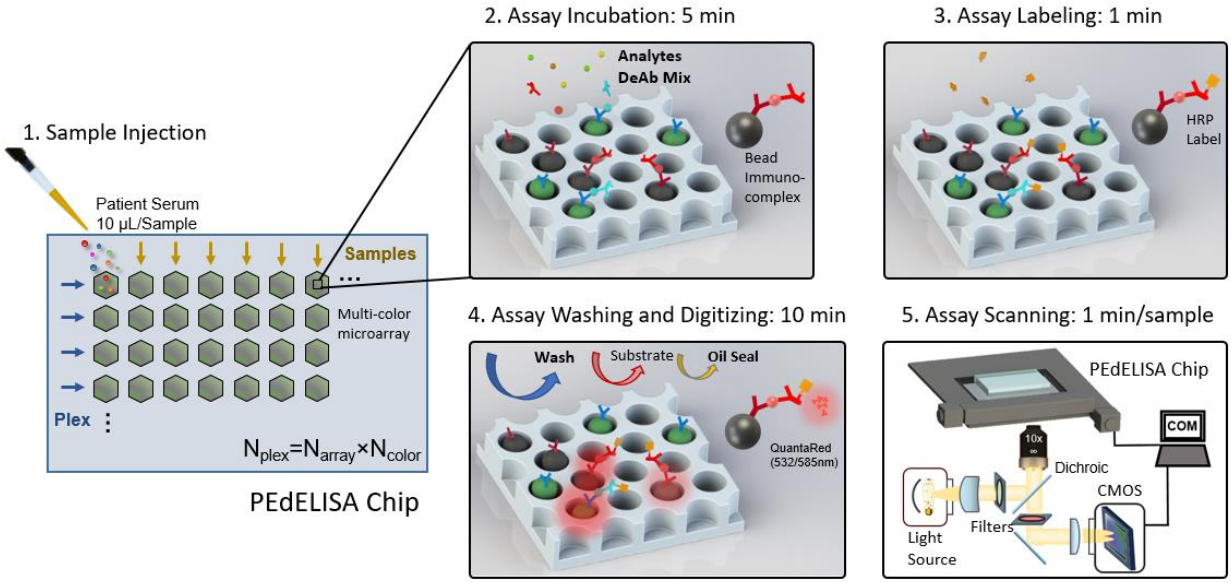

Figure 4.3 Concept of CNN processed PEdELISA microarray analysis. Microfluidic spatial-spectral encoding method used for multiplexing digital immunoassay. Fluorescence color-encoded magnetic beads coated with different capture antibodies are pre-deposited into the array of hexagonal-shaped biosensing patterns in the microfluidic detection channel. The locations of the biosensing patterns are physically separated from each other. This arrangement yields $N_{color}\times N_{array}$ measurement combinations determining the assay plexity, N_{plex}, where N_{color} is the total number of colors used for encoding beads deposited in each biosensing pattern, and N_{array} is the total number of the arrayed biosensing patterns in each detection channel. In this study, $N_{color}=2$ (non-fluorescent and Alexa Fluor® 488: AF488) and $N_{array}=8$.

The CNN-based analysis procedure (Figure 4.4) includes multi-color fluorescence image data read-in/pre-processing (image crop, noise filtering, and contrast enhancement), microwell/bead

image segmentation by pre-trained dual-pathway CNN, post-processing, and result output. The key component, dual-pathway CNN, was pre-trained to classify and segment image pixels by labels of (I) fluorescence "On" (Qred channel) microwells, (II) Alexa Fluor® 488 color-encoded beads (AF488 channel), (III) image defects, and (IV) background. The architecture of the network is separated into a downsampling process for category classification and an upsampling process for pixel segmentation. The downsampling process consists of 3 layers, including 2 convolution layers (4-6 filters, kernel of 3×3) with a rectified linear unit (ReLU), and a max-pooling layer (stride of 2) in between. The upsampling process consists of a transposed convolution layer with ReLU, a softmax layer and a pixel classification layer. To speed up the training process, we started with dividing an image with 32 × 32 pixels and classifying them with the labels and then eventually expanding the image pixel size to 256 × 256 using a pre-trained network (Figure 4.2). We found a large intensity variance across the optical signals from beads in different microwell reactors. As a result, the intensity-based labeling of microwells leads to recognition errors. Microwells with bright beads can be misrecognized to have larger areas with more pixels than those with dim beads. Instead, given that all microwells are lithographically patterned to have an identical size, we labeled them using the same pre-fixed area scale (octagon, r=3 pixel for microwell, disk, r=2 pixel for bead) regardless of their image brightness to make the machine to recognize them correctly. The majority of pixel labels are for the background (Label IV) with no assay information in typical digital assay images. We used the inverse frequency weighting method to further enhance the classification accuracy, which gives more weights to less frequently appearing classes that are identified by Labels (I), (II), and (III) (See 4.2.6 for training details).

In contrast to a previously reported study (152), we greatly reduced the number of convolution layers and filters (depth of network) for high speed processing. Our algorithm employs much fewer

labels and features required for imaging processing than those for other typical CNN applications, such as autonomous driving. The unique feature of our algorithm is the ability to run two neural networks in parallel for two detection pathways: one for assay targets (e.g. microwells, beads, and fluorescence signals) and the other for defects. This allows the imaging processing to achieve high speed while maintaining good precision. As a result, it only took ~5 seconds (CPU: Intel Core i7-8700, GPU: NVIDIA Quadro P1000) to process two-color channel data for two 6000×4000 pixel images which contain 43561 micro-reactors.

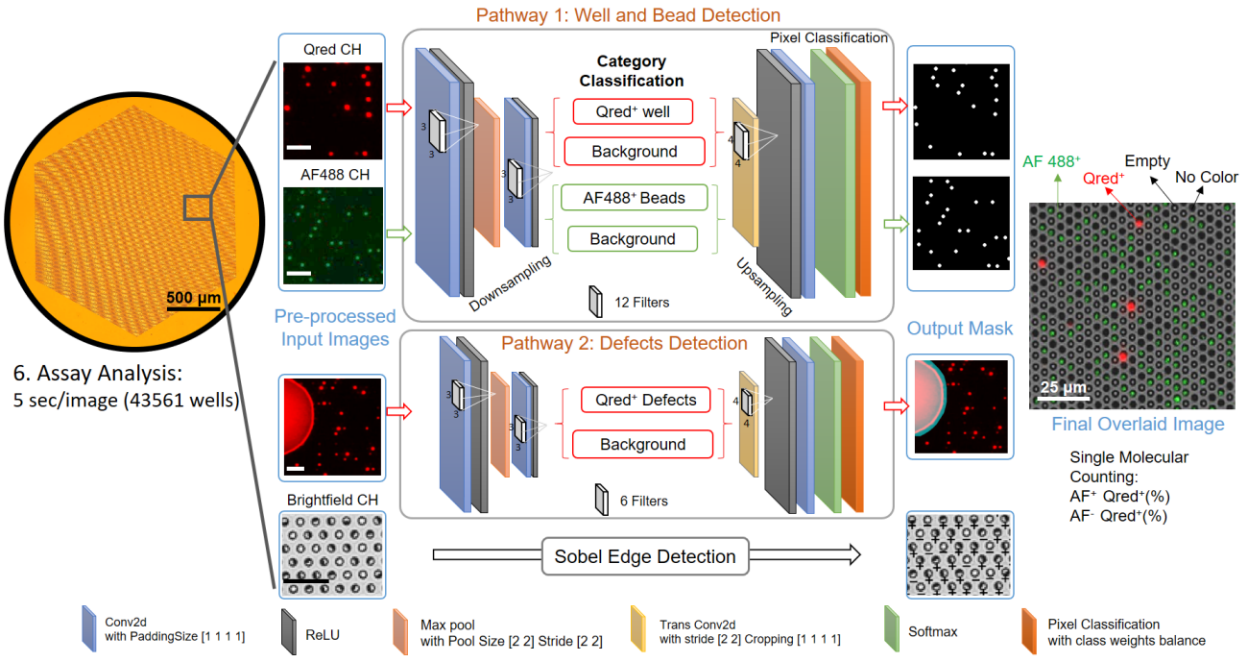

Figure 4.4 A convolutional neural network-guided image processing algorithm for high throughput and accurate single molecule counting. Two neural networks were run in parallel, reading multi-color fluorescence image data, recognizing target features versus defects, and generating an output mask for post data processing. The brightfield image was analyzed using a Sobel edge detection algorithm. The images were finally overlaid to determine the fraction of enzyme active beads emitting QuantaRed™ signal (Qred+ beads) to total beads for each color label. The unlabeled scale bars are 25 µm.

4.3.2 PEdELISA Microarray Platform Performance.

To evaluate the platform performance, we first considered false signals resulting from misplacing beads during the preparation of the PEdELISA chip. If some of the beads targeting

analyte *A* were accidentally trapped into the microwell arrays of a biosensing pattern to detect analyte *B*, these misplaced beads would yield either false positive or false negative signals of analyte *B*, thus confounding the assay ("physical crosstalk" between beads). Previous studies (154, 155) revealed that choosing an appropriate design for the PDMS microwell allowed surface tension to hold firmly a bead trapped in it even when the entire chip was flipped upside down under prolonged sonication. Guided by these studies, we designed the microwell structure to be 3.4 µm in diameter and 3.6 µm in depth to generate sufficient surface tension to hold beads in microwells (using a permanent magnet could further facilitate the seeding and retention of beads (155, 156).

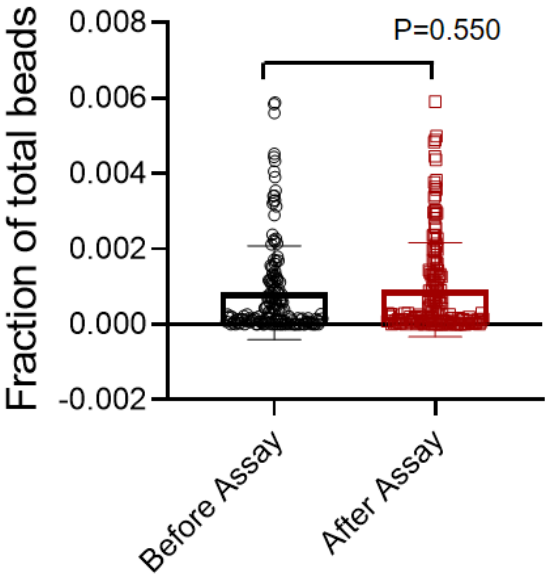

Figure 4.5 Fraction of AF-488 encoded beads invading the channel to be loaded with non-color coded beads before and after the bead flushing test assay (P=0.550). On average, only 0.087% of the trapped beads were misplaced in the channel for the both cases. The result was obtained from the fluorescence images of 160 independent microwell sites. The harsh assay conditions with a washing buffer flow rate of 40uL/min and a duration of 15 min caused negligible physical crosstalk between the beads.

To assess the impact of physical crosstalk on our assay, we ran a control test. The test started with settling AF-488 encoded magnetic beads into one of the sample loading channels of the chip (AF-488 bead channel), and then subsequently settling non-color encoded beads into another

channel next to it (non-color bead channel). Then, we washed away the untrapped beads from these channels, peeled off the bead settling layer from the multi-array biosensor layer, replaced it with sample loading layer, and applied harsh flushing first for the AF-488 bead channel and next for the non-color channel at a washing buffer flow rate of 40uL/min for 15 min. Finally, after sealing the microwells in the channels with oil, we took a fluorescence microscopy image of the chip and evaluated the number of AF-488 encoded beads invading the non-color bead channel before and after the flushing process. Across 160 independent microwell sites, we observed physical crosstalk occurring at an average bead misplacement percentage of 0.087% out of the total beads originally settled in the non-color bead channel with a 0.0012% standard deviation (Figure 4.5). Given that digital ELISA typically forms less than 0.1 antibody-antigen-antibody immune-complexes per bead on average, the false positive signal generated by physical crosstalk is nearly an order less than the typical negative control signal (0.0005-0.001 average molecule per bead) due to non-specific adsorption of proteins.

To validate the effectiveness of the dual-pathway CNN method developed in this work, we compared its performance with that of the standard method based on global thresholding and segmentation (GTS). Figure 4.6 shows the side-by-side comparison between the GTS method and the CNN method in PEdELISA image processing. Both of the methods start from a pre-processing process, which typically includes image cropping, contrast enhancement and noise filtering. The GTS method involves finding and adjusting a global threshold value based on the gray histogram of the image (Figure 4.6A, black dash line). This method labels a microwell site showing a fluorescence intensity level above the threshold value as a positive (“On”) pixel. Then, it applies a 2×2 pixel image erosion mask along the edge to remove the randomly appearing shot noise pixels with intensities above the threshold. The post-processing process of the GTS method includes

image dilation and segmentation, “On” microwell/bead counting, error correction and image overlay. Whereas, the CNN method runs two signal recognition pathways in parallel, which are pre-trained to recognize enzyme active “On” microwells (Red channel, Qred) or beads (Green channel, AF488) versus defects and contaminations using 5,750 labeled images. As a result, this method does not need to predetermine the intensity threshold value required for the GTS method.

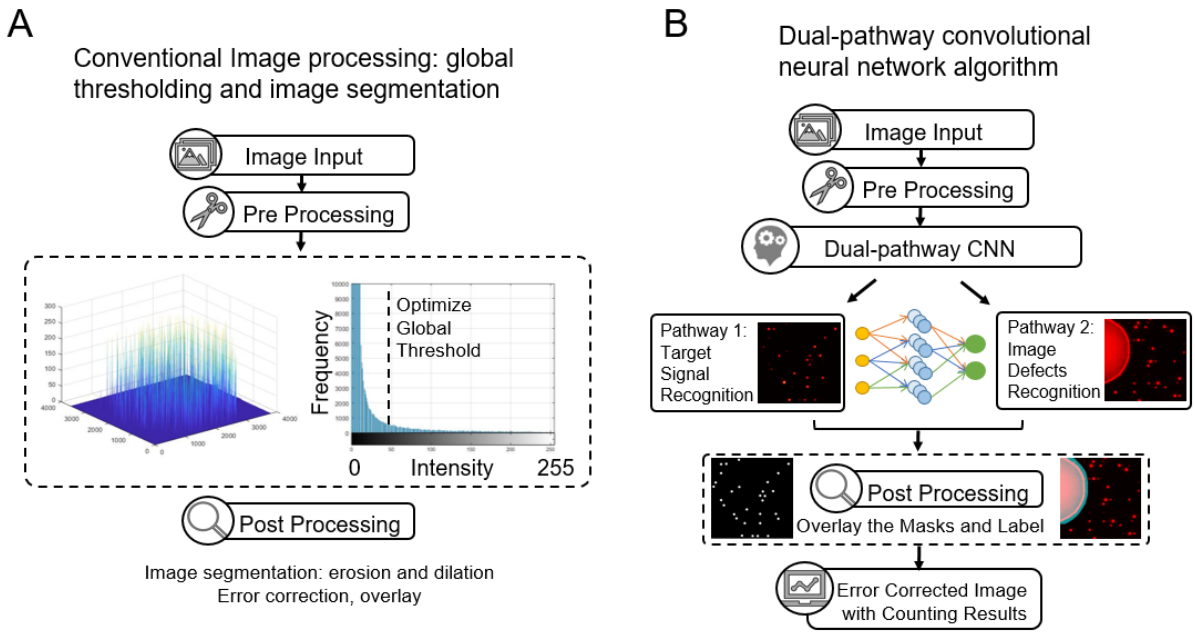

Figure 4.6 Algorithm comparison between the global thresholding segmentation (GTS) and the convolutional neural network (CNN). In GTS, an optimized global threshold value is predetermined based on the intensity histogram of the image to be processed (shown by the black dash line). The CNN method does not require the predetermination of the threshold value.

Figure 4.7A shows representative two-color-channel images causing errors to the image labeling and signal counting of the GTS method. These errors are corrected by the CNN method. For example, false signal counting derives from chip defects or poor labeling reagent confinements within individual microwell reactors due to the local failure of oil sealing. Defocusing can cause two neighboring microwells to be dilated with each other. Highly bright Qred fluorescence from an “On” microwell can cause secondary illumination to light up neighboring microwells. This

results in “optical crosstalk” between neighboring microwells (151), which causes the false counting of secondarily illuminated microwells as “On” sites. The uneven illumination of excitation light causes the failure of recognizing dim AF-488 encoded beads (recognized as non-color beads).

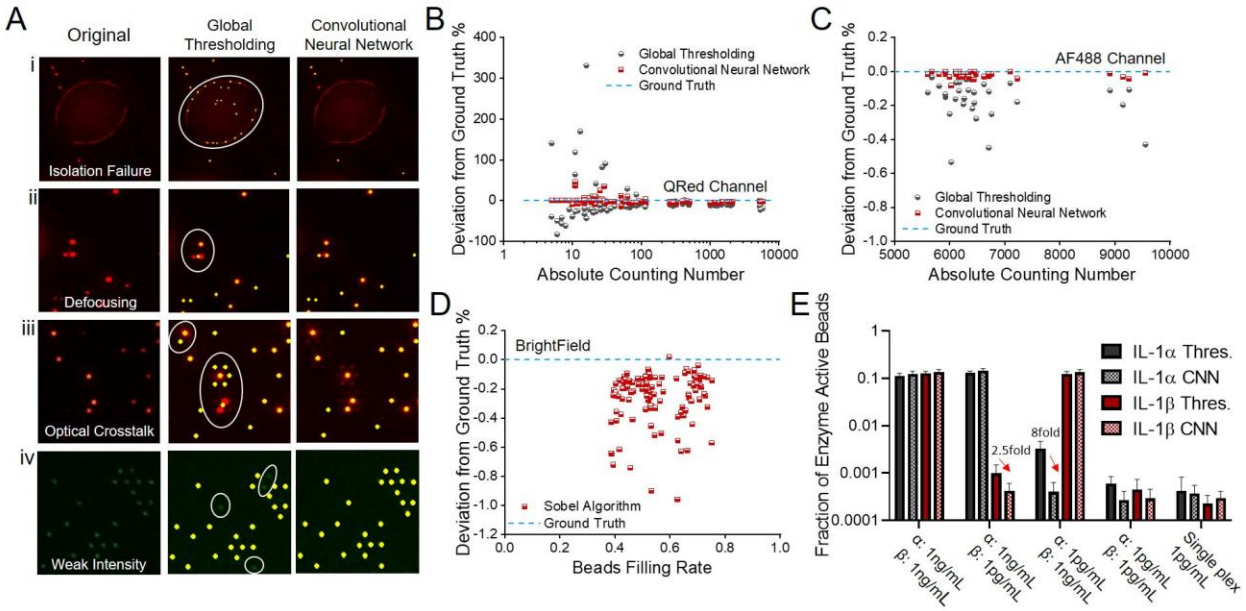

Figure 4.7 Image processing by convolutional neural network (CNN) and global thresholding and segmentation (GTS) methods (A) representative images causing false signal counting (red dot: Qred+ microwell, green dot: AF-488-colored bead, yellow dot: recognized spot to be counted). (i) The circle represents an area covered by an aqueous reagent solution that is spread over multiple microwell sites due to poor confinement during the oil sealing process. GTS counts potentially false and unreliable signal spots from the area. CNN removes the area from counting. (ii) Image defocusing causes GTS to merge two signal spots from a pair of the neighboring Qred+ microwells in the circle and to count it as a single signal spot. (iii) Secondary illumination of microwell sites due to optical crosstalk in the circle results in their false counting by GTS. (iv) GTS fails to label and count microwell sites holding dim AF-488-colored beads. Error analysis of CNN and GTS methods on (B) Qred-channel (C) AF488-channel and (D) brightfield images. (E) Tests assessing the impact of optical crosstalk on the accuracy of CNN and GTS using dual-color IL-1α and IL-1β detection by spiking (i) IL-1α:1ng/mL IL-1β:1ng/mL (ii) IL-1α:1ng/mL IL-1β:1pg/mL (iii) IL-1α:1pg/mL IL-1β:1ng/mL (iv) IL-1α:1pg/mL IL-1β:1pg/mL (v) IL-1α:1pg/mL IL-1β:1pg/mL assay in single plex for validation. All assays were performed in fetal bovine serum buffer.

In the CNN training process, we collected a large number of images for each error source and used them to train the neural network to achieve results similar to those from manual counting

with the human eyes. We applied the following equation to evaluate the error in terms of deviation to the ground truth (%):

$$Deviation(\%) = \frac{N_{CNN\ or\ GTS} - N_{TP}}{N_{TP}} \times 100\%$$

where $N_{CNN\ or\ GTS}$ is the number of microwell or bead counted either by CNN or GTS method respectively, N_{TP} is the number of true positives determined by human labeling. The human labeling process includes the pre-processing with the GTS method together with human correction to obtain the ground truth, which has been validated by the conventional sandwich ELISA method in our previous study (67).

In counting enzyme active microwells with the Qred channel, we observed that the deviation percentage from ground truth varied with the number of the counted "On" (Qred+) microwells, which is proportional to the analyte concentration. Each data point in Figure 4.7B-D was taken for a hexagonal-shaped biosensing pattern (Figure 4.4) that contains 43561 microwell arrays with an average bead filling rate of 55.1%. In these data, the number of Qred+ microwells ranged from 1 to 10000 (Figure 4.7B). At higher analyte concentrations (N_{Qred}>100), both of the methods achieved reasonably high accuracy with a deviation to the ground truth of 3.92% (CNN) and 9.96% (GTS). However, at the lower concentrations (N_{Qred}<100), this deviation became significant (CNN: 5.14% GTS: 71.6%). The larger error of the GTS scheme is attributed to the false counting of regions contaminated with fluorescent reagents and the miscounting of Qred+ microwells of low fluorescence intensity. Thus, the dual-pathway CNN greatly improved the accuracy of the image processing and eliminated the need for human supervision to correct the significant errors in the low concentration region.

In counting color-encoded magnetic beads with the AF-488 channel, we found that the deviation was very small (CNN: 0.021%, GTS: 0.161%). The deviation was suppressed by the

little spectral overlap between AF488 and Qred channels and the high image contrast that we intentionally created between AF-488 and non-color encoded beads (Figure 4.7C). Some miscounting under the uneven spatial distribution of illumination light intensity and the spherical aberration of objective lens over the entire field of view still contributed to the deviation. The CNN method achieved a nearly 8-fold improvement of accuracy. Counting the total number of beads (both no color and fluorescence color-encoded ones) with brightfield images using a customized Sobel edge detection algorithm yielded an average deviation to the ground truth of 0.256% as shown in Figure 4.7D.

To verify our ability to suppress optical crosstalk in the multiplexed assay incorporating the CNN method, we prepared a fetal bovine serum (FBS) sample spiked with two different cytokine species of 1000-fold concentration difference: IL-1α (AF488 encoded) and IL-1β (non-color encoded). Optical crosstalk becomes problematic especially in multiplexed analysis, where the quantity of one biomarker can be serval orders of magnitude higher than those of other biomarkers in the same sample. A slightly false recognition can even give a significantly higher value of biomarker concentration than its true value. Figure 4.7E shows the comparison between the conventional GTS method and the CNN method. False recognition was greatly reduced by the CNN method and we verified that 1pg/mL of IL-1α or β will not interfere even when the other protein reaches 1ng/mL. Furthermore, we performed single-plexed measurements of 1pg/mL of IL-1α and IL-1β, which give "true" concentration values while eliminating optical crosstalk. The single- and dual-plexed measurements both yielded statistically similar results with the CNN method (two-tailed unequal variance t-test, IL-1α P=0.253; IL-1β=0.368), which proves the accuracy of this method even at the presence of strong optical crosstalk.

4.3.3 Multiplex Pre-equilibrium Cytokine Detection.

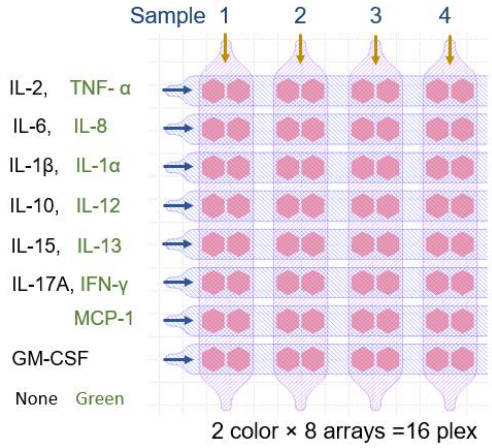

Figure 4.8 Arrangement of a panel of 14 cytokine detection for CAR-T cytokine release syndrome detection test. The two cytokines labeled with the black and green fonts on each row were detected in the sample detection channels (1, 2, 3, and 4) vertical to the row using non-color (black) and AF-488 (green) encoded beads, respectively.

Using 2-color encoded (AF488, non-color) magnetic beads with 8 physically separated microarrays, we designed a microfluidic chip to detect 14 cytokines (up to 16-plex) simultaneously (see chip design in Figure 4.8). Figure 4.9A shows standard curves obtained from PEdELISA microarray analysis with CNN image processing for cytokines ranging from 0.16 pg/mL to 2.5 ng/mL. To mimic the serum detection background, we choose to use 25% FBS as the detection buffer, which has been previously verified to match with human serum background (typical 2-4 fold dilution). Here, the measurement output is the fraction of the number of enzyme active (Qred+) beads to the total number of beads used for assaying the particular analyte. This fraction is directly correlated to the analyte concentration. The assay was performed for a system at the early state of a transient sandwich immune-complex formation reaction process with a 5-min incubation period, followed by a 1-min enzymatic labeling process. The reaction conditions have been optimized to match all cytokine biomarkers within the clinically relevant range, and a linear

dynamic range of three orders of magnitude was achieved in general. Table 4.1 summarizes the values of the limit of detection (LOD) and limit of quantification (LOQ) of the assay for each cytokine. The antibody-antigen affinity affects the LOD of the assay, and it varies across the detected cytokine species. As a result, we obtained different LOD values for these cytokines even if the capture antibody-conjugated beads were prepared by the same protocol regardless of the analyte types. The LOD value tends to decrease with an increasing incubation period. Although the assay was performed with a short incubation period of 5 min, the LOD was found to be still below 5pg/mL (with IL-1β reaching the lowest 0.188pg/mL) after optimizing the detection antibody mixing ratio and the enzyme labeling concentration.

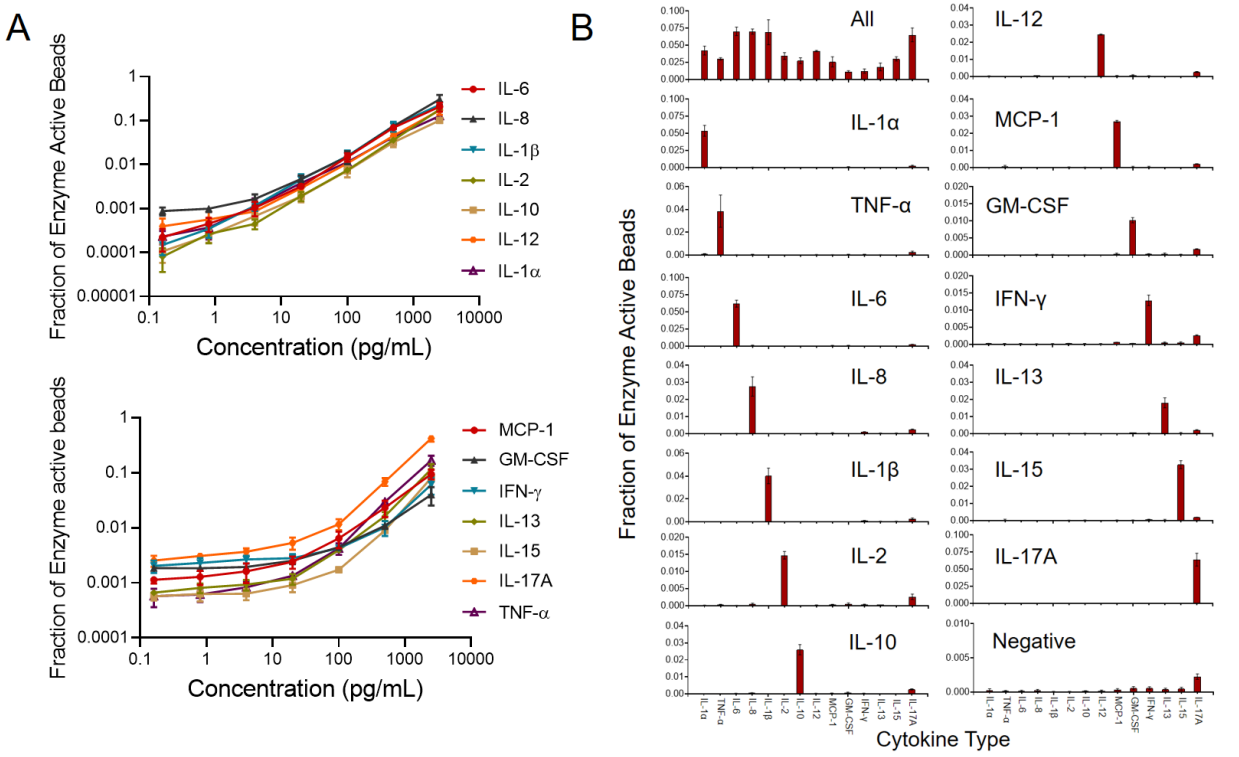

Figure 4.9 PEdELISA microarray analysis. (A) Assay standard curves for 14 cytokines from 0.16pg/mL to 2500pg/mL in fetal bovine serum (FBS). Three independent tests with two on-chip repeats were performed using recombiant proteins (error bar = standard deviation: σ). (B) Assay specificity test with FBS "all-spike-in," "single-spike-in," and "no-spike-in" (negative) samples. The analyte concentration of 500pg/mL used for spiking FBS is the optimal value to assess both false positive and negative signals. The limit of detection (LOD), limit of quantification (LOQ), and standard root mean square coefficient of variance (RMS CV) of each cytokine were cacluated from these data and summarized in Table 4.1.

Table 4.1 Limit of detection (LOD), Limit of Quantification (LOQ) and standard root mean square coefficient of variance (RMS CV) summary of 5-min 14-plex PEdELISA. Here, the LOD was determined by concentration from the reagent blank signal + 3σ and the LOQ was reagent blank's signal + 10σ. The RMS CV was determined by the root mean square average signals from 20, 100, and 500 pg/mL assay standard with typical three day-by-day repeats and 2 on-chip repeats.

Cytokine Type	TNF-α	IL-6	IL-8	IL-1β	IL-2	IL-10	IL-12
Assay Blank+3σ (%)	0.0580	0.0456	0.0920	0.0148	0.0222	0.0217	0.0493
Assay Blank+10σ (%)	0.1355	0.1168	0.1820	0.0404	0.0601	0.0584	0.1109
LOD 5-min (pg/mL)	2.195	2.667	2.033	0.188	0.535	0.210	0.613
LOQ 5-min (pg/mL)	12.80	12.21	11.54	0.696	11.24	5.661	4.996
Assay standard RMS CV (%)	16.0	6.30	14.6	5.19	15.3	9.96	14.1

Cytokine Type	IL-1α	MCP-1	IL-13	IL-15	IL-17A	IFN-γ	GM-CSF
Assay Blank+3σ (%)	0.0527	0.1557	0.0706	0.0518	0.3675	0.2283	0.2139
Assay Blank+10σ (%)	0.1240	0.3769	0.1758	0.1299	0.6641	0.3566	0.2896
LOD 5-min (pg/mL)	0.349	3.406	1.733	3.206	4.120	3.448	7.797
LOQ 5-min (pg/mL)	2.674	47.83	18.296	57.944	43.423	62.66	35.33
Assay standard RMS CV (%)	13.1	18.8	10.1	20.6	11.1	12.6	10.7

We further assessed the level of antibody cross-reactivity among 14 cytokines in FBS. Figure 4.9B shows the assay results for sera spiked by all, one, or none of the recombinant cytokines of 14 species, namely "all-spike-in," "single-spike-in," and "no-spike-in" samples. We observed more than 100 times lower background signals from the no-spike-in (negative) sample than those from the all-spike-in sample across the 14 cytokines (except IL-17A for which there is a slightly higher background due to the more active binding between its capture and detection antibodies). The signal-level variation across the 14 cytokines at the same concentration from the all-spike-in and single-spike-in samples could derive from the different levels of analyte-antibody affinity for these cytokines. We also observed a similar trend in the variation of the LOD values for the cytokines from the curves in Figure 4.9A. The signal from each of the 14 single-spike-in samples manifests a high level of specificity to the target analyte. This verifies that the multiplexed assay measurements cause negligible cross-reactivity between each cytokine analyte and other capture and detection antibodies that should not couple with it.

Finally, we applied the 14-plex PEdELISA microarray analysis for the longitudinal serum cytokine measurement from patients receiving CAR-T cell therapy. CAR-T therapies have demonstrated remarkable anti-tumor effects for treatment-refractory hematologic malignancies (157, 158). Unfortunately, up to 70% of leukemia and lymphoma patients who receive CAR-T therapy experience cytokine release syndrome (CRS). CRS is a potentially life-threatening condition of immune activation caused by the release of inflammatory cytokines (e.g., IL-6, TNF-α, and others) (121, 135). CRS initially causes fevers and other constitutional symptoms that can rapidly (i.e., within 24 hours) progress to hypotension and organ damage requiring intensive care. Previous studies (131, 132) have shown the measurement of a panel of cytokines can indicate the

early onsite of severe CRS. Thus, the way of intervening CRS could be significantly improved by the multiplex PEdELISA microarray analysis.

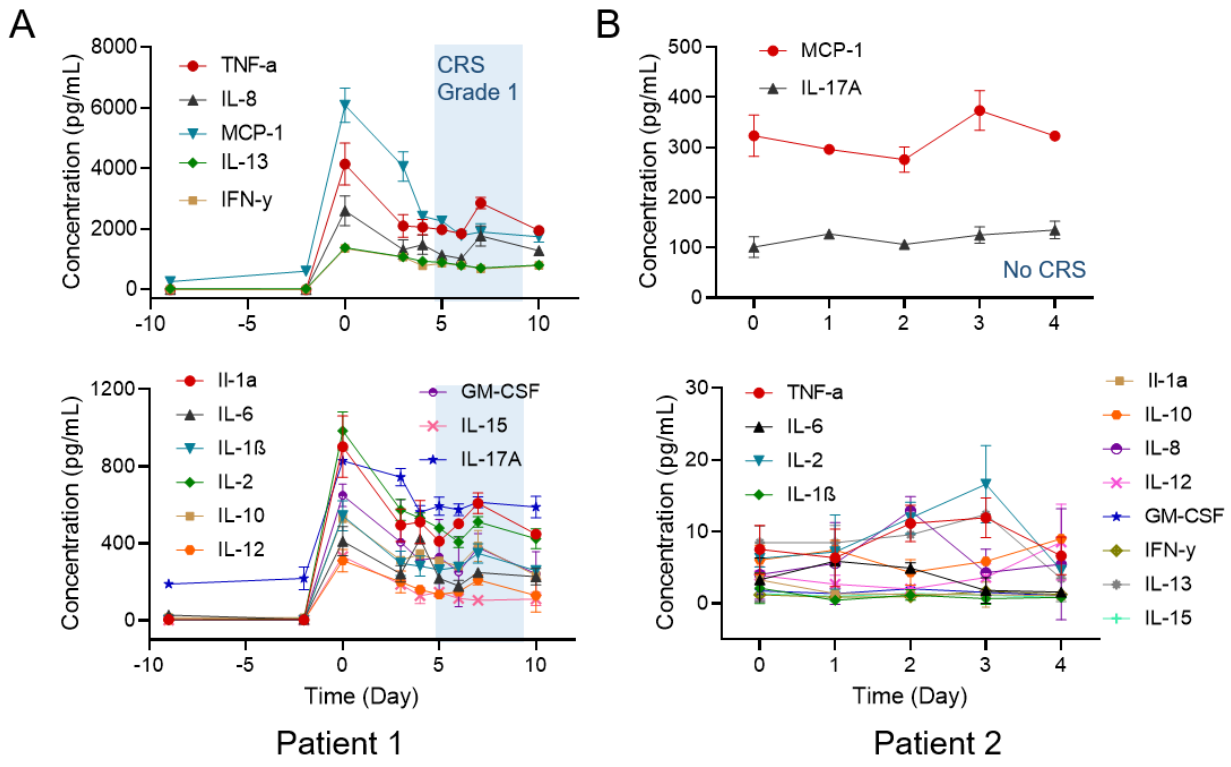

Figure 4.10 14-plex cytokine measurements in longitudinal serum samples from CAR-T patients who were diagnosed (A) grade 1-2 CRS (B) no CRS. Day 0 represents the day of CAR-T cell infusion. Data before Day 0 represents the baseline. The shaded region marks the period that the patient was diagnosed with grade 1-2 CRS. For better visualization, the data was organized and separately plotted based on the cytokine level from high to low.

To demonstrate the clinical utility of the assay technology, we ran our assay for two CAR-T patients, one who experienced up to grade 2 CRS and one who did not experience CRS in the first few days after the CAR-T infusion. The total sample-to-answer time achieved was 30 min for the entire 14-plexed measurement including the sample incubation (5 min), labeling (1 min), washing/reagent confining (10 min), and image scanning/analysis (14 min). Figure 4.10A shows that Patient 1 developed CRS on day 4 that persisted until day 9. We found significant elevations for all assayed cytokines on Day 0 in comparison to their baseline levels on Day -2 and Day -9.

Interestingly, the spike on Day 0 is not due to the CAR-T cells, as the blood sample was taken prior to CAR-T infusion. Typically, CRS patients exhibit a high IL-6 concentration within their blood (159). However, Patient 1 manifested a significantly higher level of TNF-α. This suggests biological heterogeneity in the pathogenic cytokine profiles of patients who develop CRS. We also conducted a similar analysis for a patient who did not develop CRS (Figure 4.10B). We recorded an increase in IL-2 and a relatively high level of IL-17A for this patient, while other cytokines showed no significant changes throughout the analysis. Presumably, normal CAR-T cell expansion was taking place in the patient's body.

Chapter 5

A Digital Protein Microarray for COVID-19 Cytokine Storm Monitoring

5.1 Introduction to the Study

With the global outbreak of the novel coronavirus pneumonia (COVID-19), accumulating evidence (16, 160, 161) indicates that cytokine release syndrome (CRS) is associated with severe illness. CRS is observed in several disease states associated with dysregulated immunity, including as a consequence of CAR-T cell immunotherapy(121), a manifestation of hemophagocytic lymphohistioctytosis (HLH) in malignancy, macrophage activation syndrome in autoimmune disease (162), or severe sepsis (163). Selective cytokine blockade is a mainstay of care for CRS related cancer immunotherapy (121, 136, 159), and macrophage activation syndrome (164). In COVID-19, early translational studies suggest that high serum cytokines are a result of complex interplay between lymphocytes and myeloid cells (165). Modulation of cytokine signaling pathways is currently the subject of over 50 clinical trials worldwide (166). However, most studies enroll based on clinical criteria without rapid assessment of specific cytokine levels, despite delivering therapies that are targeted to specific cytokines, such as interleukin (IL)-6. In our center, the current clinical practice is to use a variety of less specific surrogate markers, such as ferritin and CRP, to gauge a patient's overall level of inflammation. While cytokine levels are being

checked in patients with severe COVID-19, the results of these tests return in days, not hours. Ideally, treating physicians would understand the “real-time” level of a variety of cytokines in a particular patient before administering specific medications to blunt cytokine storm in critical illness, which urgently requires a low-cost near-bedside multiplex cytokine profiling assay with near-realtime assay turnaround.

Digital immunoassay (52, 56) has been considered as the next generation protein detection method which provides single-molecular sensitivity (aM-fM) detection by digitizing and amplifying enzymatic reaction in extremely confined volumes (fL-nL). Several groups invented microfluidic platforms for lab-on-a-chip operation of digital assays (78, 124, 156, 167) and notably, Yelleswarapu et al (122) demonstrated a mobile-phone-based, droplet microfluidic digital immunoassay for point-of-care (POC) settings. However, few studies have implemented a digital assay platform applicable to the clinical treatment of a COVID-19-induced cytokine storm. If continuous monitoring of the cytokine profiles of a COVID-19 patient is needed, the assay requires more than speed, sensitivity, and multiplex capacity. Other important but often overlooked requirements include (1) flexibility of running a small number of samples based on the demand of the physician with minimum preparation; (2) great inter-assay precision between multi-time point measurements, which is not an issue in conventional large batch-based retrospective tests; (3) a low-cost, compact, automated fluidic handling and readout instrumentation that can be operated inside the bio-safety cabinet with minimum user exposures to virus-contaminated blood samples.

Here, we report the development and application of an automated digital assay platform using a method termed the “pre-equilibrium digital enzyme-linked immunosorbent assay

(PEdELISA) microarray" for rapid multiplex monitoring of cytokine: IL-6, TNF-α, IL-1β and IL-10 from COVID-19 patients admitted to the ICU in the University of Michigan hospital. The PEdELISA microarray analysis employs magnetic beads trapped into spatially registered microwell patterns on a microfluidic chip. The locations of the microwell patterns on the chip indicate which target analytes are detected. Unlike the existing digital assays, our method employs an approach of quenching the assay reaction entirely on-chip at an early pre-equilibrium state. This approach achieves near-realtime assay speed (<10 min incubation) with a clinically relevant fM-nM dynamic range without losing assay linearity. Furthermore, using a simple microfluidic spatial encoding technique and machine learning-based image processing algorithm, we achieved multiplex detection with high-accuracy counting and eliminated significant bead loss faced by the commercial state of the art platform (150). The advancements of our digital assay demonstrated here enable it as a great candidate for near-bedside cytokine profiling with the combination of speed and sensitivity, both greater than those of current analog (36-38, 63) and label-free POC diagnostic systems (32, 39, 105, 168).

5.2 Materials and Methods

5.2.1 Materials.

We purchased human IL-6, TNF-α capture, and biotinylated detection antibody pairs from Invitrogen™, and IL-1β, IL-10 from BioLegend. We purchased the corresponding ELISA kits from R&D Systems (DuoSet®). We obtained Dynabeads, 2.7μm-diameter epoxy-linked superparamagnetic beads, avidin-HRP, QuantaRed™ enhanced chemifluorescent HRP substrate, bovine serum albumin (BSA), TBS StartingBlock T20 blocking buffer, and PBS SuperBlock blocking buffer from Thermo Fisher Scientific. We obtained Phosphate buffered saline (PBS) from

Gibco™, Sylgard™ 184 clear polydimethylsiloxane (PDMS) from Dow Corning, and Fluorocarbon oil (Novec™ 7500) from 3M™. The automated PEdELISA system was mainly constructed by a micro-controller (Arduino Uno and MEGA 2560), stepper motors and shields (NEMA 17, 0.9 degree, 46 N·cm, TB6600 and DM542T motor shields), linear rail guide with ballscrews (5 mm/revolution), standard anodized aluminum profiles, clear acrylic boards and other supporting wheels, connectors and parts purchased from Amazon through various vendors. The optical scanning system mainly consists of a consumer-grade CMOS camera (SONY α6100), 10x Objective lens (Nikon, CFI Plan Achro), tube lens (200 mm), optical filter sets (Chroma), halogen light source, LED light source (560 nm), optical mountings and tubings (mainly from Thorlabs and Edmund Optics).

5.2.2 Antibody Conjugation to Magnetic Beads.

We conjugated human IL-6, TNF-α, IL-1β, IL-10 capture antibodies using the epoxy-linked Dynabeads (2.7 μm) with the capture antibody molecules at a mass ratio of 6 μg (antibody): 1 mg (bead) following the protocols provided by Invitrogen™ (Catalog number: 14311D). The beads were then quenched (for unreacted epoxy groups) and blocked with TBS StartingBlock T20 blocking buffer. We stored the antibody-conjugated magnetic beads at 10 mg beads/mL in PBS (0.05% T20 + 0.1% BSA + 0.01% Sodium Azide) buffer sealed with Parafilm at 4 °C. No significant degradation of the beads was observed within the 3-month usage.

5.2.3 PEdELISA Cartridge Fabrication and Patterning.

The disposable microfluidic cartridge used for PEdELISA assay is plastic-based and fabricated by laser cutting and PDMS molding. It has a transparent sandwich structure for optical imaging as shown in Figure 5.1. The top and bottom layers are laser-cutted using 3.175 mm (1/8 inch) and 1 mm thin clear polymethyl methacrylate (PMMA) boards which contains through-holes for venting

and screw assembly purposes. The microfluidic channels (designed with AutoCAD software) are laser-cutted through a 120 μm high definition transparency polyethylene terephthalate (PET) thin film (adopted from standard screen protector) which has a silicone gel layer to create a vacuum for securely sealing to the top acrylic layer without adhesives. The power and speed of the laser cutter are optimized to ensure a high-resolution smooth cut so that resistance difference or bubbles generation can be minimized during the fluidic handling process. The femtoliter-sized microwell (d=3.4 μm) array layer (~300 μm) was made by polydimethylsiloxane (PDMS) through a standard SU-8 molding. First, we constructed SU-8 molds on oxygen plasma treated silicon wafers by standard photolithography which involved depositing negative photoresist (SU-8 2005 MicroChem) layers at 5000 rpm to form the desired thicknesses 3.8±0.1 μm. Subsequently, a precursor of PDMS was prepared at a 10:1 base-to-curing-agent ratio and deposited onto the SU-8 mold by spin coating (300 rpm) and baking overnight at 60 °C. We then transferred the fully-cured PDMS thin film onto the bottom acrylic layer using a modified surface silanization bonding method based on a previous publication (169). We also drilled 2 mm countersink holes (60°) using a benchtop mini drill press (MicroLux®) on the top venting layer for guiding the multi-pin fluidic dispensing connector. Each layer was cleaned by water bath sonication and the PET microchannel layer was carefully attached to the top venting layer for the later bead patterning process.

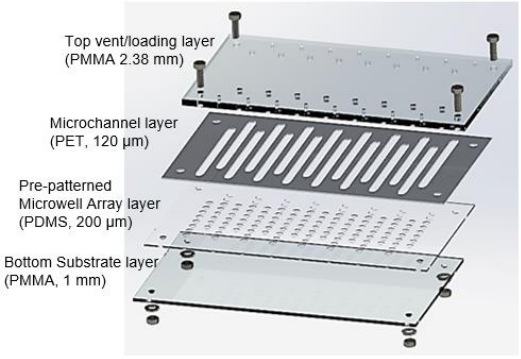

Figure 5.1 Fabrication of the disposable PEdELISA microfluidic cartridge. The cartridge contains two PMMA layers top (venting) and bottom layer (substrate), a thin PDMS layer (200 μm) which contains fL-sized microwell arrays for digital assay, and a PET thin film (120 μm) with microfluidic channels.

The PEdELISA bead patterning process involves first attaching the bead settling layer (containing long straight PDMS channels perpendicular to the PET microchannel layer) to the PDMS microwell array layer on the bottom PMMA substrate. Then, we prepared 4 sets of a 25 μL bead solution at the concentration of 1 mg/mL for IL-1β, TNF-α, IL-10, and IL-6 bead respectively. The bead solution was loaded into four different physically separate patterning channels in the bead settling layer. After waiting 5 min for beads settling inside the microwells, we washed the patterning channels with 200 uL PBS-T (0.1% Tween20) to remove the unstrapped beads. At this step, we imaged the microarray under the microscope to ensure that the microwells were filled with the beads at a sufficient rate (typically above 50%). If not, the bead mixture solution was reloaded and washed again. Finally, the bead settling layer was peeled off and replaced with PET microchannel and top venting layer. Four layers of the cartridge were sandwiched together using M2 bolt screws. Note that the bonding between the PET layer and the PDMS layer was not permanent but through pressure-based self-sealing, which can be later easily peel off and replaced. We then slowly primed each sample detection channel with Superblock buffer to passivate the cartridge surface and incubated the whole chip for at least 1 hour before the assay to avoid non-specific protein adsorption. The cartridge was typically prepared in batch and sealed in a moisture-controlled petri-dish at room temperature for up to a week with no significant degradation.

5.2.4 Design of programmed fluidic handling and low-cost optical scanning modules.

A programmed fluid handling module was designed to allow semi-automated parallel fluid handling (up to 16 samples) and to improve the fidelity and sensitivity of the assay by active on-chip mixing. The module incorporates a linear rail system (one NEMA 17 stepper motor, TB6600 motor shield, Arduino Uno, pipette holders) to operate up to four multi-channel pipettes for assay reagents loading, mixing and washing (Fig. 5.2A). A multi-pin connector was designed to provide

good sealing for the countersink holes on the cartridge. This helps avoid leaking and bubble generation during sample/reagent solution loading. A liquid crystal display (LCD) screen was attached to inform the user of step-by-step instructions with time countdown for each assay step.

An optical scanning module was designed to be cost-effective and compact for high-throughput, high-quality digital image readout. The module comprises a 2D image scanner and an optical unit. The scanner employs a two-axis linear rail system with two 0.9° NEMA 17 stepper motors, which are powered by DM542T motor shields and controlled by an Arduino MEGA 2560 board, a lead screw/rail system, and an imaging stage made of aluminum (Fig. 5.2B). The optical unit (Fig. 5.2B inset) was assembled beneath the scanning unit with a 10X Nikon objective lens mounted on a high-precision non-rotating zoom housing, a 30mm filter cube including a dichroic mirror (565 nm long-path), and an excitation (545/25 nm) and emission filter (605/70 nm). The excitation side of the filter cube was connected to an aspherical lens (F=16 mm) that collimates an LED fluorescence light source (560nm) used for fluorescent excitation of beads. The bottom of the cage cube was connected to a sliding emission filter mount for switching between the brightfield and fluorescent imaging modes. The filter mount was connected to a 200mm tube lens (Nikon) and the light path was reflected towards the side using a 50 mm right-angle prism mirror mounted in a 60mm cage cube. A CMOS sensor (SONY a6100 CMOS camera) was mounted on the side of the 60mm cage cube and remotely controlled by a laptop to perform image scanning as well as data processing. Lastly, a collimated halogen lamp for bright field imaging was mounted above the chip to provide bright field illumination. To achieve a large field and depth of view in imaging as well as increase the compactness of the module, we customized the optical distance between the tube lens and the CMOS plane so that it lowered the magnification ratio of the whole optical system to 9X. To avoid high cost and complexity for the module, we did not use Köhler

illumination for brightfield imaging. Instead, all images were post-processed with a simple flatfield correction algorithm using MATLAB. The cost of the entire optical unit is less than $4000.

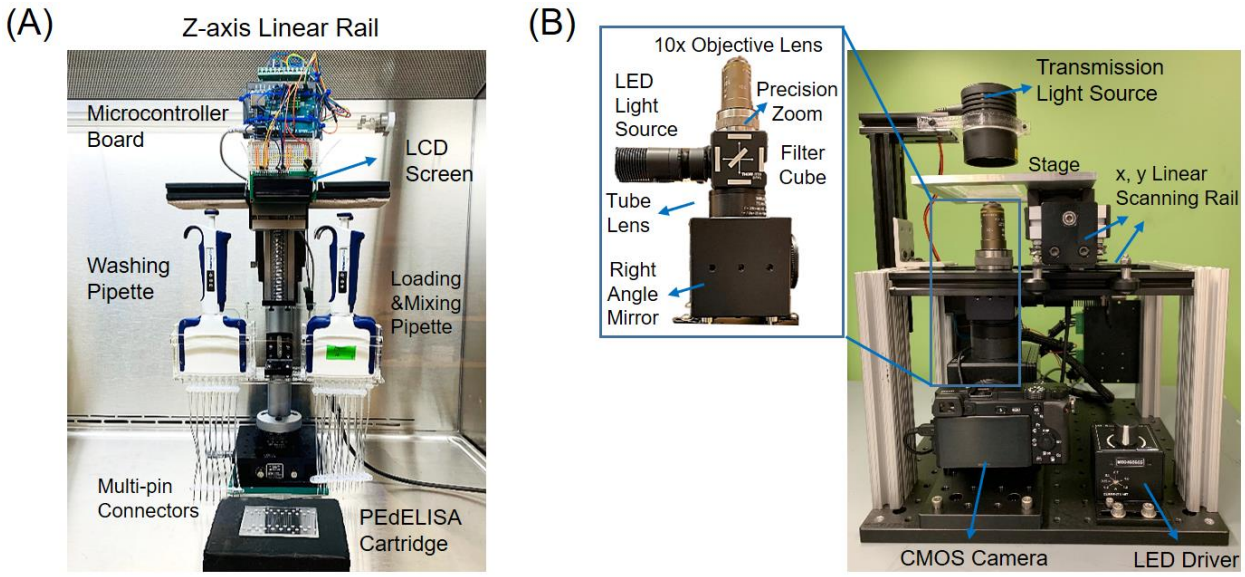

Figure 5.2 PEdELISA assay platform comprising two modules: (A) programmed fluidic handling module with Arduino controlled linear rail and multi-channel pipettes. (B) customized low-cost 2-axis fluorescence scanning module with a consumer-grade CMOS camera.

5.2.5 Control and characterization of 2D optical scanning module.

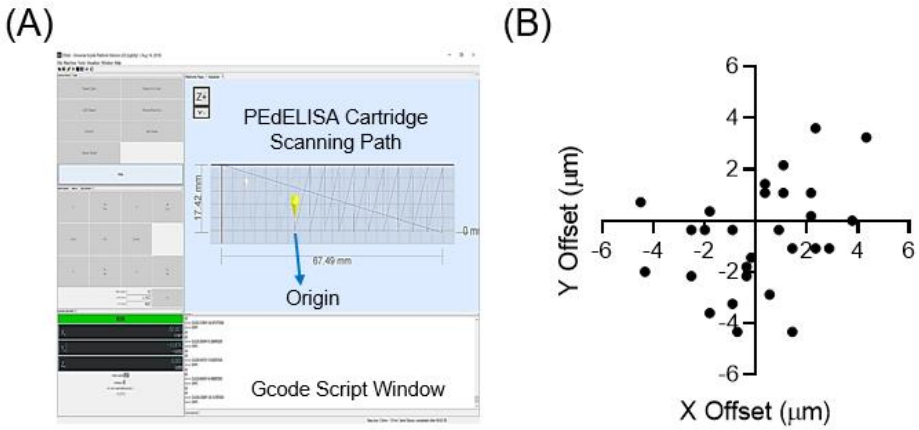

Figure 5.3 (A) User-interface of the Universal Gcode Sender for automated PEdELISA assay image scanning (B) Characterization of the bi-directional motion control accuracy by repetitively scanning and imaging the designated microarray on the cartridge. Less than 5 µm bidirectional repeatability was achieved.

To control the optical scanning module, we use the Universal Gcode Sender (UGS) that transmits a MATLAB-generated Gcode to the Arduino for imaging scanning (Fig. S3A). UGS provides a platform with manual and automated precision control of the stage and visualization of the scanning paths, making the whole module practical for this application. By designating each motor of the system through the Arduino, specific commands can be sent to each motor to move the stage to the desired location. A single command for moving a motor in Gcode includes the origin and units of movement, the shape of travel, the axis and distance of movement, and the motor speed. For the image scanning, an algorithm has been developed to account for any rotational offset in the cartridge placement to ensure that the microscope optics can capture an image of each microwell in the center of the view. We used a MATLAB script that generates a Gcode file containing line-by-line commands between two locations on the cartridge with a 5-sec delay for image focusing and capture. Our preliminary test showed that simultaneous x and y travel increases the errors of the motors. As such, we executed x and y-axis movements individually to improve the accuracy of the scanning. We characterized the x-y motion control accuracy by repeating the scanning and imaging of the on-chip microarray structures. We then used post-image overlay to calculate the x, y offsets which are plotted in Fig. S3B. We were able to achieve repeatable bi-directional scanning with a positional error of less than 5 μm and a minimum incremental movement of 0.31 μm. This provided sufficient accuracy for the PEdELISA assay.

5.2.6 Programmed PEdELISA Assay and Imaging.

The automated pipetting system was programmed to first draw 15 μL of the sample solution (patient serum and assay standard) and mix with 15 μL of detection antibody (DeAb) solution in the 96-well tube rack for 20 cycles (25-sec), and then draw 28 μL of the mixed solution and load them into the PEdELISA cartridge by two steps: Step 1. Load 14 μL of the sample-DeAb mix for

channel buffer exchange, delay 10-sec for wiping away the original buffer solution inside the channel (1x PBS solution), Step 2. Load the rest of 14 μL, followed with 50-cycles of on-chip mixing (8-min). Then the system drew in 200 μL of washing buffer (PBS-T 0.1% Tween20) and slowly loaded (micro-stepping) into the chip for washing (2-min). Next, the system drew in 40 μL of the avidin-HRP solution and slowly loaded (micro-stepping) into the chip for enzyme labeling (1-min). The chip was washed again with the PBS-T solution for one cycle (200 μL) and 1x PBS solution for another cycle (200 μL), total to reduce the interference between Tween20 and the chemifluorescent HRP substrate later (total 5-min). Finally, the system drew and loaded 30 μL of the QuantaRed substrate solution and then sealed with 35 μL of fluorinated oil (HFE-7500, 3M) for the digital counting process.

The scanning system was used to scan the image of the bead-filled microwell arrays on the PEdELISA cartridge right after the oil sealing step to detect the enzyme-substrate reaction activity. The imaging stage was pre-programmed to follow the designated path to scan the entire chip (64 microarrays) twice: 1. Scan the QuantaRed channel (545nm/605nm, excitation/emission) 2. Scan the brightfield with the transmission light source on. It typically took around 6 min to scan the entire chip for 16 samples in 4-plex detection.

5.2.7 Pragmatic study of rapid cytokine measurement in COVID-19.

This study was approved by the University of Michigan Institutional Review Board (HUM00179668) and patients or their surrogates provided informed consent for the investigational use of this test. Patients with positive SARS-CoV-2 test via PCR and respiratory failure requiring hospitalization in the intensive care unit for heated high flow oxygen or mechanical ventilation were eligible for enrollment. Subjects were approached at the request of treating teams at any point in their disease course after intensive care unit admission. Due to restrictions on patient contact

during the COVID19 pandemic, samples were drawn by the subjects' nurse with routine clinical labs in a serum separator tube and sent to the clinical specimen processing area, where they were centrifuged, aliquoted, and kept at 4°C until analysis. IL-6, TNF-α, IL-1β, and IL-10 were measured and results were posted to the patient's chart the same day. Ferritin and C-reactive protein (CRP) measurements made during routine clinical care were recorded if available from a sample within 24 hours of the cytokine measurement.

5.2.8 Statistics.

Experiments with synthetic recombinant proteins were performed daily with 2 on-chip repeats averaged to calculate the patient serum cytokine levels. 10-day standard curves using 10 microfluidic cartridges were accumulated to calculate the inter-assay coefficient of variance. The COVID-19 patient serum samples were performed in quadruplicate and averaged for the near-real-time daily cytokine profile monitoring test. Conventional ELISA test was conducted retrospectively for IL-6 in duplicate for selected banked patient samples. Here, Pearson's R-value was used to quantify the PEdELISA to ELISA correlations and the t-test was used for group analysis of the Tocilizumab treatment. A p-value of < 0.05 was considered to be statistically significant.

5.3 Results and Discussion

The PEdELISA microarray assay platform comprises a cartridge holding a disposable microfluidic chip with capture antibody (CapAb)-conjugated magnetic beads pre-settled in the designated microarray locations according to the antibody type, a parallel pipetting module controlled by Arduino for on-chip fluidic dispensing and mixing, and a 2-axis cartridge scanning and fluorescence imaging module (Figure 5.4A). In this setup, the disposable microfluidic cartridge (Figure 5.4A, inset) was designed to handle 16 samples per chip with up to 16-plex

maximum capacity. The chip contains two polymethyl methacrylate (PMMA) layers top (venting) and bottom layer (substrate) with countersink connectors that are seamlessly interfaced with fluidic dispensing tips, a thin polydimethylsiloxane (PDMS) layer (200 μm) which contains fL-sized microwell arrays for digital assay, and a polyethylene terephthalate (PET) thin (120 μm) film with microfluidic channels fabricated by laser cutting (see Figure 5.1 for cartridge fabrication). The use of the materials and processing methods significantly reduced the chip manufacturing cost (< $0.5/chip).

The PEdELISA assay was carried out by the programmed pipetting module that allowed for microfluidic loading and handling in a consistent and repeatable manner. The module first mixed patient samples or assay standards with a detection antibody (DeAb) solution and then loaded them into the cartridge in parallel, followed by 50 automated cycles of on-chip mixing during incubation (8 min), washing (2 min) and enzyme labeling (1 min), washing (5 min), substrate loading, and oil sealing (Figure 5.4B). The chip was subsequently scanned and imaged by the compact and low-cost (<$5000) fluorescence imaging module using a consumer-grade CMOS camera, and the data was analyzed by a high-throughput in-house image processing algorithm based on convolution neural network and parallel computing (Figure 5.4C). This algorithm performed autonomous classification and segmentation of image features such as microwells, beads, defects, and backgrounds, so that the digital assay counting results were generated without human supervision. The assay involved some minor manual work for assay reagent preparation and serial dilution, fluid waste collection, z-axis focusing, and origin/endpoint positioning to trigger the optical scanning.

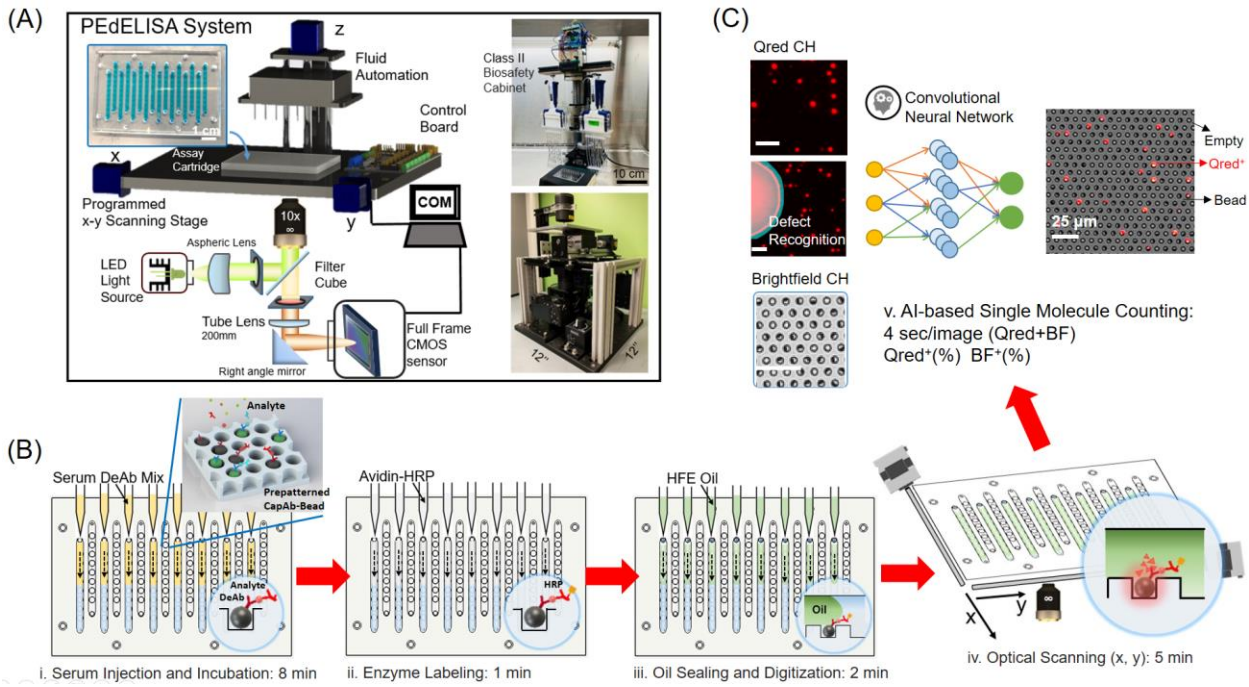

Figure 5.4 PEdELISA microarray assay platform for COVID-19 patient cytokine storm profiling. (A) Schematic and photo image of the assay system in a biosafety cabinet. The platform comprises a cartridge holding a disposable microfluidic chip (inset), an automated fluidic dispensing and mixing module, and a 2D inverted fluorescence scanning module. (B) The 4-step assay procedure includes (i) automated injection and subsequent on-chip mixing of serum and a detection antibody solution with capture antibody-coated magnetic beads pre-deposited in microwell arrays, which is accompanied by a short incubation (8-min) and followed by washing (2-min), (ii) HRP enzyme labeling (1-min), followed by washing (5-min), (iii) fluorescence substrate loading and oil sealing (2-min), and (iv) x-y optical scanning and imaging (12-min). (C) Data analysis using a convolutional neural network-guided image processing algorithm for high throughput and accurate single-molecule counting that corrects image defects and accounts for signal intensity variations. Both the fluorescence substrate channel (Qred CH) and brightfield channel (BF CH) are analyzed to calculate the average number of immune-complexes formed on each bead surface. The unlabeled scale bars are 25 µm.

We ensured the x-y optical scanning motion control accuracy each time by repetitively scanning and imaging the microarray structures on the cartridge. Post-image processing was used to calculate the x, y offset, which may be induced by the imperfection of system alignment, lead screw backlash, or motor step missing. We developed a mathematical algorithm to correct these offsets, and the scanning module was able to achieve less than 5 µm bidirectional repeatability and 0.31 µm minimum incremental movement (Figure 5.3). Using the programmed fluidic dispensing system, we optimized the assay reaction parameters (incubation time and reagent concentration) and achieved a limit of detection (LOD) less than 0.4 pg/mL with both assay reaction and labeling

incubation time in 9 min (Table 5.1). We also assessed the 4-plex assay's specificity and signal to noise ratio (SNR) by spiking-in each cytokine analyte in 100% fetal bovine serum buffer (FBS) to mimic the patient serum detection. Figure 5.5A shows the assay results of "all-spike-in," "single-spike-in," and "no-spike-in" using 200 pg/mL recombinant cytokine standards (a typical clinical threshold for cytokine storm). Negligible antibody cross-reactivity was observed between each cytokine analyte and SNR=488.0 was calculated on average (averaged assay signal over background signal).

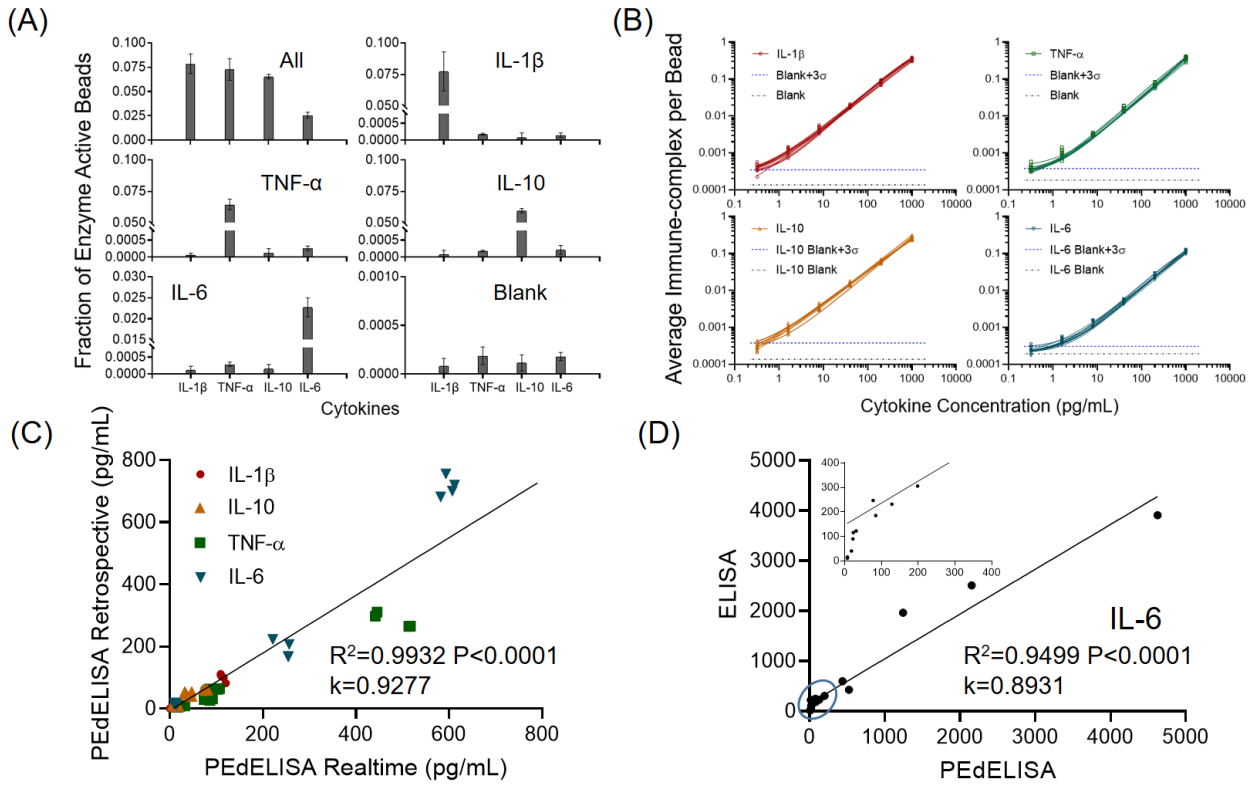

Figure 5.5 PEdELISA assay characterization. (A) Assay specificity test with "all-spike-in," "single-spike-in," and "no-spike-in" (negative) of recombinant cytokine standard at 200 pg/mL in fetal bovine serum (FBS) buffer. (B) Daily COVID-19 patient assay standard curves for four cytokines from 0.32 pg/mL to 1000 pg/mL in FBS (10 curves for each cytokine obtained over 10 workdays). The data points were fitted with four-parameter logistic (4PL) curves. The black dotted line represents the signal level from a blank solution. The blue dotted line shows 3σ above the blank signal, which is used to estimate the limit of detection (LOD) for each cytokine. (C) Linear correlation (R^2=0.99, P<0.0001) between rapid measurements of fresh samples and retrospective measurements of stored samples (1 freeze-and-thaw at -80 °C) in quadruplicate for 5 representative COVID-19 patients. (D) Good agreement (R^2=0.95, P<0.0001) observed between single-plex IL-6 ELISA and multiplex PEdELISA measurements for 16 COVID-19 patients. The inset shows the circled region.

In order to facilitate the care of patients with COVID-19 at the University of Michigan Hospital, we undertook a pragmatic study to rapidly return same-day cytokine levels to the clinical teams treating critically ill COVID-19 patients in ICU at the physicians' request from April 9th to May 29th in 2020 (170). Given the investigational nature of the assay, patients or their representatives provided informed consent for cytokine measurements to be provided for clinical use (UM IRB HUM00179668). COVID-19 Patients with respiratory failure that requires hospitalization in the ICU for mechanical ventilation were eligible for enrollment (see 5.2.7 for details). To ensure the accuracy of our data, the COVID-19 patient samples were run in quadruplicates with a calibrated assay standard curve every day. Figure 5.5B shows assay standard curves that were accumulated in 10 different workdays of the patient cytokine monitoring period. The multiple assay standard curves yielded excellent repeatability with the inter-assay coefficient of variation (CV) of ~ 10% due to the programmed fluidic handling and reaction (Table 5.1). We also characterized the intra-assay CV for five representative COVID-19 patient serum samples with cytokines at concentrations ranging from 6-600 pg/mL, each tested in quadruplicate measurements. We compared assay data for these five patients resulting from near-real-time measurements of fresh samples drawn daily and retrospective measurements of stored samples after one freeze-thaw cycle. We observed a good linear correlation (R^2=0.99) between the two measurement modes except for TNF-α. This suggests that TNF-α in the stored serum could degrade by 20-40% after the freeze-and-thaw banking at -80 °C (Figure 5.5C). Additionally, to validate our PEdELISA microarray assay, we compared the assay results with those of a conventional single-plex ELISA method that retrospectively measured 15 banked samples from identical patients. Because conventional ELISA requires a much larger sample volume (>200 μL for each measurement, in duplicate per analyte) relative to PEdELISA, it was practically difficult

for us to manage the acquisition of a sufficiently large blood sample volume from critically ill COVID-19 patients. Therefore, we only validated our assay against IL-6 detection results (Figure 5.5D). The data between these two methods overall matched linearly (R^2=0.95, P<0.0001). The slight discrepancy was observed at concentrations below 50 pg/mL and may potentially due to the limited sensitivity and linearity of the ELISA assay (Figure 5.5D inset).

Table 5.1 Limit of detection (LOD), limit of Quantification (LOQ), and coefficient of variation (CV) of PEdELISA for a panel of 4 cytokines. Here, the LOD and LOQ values were determined from the blank signal + 3σ and the blank signal + 10σ, respectively. The intra-assay CV was determined by quadruplicate measurements of five COVID-19 patient samples at the range of 6-600 pg/mL in both near-real-time and retrospective assay modes. The inter-assay CV was determined by taking the root-mean-square average of signals from 40, 200, and 1000 pg/mL assay standard in 10-day continuous measurements of COVID-19 patients.

Cytokine Type	Assay Blank (Average molecule per bead)	Assay Blank+3σ (Average molecule per bead)	LOD (pg/mL)	LOQ (pg/mL)	Intra-Assay CV (%)	Inter-Assay CV (%)
IL-1β	0.000143	0.000347	0.191	1.188	4.68	9.98
TNF-α	0.000179	0.000379	0.198	1.889	8.77	11.66
IL-10	0.000136	0.000378	0.350	1.552	5.70	9.63
IL-6	0.000189	0.000309	0.377	2.378	4.55	10.80

Figure 5.6A shows a typical timeline of our daily cytokine profile measurement completed within 4 hours after the blood draws in the ICU. The assay itself could be performed with a sample-to-answer time as short as 30 min for typical non-COVID-19 serum samples. However, in the practical operation of our test, a larger amount of time was spent on sample processing, transport, and team coordination, as well as biosafety and disinfection protocols in handling COVID-19 samples. Nevertheless, the <4-hour blood

draw to result turnaround is still rapid as compared to typical clinically deployed tests. This rapid result of the PEdELISA allows clinically meaningful time-course measurements in critically ill COVID-19 patients with respiratory failure during their ICU-span. Here, patients undergoing treatment with an expanded/emergency use of an immunomodulating selective cytophoretic device (SCD) were screened (first data point) and monitored with PEdELISA to provide <4-hour feedback on progress of therapy. Here, the SCD therapy was applied to temper the cytokine storm by continuously processing circulating neutrophils and monocytes to a less proinflammatory phenotype using an extracorporeal membrane cartridge integrated into a renal replacement blood circuit (171). Treatment details and outcomes are described in (172), and here we present serial measurements from two additional patients for two-week continuous monitoring. Both patients experienced severe cytokine storm and acute respiratory distress syndrome (ARDS) on the screening time point, and demonstrated decreases in IL-6 and IL-6/IL-10 ratio and clinically improved treatment outcome over the course of therapy (Figure 5.6B, C). With the successful implementation of this therapy monitored by PEdELISA, both of the patients were able to come off of extracorporeal membrane oxygenation (ECMO) and mechanical ventilator support and were eventually discharged alive from the hospital.

Our rapid cytokine measurement also revealed significant subject-to-subject heterogeneity despite all patients being critically ill. As expected, interruption of IL-6/IL-6R signaling in patients who received tocilizumab resulted in marked elevation of IL-6 levels in the setting of ongoing illness ($p<0.0001$, Figure 5.6D) (173). Among patients who did not receive tocilizumab, we observed a large degree of variability in IL-6 levels, with a quarter of subjects having IL-6 <15 pg/mL, median value of 106 pg/m, and coefficient of

variation (CV) of 114%. Variability of TNFα (CV 164%) and IL1β (CV 193%) was driven by a small number of subjects with elevated levels. However, like IL6, levels of IL10 were also broadly distributed in patients who had not received tocilizumab (CV 93%).

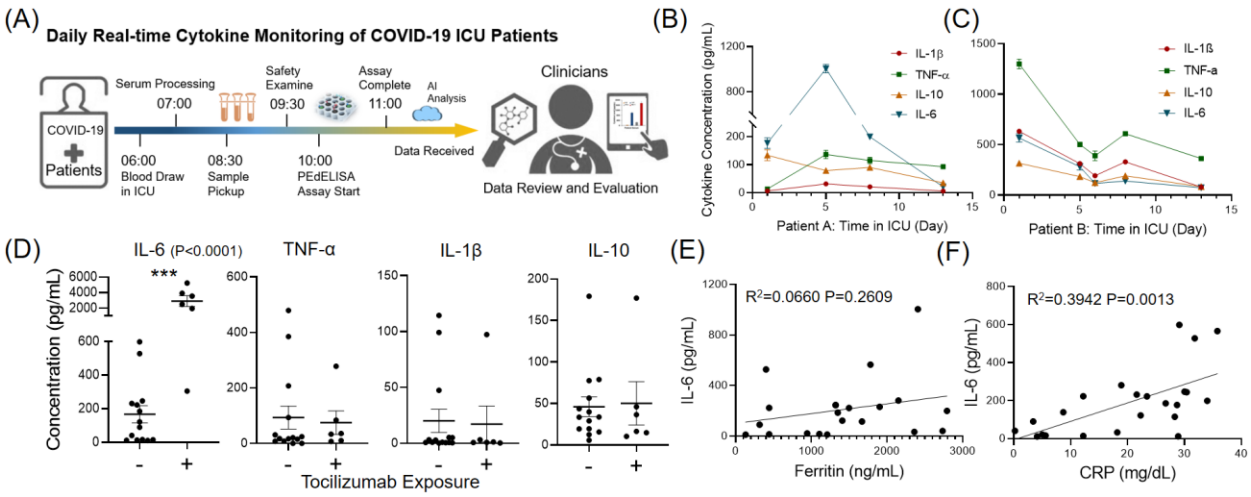

Figure 5.6 (A) Timeline of daily near-real-time COVID-19 cytokine measurement. (B)-(C) Two-week serial monitoring of two critically ill COVID-19 patients with respiratory failure in ICU. Both patients experienced severe cytokine storm and were under emergency use of a selective cytophoretic device (SCD) by cytokine pre-screening (first data point). The patients demonstrated decreases in IL-6 and IL-6/IL-10 ratio and clinically improved treatment outcome over the course of therapy. (D) Statistical group analysis of patients that were dosed/undosed with Tocilizumab. Significant elevations of IL-6 levels were observed after the treatment of Tocilizumab (P<0.0001). (E)-(F) Correlation of cytokine IL-6 to Ferritin and C-Reactive Protein (CRP), standard clinical inflammatory biomarkers. Ferritin does not correlate well with IL-6 (R2 = 0.066, P=0.261). CRP correlates with IL-6 (R2 =0.394, P=0.0013) better, but the IL-6 levels were widely distributed for patients with high levels of CRP.

Given the heterogeneity of cytokine levels in critically ill patients with COVID-19, we asked whether IL-6 levels were reflected in surrogate biomarkers. In current, rapidly evolving clinical practice, the presence of cytokine storm and risk of clinical deterioration is frequently judged by inflammatory markers such as CRP and ferritin in the absence of direct cytokine measurement. Ferritin did not predict IL-6 levels (Figure 5.6E, R^2 = 0.01, P=0.71). CRP was significantly associated with IL-6 (Figure 5.6F, R^2 =0.41, P=0.018). However, this association was driven by low IL-6 in subjects with low levels of CRP, while IL-6 values in subjects with high CRP were widely distributed. Neither CRP nor ferritin is a reliable predictor of IL-6. Note that our pragmatic

study of rapid cytokine measurements in patients with COVID-19 was designed to provide information to clinicians, rather than systematically study the biology of COVID-19. We therefore enrolled subjects without regard to time from the onset of infection. Furthermore, due to these subjects' critical illness, many received empiric antibiotic therapy, limiting our ability to determine bacterial co-infection. These factors, as well as our small sample size, may have contributed to the heterogeneity of the cytokine response. Nevertheless, all subjects in this study were critically ill and had respiratory failure, underscoring the diversity of biological mechanisms that may lead to critical illness in COVID-19 and the importance of measuring, rather than inferring, cytokine storm.

Chapter 6

AC Electroosmosis-enhanced Nano-plasmofluidic Detection of Ultra-low-Concentration Cytokine

6.1 Introduction to the Study

The ability to detect the dynamic surface binding of biomolecules without using labeling agents provides a critical basis for emerging biochemical analysis. Plasmonic biosensors based on biologically functionalized noble metal nanoparticles enable rapid, label-free detection of proteins, DNA, and mRNA with ease of signal acquisition and robustness in complex biological solutions (174-177). These biosensors transduce biomolecular surface binding events into optical signals that reflect changes in the resonant behavior of conduction band electrons near the surface of optically excited metallic nanoparticles. Among them, gold nanorod-based plasmonic biosensors have been demonstrated to achieve single-molecular sensitivity (178-180) and its microarray enables practical protein detection at high-throughput and multiplexity (31, 181, 182). Despite their practicality and the intrinsic sensitivity of the individual nanoparticles, these biosensors exhibit performances limited by poor diffusion of the target molecules, exemplified by the presence of a large depletion zone near the sensor surface, especially for high-density microarrays. The diffusion-limited molecular binding kinetics and the resulting poor LOD prohibit the wide use of the nanoplasmonic biosensors in clinical diagnostics and biochemical assays.

A miniaturized microfluidic design with effective sample mixing techniques (183-186) plays a key role in the detection of a wide variety of chemical/biological species. In particular, AC electrokinetics, including dielectrophoresis (DEP), ACEO, and electrothermal effects, have been widely used to preconcentrate biomolecules and enhance the analyte capture efficiency in microscale heterogeneous assays (187-190). For example, Gong (191) et al. monolithically integrated silicon nanowire field-effect transistor (FET) biosensors with micro-fabricated electrodes and achieved 10^4 times sensitivity improvement for detection of prostate specific antigen (PSA) in PBS buffer. Cheng (192) et al. integrated ACEO and positive DEP with an electrochemical impedance spectroscopy (EIS) biosensor in the detection of IgG-protein A. More recently, DEP was utilized to enhance surface plasmon resonance (SPR) sensing with gold nanohole arrays (42), and ACEO was coupled with surface-enhanced Raman spectroscopy (SERS) (40), in both studies, unprecedented levels of detection limit and assay speed were demonstrated. Among these sensing enhancement mechanisms, ACEO coupled with label-free optical biosensing logically offers a promising approach because it can generate strong three-dimensional (3D) vortices for microfluidic mixing at relatively low voltage (188), does not require any invasive, agitating mechanical components interfering with far-field plasmonic detection optics, and can be readily tuned by voltage and frequency using microfabricated electrodes of simple design which is integrated in a microfluidic system. The ACEO approach can improve mass transfer-enhanced analyte-receptor interactions, thus enhancing biosensing performance.

In this study, we report synergistic integration of plasmonics and microfluidics to develop a label-free plasmonic gold nanorod (AuNR) optofluidic device coupled with ACEO analyte flow to overcome the barrier for diffusion-limited nanoparticle biosensing performance. The plasmofluidic integration has recently attracted much attention as an emerging approach to

advancing plasmonic device technology (193). Our device consists of a glass substrate coated with gold nanorods between two coplanar rectangular Pt microelectrodes and another polydimethylsiloxane (PDMS) microfluidic channel layer (Figure 6.1A). The ACE-LSPR biofunctional nanoparticle imaging process starts by applying an 180° out-of-phase AC voltage across the microelectrodes of the device. The movement of ion charges in the electrical double layer induced on the electrode surfaces (Figure 6.1A) generates a rotational fluid motion. This fluid motion causes microfluidic agitation, facilitating the transport of analytes down to the sensing surface of AuNR to break the depletion zone (depicted by the blue arrows in Figure 6.1B, C). The sensor response is therefore enhanced by the increased molecular collision events. The binding of target analytes onto the antibody-conjugated AuNRs causes a spectral shift of the scattering light from the AuNR surfaces, which translates into a far-field intensity increase of the optical signal detected by optics using a bandpass filter (Figure 6.1D). Patterned AuNR arrays on the device were imaged by darkfield microscopy coupled with an Electron Multiplying Charge Coupled Device (EMCCD) with high sensitivity. As shown by the darkfield image (Figure 6.1E), the glass substrate contains a 25 μm-wide patterned area of AuNRs between 50 μm-wide microelectrodes and two additional reference AuNR sensor patterns of the same shape placed sufficiently (200 μm) away from the microelectrodes. Three sets of such patterns were constructed on the same chip for triplicate measurements. The PDMS layer was attached to the glass substrate with the sample detection channels (400 μm in width and 80 μm in height) running orthogonal to the line-shaped AuNR sensor patterns and the microelectrodes (depicted by the dotted line in orange). A scanning electron microscope (SEM) image (Figure 6.1F) shows the distribution of nanorods and the formation of a thin dielectric layer (from the binding of antibody/antigen) after assay.

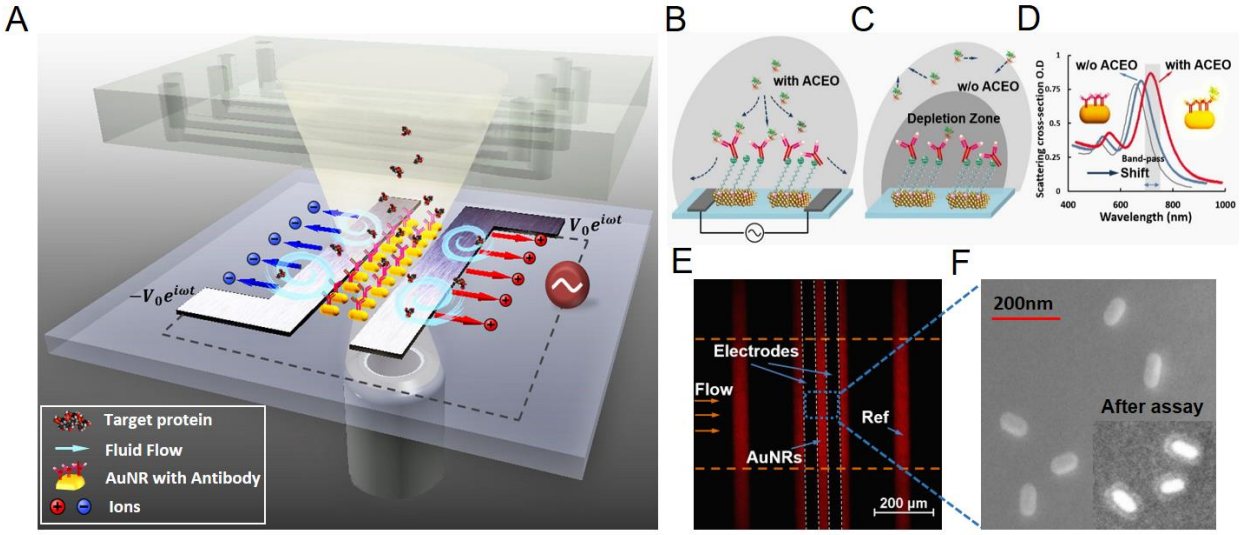

Figure 6.1 (A) Schematic and principle of AC electroosmosis-enhanced localized surface plasmon resonance (ACE-LSPR) biofunctional nanoparticle imaging. Pt microelectrodes were first patterned on a glass substrate by photolithography and metal lift-off. AuNRs were then deposited to form line-shaped sensor pattern between the microelectrodes using a microfluidic patterning technique. With 180° out-of-phase AC bias applied to the Pt electrodes, the electrical double layer horizontally moves along the electrode surfaces. The electrical double layer movement generates a hydrodynamic rotational flow within the microfluidic channel. The hydrodynamic flow facilitates the transport of the target biomolecules down to the sensing surface and their surface binding reaction. (B)-(C) Close views of the analyte-receptor interactions with/without ACEO. A large depletion zone is formed and slows down the surface reaction under diffusion-limited operation. (D) The binding results in an increase of scattering cross-section and a red shift of the plasmon resonance which is converted into the scattering intensity increase by a band-pass filter (680/13 nm, shown by the shade). (E) Darkfield image of AuNR line-shaped patterns (shown in red) and microelectrodes (black strips in the middle) with a microfluidic flow channel perpendicular to them (400 μm, orange dotted line). (F) SEM image showing the zoomed-in view of the isolated AuNRs patterned on the glass substrate between the microelectrodes. The size of the AuNRs was measured to be ~40 nm in diameter and ~84 nm in length. After the assay, the formation of a dense dielectric layer surrounding each AuNR was observed, suggesting the binding of antibodies and analytes onto the sensor surface (Inset).

6.2 Materials and Methods

6.2.1 Materials.

The AuNRs were purchased from NanoSeedz^{TM}, Hong Kong (product # NR-40-650). Each AuNR is 40 nm in diameter and 84nm in length. The particle shape and size were chosen to yield high sensitivity and sufficient binding sites (31, 194). The AuNRs were synthesized by a seed-

mediated method and were stabilized by cetyltrimethylammonium bromide (CTAB). The measured ensemble-average scattering longitudinal plasmon resonance of these particles in water is at λ = 655 nm. Human IL-1β capture and antibody was purchased from BioLegend. Human IL-1β uncoated ELISA kit was purchased from Invitrogen. EDC (1-ethyl-3-(3-dimethylaminopropyl) carbodiimide hydrochloride), Sulfo-NHS (Sulfo-N-hydroxysulfosuccinimide), MES (2-(N-morpholino)ethanesulfonic acid) buffered saline, and PBS SuperBlock blocking buffer were obtained from Thermo Fisher Scientific. 16-Mercaptohexadecanoic acid (MHA) was purchased from Sigma-Aldrich. Charcoal stripped human serum matrix was obtained from EMD Millipore.

6.2.2 Device Layout and Fabrication.

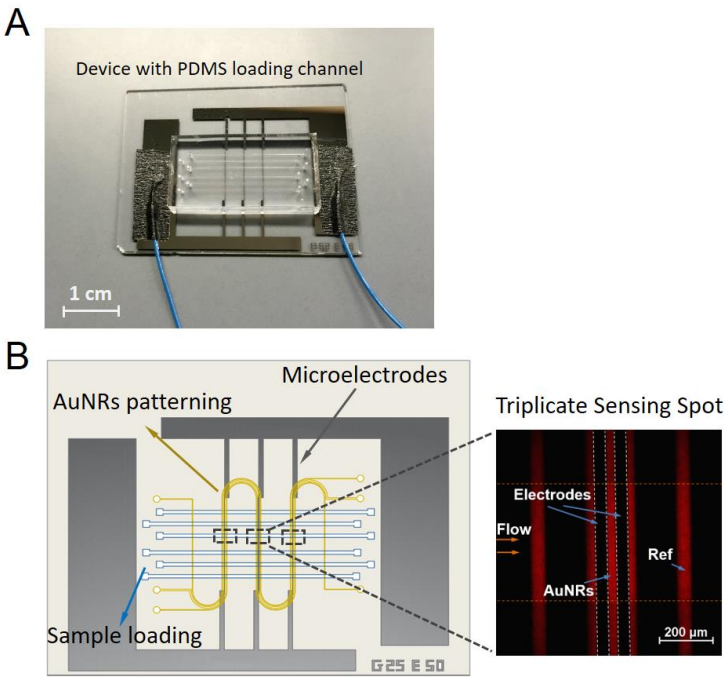

Figure 6.2 ACE-LSPR optofluidic device layout. (a) Photo image of the ACE-LSPR optofluidic device chip. The scale bar is 1 cm. (b) Device layout showing the design incorporating three parallel meandering AuNR patterns (yellow) and six parallel sample loading/detection channels made of PDMS (blue). Inset: x10 darkfield image of the sensing spot formed at the intersection between the AuNR lines and the PDMS channels. Ref: ACEO-Decoupled LSPR Biosensor.

Figure 6.2 shows the detailed device layout, which consists of coplanar rectangular Pt microelectrodes, three parallel meandering lines of gold nanorods (AuNRs) (depicted in yellow),

and six parallel sample loading/detection channels of PDMS (depicted in blue) on the same glass substrate. Each intersection between the AuNR lines and the horizontal sample loading/detection channels yields a sensing spot, which has an ACEO-coupled LSPR biosensor region between the microelectrodes and two ACEO-decoupled LSPR biosensor regions 200 μm away from the microelectrodes. The ACEO-decoupled LSPR biosensor regions are used as references in control experiment (depict as Ref in Figure 6.2B inset). Three identical sets of the sensing spot were constructed within each sample loading/detection channel on the same chip for triplicate measurements.

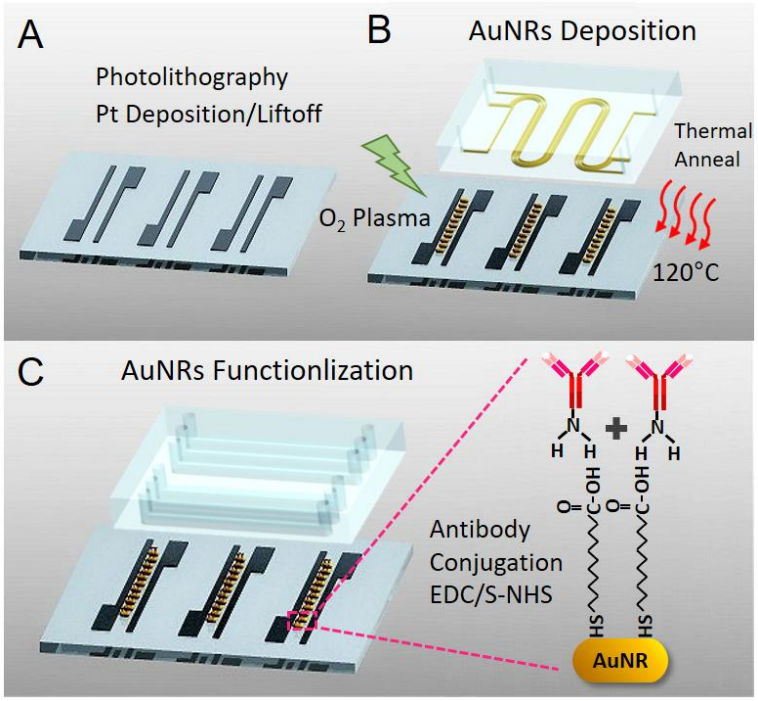

Figure 6.3 Schematic of the device fabrication process which includes: (A) Pt/Cr microelectrode patterning by sputtering and liftoff processes; (B) AuNRs deposition by O_2 plasma treatment, microfluidic patterning, and thermal annealing; (C) Bioconjugation of AuNR sensor sites with anti-IL-1β with EDC/sulfo-NHS linking using 16-Mercaptohexadecanoic acid.

Figure 6.3 shows the schematic of the ACE-LSPR device fabrication process. It started with deposition of parallel coplanar Cr/Pt (60nm) plate microelectrodes (50um wide, 25 um gap) on

glass substrates (Figure 6.3A). A glass substrate was first treated with Piranha solution ((H_2SO_4:H_2O_2 = 3:1 v/v), rinsed thoroughly with DI water, and air dried before use. A layer of positive photoresist (SPR 220 3.0) was spin-coated on the glass substrate and photolithographically patterned using a darkfield photomask. An E-beam evaporation method (EnerJet Evaporator) was used to deposit a 10 nm-thick layer of chromium as the adhesion layer and then a 50 nm-thick layer of platinum on top of it. The Cr/Pt layer was subsequently lifted off using acetone and ultrasonication, which formed the microelectrode patterns. The Cr/Pt microelectrode-patterned glass substrate was then thoroughly rinsed with D.I. water and dried with N_2.

The next step involved deposition and patterning of gold nanorods (AuNRs) to form the three parallel sensor lines on the glass substrate using a microfluidic patterning technique (Figure 6.3B). The substrate was again Piranha cleaned (10 min) and then treated with O_2 plasma. The O_2 plasma treatment generates a negatively charged surface as a result of the dissociation of hydroxyl groups, which enables the glass substrate to attract the positively charged, CTAB stabilized AuNRs suspended in a colloidal solution onto its surface. Immediately after plasma treating, a soft-lithographically molded PDMS microfluidic channel layer was placed on the substrate with the straight-line segments of its meandering-shaped channels aligned to the microelectrodes under a long working-distance stereomicroscope. The AuNR containing colloidal solution with a carefully determined particle concentration was loaded into the microfluidic channels from their inlets in both directions. A uniform monolayer of AnNR with an average inter-particle distance > 200 nm was settled on the substrate (Figure 6.1F), which was followed by a thermal annealing step (195) (120℃, 1h) to increase the binding strength between the AuNRs and the substrate. The straight-line segments of the meandering channels formed the AuNR sensor lines.

The third step was biofunctionalization of the AuNR patters with antibodies (Figure 6.3C). After removing the aforementioned PDMS layer, the ACE-LSPR biosensor glass substrate was rinsed with pure ethanol. An O_2 plasma descum process was used to clean the substrate surface and to remove the excess CTAB. The substrate was then immersed in 0.5mM of 16-Mercaptohexadecanoic acid (MHA) dissolved in ethanol overnight to form a uniformly coated self-assemble monolayer (SAM). Finally, the substrate was rinsed with ethanol and DI water, and the chip was covered with another soft-lithographically molded PDMS layer with straight sample loading/detection channels (400 μm in width and 80 μm in height). These channels were aligned orthogonal to the directions of the microelectrodes and the AuNR sensor lines. A solution of 0.4M EDC and 0.1M sulfo-NHS was loaded into the microchannel and incubated for 40min to activate the carboxylic acid groups of MHA. Rinsed with DI water, the chip was incubated for 1.5 hr by loading 50 μg/ml anti-IL1β solution and then passivated by SuperBlock™ (PBS) Blocking Buffer for 30 min, and finally became ready for the real-time LSPR biofunctional nanoparticle imaging study.

6.2.3 Experimental Setup and ACE-LSPR Imaging Technique.

Figure 6.4 shows the dark-field microscopy setup used for ACE-LSPR biofunctional nanoparticle imaging and signal detection. The molecular binding on the AuNR surface induces a red-shift of scattering spectrum due to the change of local refractive index as well as an increase of the particle scattering cross-section. The electron multiplying charge coupled device (EMCCD) was implemented to quantify the signal intensity enhancement here by coupling with a proper band-pass filter (680nm/13nm). We also used a fiber spectrometer to check the extinction spectrum of the entire AuNR substrate and roughly monitored the spectral shift at each bio-conjugation step. The ACE-LSPR biofunctional nanoparticle imaging process involved mounting the ACE-LSPR

device chip on a motorized X-Y stage (ProScanIII, Prior Scientific, Rockland, MA), loading a sample of 5 μL into each microfluidic channel by a syringe pump, and then performing time-lapse recording and automated image scanning across the entire sensing spots within the same channel. The optical intensity signal was averaged over the sensor surfaces, each holding a large number of AuNR biosensor nanoparticles, using a customized MATLAB code developed in our lab.

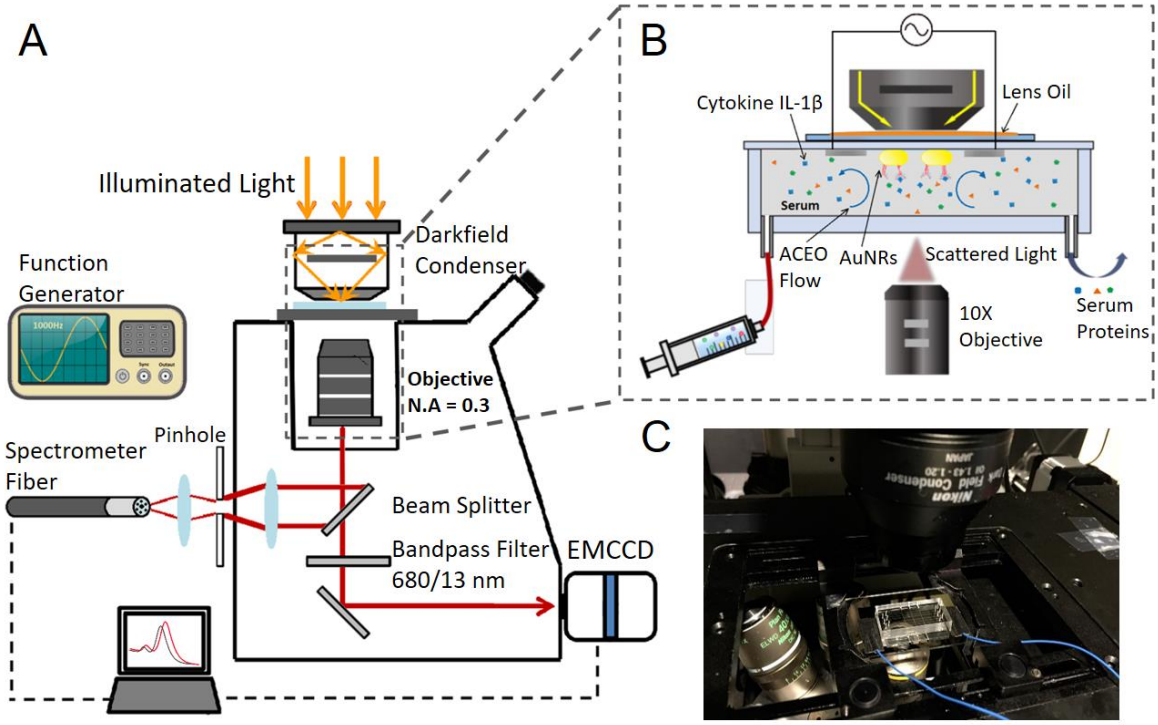

Figure 6.4 (A) Schematic of the dark-field microscopy setup used in this study. (B) Illustration of the ACE-LSPR biofunctional nanoparticle imaging process. (C) Photo image of the ACE-LSPR device mounted on the motorized X-Y stage of the dark-field microscopy setup.

6.2.4 Modeling of Electrical Double Layer.

Modeling the ACEO effect accompanying our device operation is a key task of the theoretical part of this study. First, the long coplanar plate electrodes immersed in aqueous electrolyte were modeled as a series of distributed capacitors associated with the electrical double layer and

semicircular resistors due to the electrolyte. The potential drop across the electrical double layer is given by (196)

$$\Delta\phi_{EDL} = \frac{V_0}{2 + i\omega\pi(\varepsilon/\sigma)\kappa x} \qquad (1)$$

where V_0 and ω are the peak value and frequency of the applied AC bias, respectively, ε and σ are the permittivity and conductivity of the electrolyte, respectively, κ is the reciprocal Debye length, which is the function of the ionic strength of the solution, and x is the distance from the center between the two coplanar microelectrodes. This equation is valid when V_0 is small enough to avoid an additional electrochemical effect and ω is much smaller than the relaxation frequency of the solution. Since the thickness of the electrical double layer is small compared to the microfluidic channel height, a linear relationship was assumed between the surface ion charge density σ_s and the potential drop across the diffuse layer $\Delta\phi_{EDL}$ as $\sigma_s = \varepsilon\kappa\Delta\phi_{EDL}$. The electrical force acting on the fluid was derived by Coulomb's law, which is opposed by the viscous force of the fluid as

$$F_E = E_t\rho_e dy = -\mu\left(\frac{d^2u_{ACEO}}{dy^2}\right)dy \qquad (2),$$

where E_t is the tangential component of the electric field, ρ_e is the charge density, μ is the dynamic viscosity of the solution. Integrating Equation (2) from infinity ($y = \infty$) to the electrode surface ($y = 0$) and combine the surface charge expression, we derived the AC electroosmosis velocity u_{ACEO} as shown in the main text. It should be noted that although a more complicated electrical double layer modeling may be needed especially for high ion concentration conditions, this simple circuit model fairly well predicts the experimentally observed flow velocity fields in the solution, and thus is sufficient for providing insights into the physical phenomena governing the ACE-LSPR device performance.

6.2.5 ACEO Flow Visualization and Particle Image Velocimetry (μ-PIV) Analysis.

AuNRs (l=84 nm, d=40 nm) were used as tracer particles to visualize the flow patterns within the fabricated device. The particle motions were observed using the above-described darkfield microscope (Figure 6.4) and recorded by the EMCCD camera. We selected the operating voltage and frequency in a buffer solution with varying ion concentration such that the fastest particle motions were visually observed from the dark-field image. The buffer solution we used were 0.001x phosphate-buffered saline (PBS) and 50% DI diluted human serum matrix (HSM). The colloidal medium suspending gold nanoparticles was first centrifuged in a tube. The original medium was collected from the tube using a pipette and replaced by the PBS solution. The gold nanoparticles in the PBS solution were loaded into the microfluidic channels of the ACE-LSPR device. The gold nanopartilces are much smaller than fluorescent latex spheres normally used in conventional particle image velocimetry for flow visualization. The small mass of the nanoparticles together with the non-fluorescence detection approach has the potential to visualize even weak flow patterns in a nanofludic environment without photobleaching. We took videos that showed nanoparticle motions resulting from a vortex flow pattern whose center of circulation was close to the electrode edge as predicted by our theoretical calculation. As the buffer was switched from PBS to HSM, the speed of the nanoparticle motions significantly decreased due to an increase of the ion concentration in the medium. The video also showed flow patterns at different frequencies. The fastest nanoparticle motions were observed at 1kHz in HSM, thus suggesting that it is close to the optimum ACEO bias frequency. Note that some aggregation of nanoparticles due to the positive dielectrophoretic effect was visualized at the edge of the electrodes under condition $V_0 = 2V$ at f=1kHz. This dielectrophoretic effect could cause non-specific adsorption of free background proteins occurred in serum.

This study developed a flow visualization technique to characterize ACEO velocity fields experimentally within the ACE-LSPR device based on 2D micron resolution particle image velocimetry (μ-PIV) analysis. An open source MATLAB toolbox (197) was utilized to perform image processing and fluid velocity field measurement. We captured a video series of the gold nanorods moving in the 0.001x PBS buffer (σ = 1.59 mS/m) at V_0 = 1V and 16.67 frame/s with the frequency varied using darkfield microscopy. Since the video were taken from the top view, the focal plane was fixed at 40 μm above the microelectrode surface to ensure the image quality and unidirectional flow. Some image preprocessings were first applied to enhance the image contrast, filter the background noise, and remove the very bright particle spots. A region of interest (ROI) was then selected around the electrode surface as depicted by the blue dotted line in Figure 6.5A. A mask image was placed at the center of the microelctrodes so that the out of plane flow will not be quantified. Cross-correlation functions were built up based on a fast Fourier transform (FFT) algorithm. Lastly, the velocity field at the frame rate was visualized with arrows as shown in Figure 6.5A. Figure 6.5B shows the theoretical and experimental ACEO velocity values at x =17.5 μm from the center of the microelectrodes at frequency 200Hz. The scattered dots represent experimental values obtained by averaging the tracing particles' x-direction velocity along the red dotted line (shown in Figure 6.5A) at V_0 = 1V while the curve represents an simulation obtained at V_0 = 0.613V. Here, anticipating experimental uncertainties associated with our electronics setup, the value of V_0 in the simulation was slightly corrected to be lower to match the theoretical ACEO velocity value with the one measured at the operational frequency of 200Hz. Note that the bell-shaped simulation velocity is slightly narrower than the experimental results. A similar discrepancy was also found by N.G. Green et al. (198), which is likely to be caused by the simplified linear assumption in the electrical double layer model as mentioned above and the

deviation of the relaxation time $\tau = \varepsilon/\sigma$ associated with the fabricated electrodes from the theoretical value. Nonetheless, combining the μ-PIV measurement and the theoretical mass transfer calculation allows us to accurately estimate the upper bound for the ACEO enhancement of biosensing.

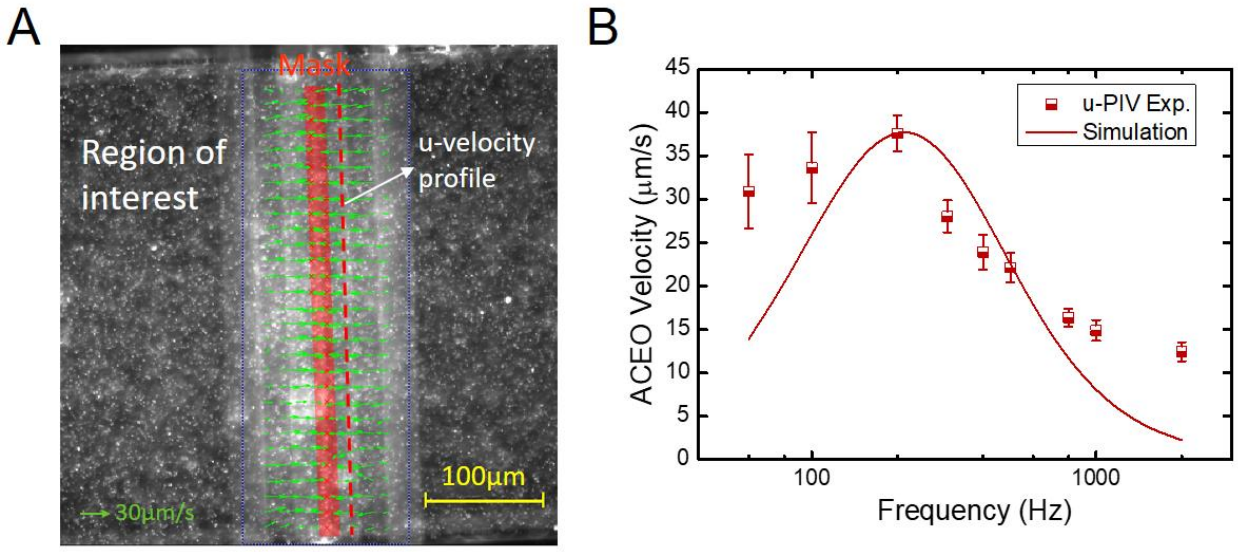

Figure 6.5 (A) Fluid velocity field measured by 2D micron resolution particle image velocimetry (μ-PIV) analysis. Images of the gold nanorods moving in the 0.001x PBS buffer (= 1.59 mS/m) were captured at 16.67 frame/s using darkfield microscopy with a focal plane at 40 μm above the microelectrode surface. (B) Theoretical and experimental ACEO velocity at x =17.5 μm from the center of the microelectrodes at 200Hz. The scattered dots represent experimental values obtained by averaging the tracing particles' x-direction velocity values along the red dotted line in (a) at V_0 = 1V. The curve represents simulation results at a corrected value of V_0 = 0.613V.

6.2.6 ELISA Correlation Test.

The Invitrogen™ 96-well Human IL-1β ELISA Kit was used to quantify the level of human IL-1β in the same patient serum sample as we used for our ACE-LSPR assay. For the both tests, two identical sets of serum sample were prepared during each freeze-thaw cycle. The patient serum samples were diluted two times by DI water, and the standard curves were obtained using 50%

diluted heat inactivated and charcoal stripped human serum matrix (EMD Millipore) spiked by known concentrations of IL-1β.

6.2.7 T-Test for 5min Initial Slope Analysis.

The initial slope analysis for analyte binding curves under ACEO operation (ACE-LSPR binding curves) provides an effective and advantageous way to reduce the sampling-to-answer time for assays using label-free biosensors (35). Plotting the initial slope value as a function of the IL-1β concentration yielded a calibration curve showing a similar trend to the conventional method analyzing the signal intensity at the end point of the analyte biding assay. We found out that the selection of the time period from the starting point of the ACE-LSPR binding curve for which the initial slope value was extracted (initial slope extraction time) strongly affected the extraction of the calibration curve. To determine the minimum initial slope extraction time required for reliable calibration curve extraction, we performed a two-tailed heteroscedastic t-test. This analysis involved comparing the initial slope values obtained for the extraction time of 1, 2, 3, …, 7 min with the one obtained for the extraction time of 8 min, as shown by Figure 6.6. Here, fitting to the ACE-LSPR binding curve data within the first 8 min was found to yield the same initial slope value as fitting to the whole binding curve covering the entire incubation period of 15 min. Thus, the analysis took the value for the initial slope extraction time of 8 min as the reference. All the initial slope values obtained for time periods longer than 5 min show statistically insignificant differences ($P>0.2$) while these values were distinct from those obtained for time periods shorter than 3 min ($P<0.05$). Thus, we concluded that the incubation time of 5 min was long enough to yield an ACE-LSPR binding curve for which we can obtain consistent standard curve data. The initial slope analysis for the 5 min incubation allows us to perform the rapid analyte quantification for patient samples.

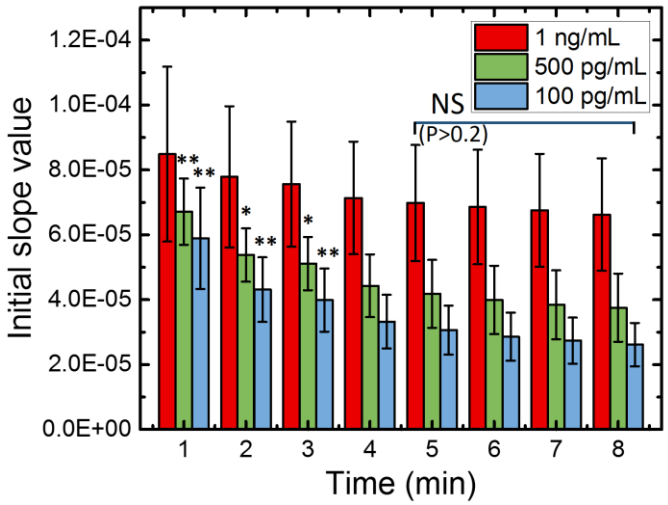

Figure 6.6 Initial slope values obtained from analyte binding curves under ACEO for the initial slope extraction time of 1 to 8 min. The time period of 5 min was determined as the minimum period to obtain the calibration curve. P values were calculated between the initial slope values for 1 to 7 min and the value for 8 min for the IL-1β concentration at 100 pg/mL, 500 pg/mL, and 1 ng/mL. *, p-value < 0.05; **, p-value < 0.01; NS, no significant difference.

6.3 Results and Discussion

6.3.1 Theoretical Study of ACE-LSPR.

Figure 6.7A provides a schematic illustration of the theoretical model for the ACEO-enhanced analyte transport and surface reaction during the ACE-LSPR optofluidic device operation. Using a simplified two-dimensional model, AC electroosmosis velocity u_{ACEO} was first calculated from the movement of the electrical double layer in the presence of an alternating tangential electric field at the frequency f near the electrode surface as (198)

$$u_{ACEO} = \frac{1}{8}\frac{\varepsilon V_0^2 \Omega^2}{\mu x(1+\Omega^2)^2}\frac{C_S}{C_S + C_D} \qquad (3)$$

where Ω is the non-dimensional frequency defined as $\Omega = \pi^2 \kappa x(\varepsilon_m/\sigma_m)f$, in which κ is the reciprocal of the Debye length, and ε_m and σ_m are medium electrical permittivity and conductivity, respectively, μ is the dynamic viscosity of the solution, C_S is the capacitance of the

Stern layer, or the thin layer of tightly associated counter ions near the electrode surface, C_D is the capacitance of the Diffuse layer, or the layer behind the Stern layer in which the electric potential exponentially decays, and V_0 is the peak value of the applied potential. The AC electroosmosis velocity u_{ACEO} was then included into the slip boundary condition when solving the incompressible Navier-Stokes (N-S) equation to obtain the velocity field (u, v) of the solution. The transient local analyte concentration $c = c(x, y, t)$ was then calculated by solving the mass transport equation that accounts for both diffusion and convection, given by

$$\frac{\partial c}{\partial t} = D\left(\frac{\partial^2 c}{\partial x^2} + \frac{\partial^2 c}{\partial y^2}\right) - \left(u\frac{\partial c}{\partial x} + v\frac{\partial c}{\partial y}\right) \qquad (4)$$

where D is the diffusion coefficient. At the sensor surface ($y = 0$), the boundary condition was set up such that the analyte mass flux is balanced with the surface binding reaction rate based on the first-order Langmuir absorption model as

$$-D\frac{\partial c}{\partial y} = k_{on}c|_{y=0}(B_0 - B) - k_{off}B \qquad (5)$$

where k_{on} and k_{off} are association/dissociation constants, B_0 is the initial binding site density, and B is the immobilized antigen concentration. Here, the key parameters to be optimized are the applied voltage, frequency, and microfluidic chamber height under different ionic concentrations in solution. Both the applied voltage and frequency determine u_{ACEO} while the microfluidic chamber height affects the entire mass transport process. The inlet and outlet were set as an "open boundary", where the local concentration is equal to the bulk solution concentration under zero normal stress. Table 6.1 summarizes key parameters used for our simulation and device design. The dissociation constant k_D was estimated based on published cytokine binding kinetics (93, 199). Note that the electrode thickness was carefully selected to be 60 nm in our device, higher than AuNR's diameter (40nm) to ensure the binding is well-protected from the movement of the

electrical double layer. Previous study (200) suggests that too high a flow velocity on the electrode surface at a high voltage may pull the antigen out of the bond, thus causing a negative effect.

Table 6.1 Simulation and design parameters selected for the ACE-LSPR device.

Simulation Parameter		Design Parameter	
k_D (M)[10-11]	10^{-11}	$w_{electrode}$ (μm)	50
k_{on} ($M^{-1}s^{-1}$)	3×10^{7}	$h_{electrode}$ (nm)	10 (Cr)+50 (Pt)
k_{off} (s^{-1})	3×10^{-4}	w_{gap} (μm)	25
C_0 (ng/ml)	1.0	$w_{channel}$ (μm)	400
D (m^2s^{-1})	10^{-11}	$h_{channel}$ (μm)	80
$h_{channel}$ (μm)	60-140	$l_{channel}$ (cm)	2
$w_{electrode}$ (μm)	50		
V_0 (V)	1-4		
f (Hz)	50-100000		
σ (mS/m)	1.590		

In order to accurately predict the enhancement of the ACEO-facilitated analyte transport and surface reaction, we experimentally verified the ACEO velocity calculated above using a flow visualization technique developed in this study (see 6.2.5). This technique employed AuNRs suspended in a testing buffer solution as tracing particles. Real-time imaging of particle trajectories with a darkfield microscopy setup allowed us to measure the flow velocity field within the device under ACEO operation by two-dimensional (2D) micron resolution particle image velocimetry (μ-PIV) analysis. We quantitatively observed a good match between our theory and experiment for frequency-dependent ACEO flow behaviors and determined the best operating frequency to be f = 200Hz for the testing buffer (conductivity: 1.59 mS/m), as shown in Figure 6.5.

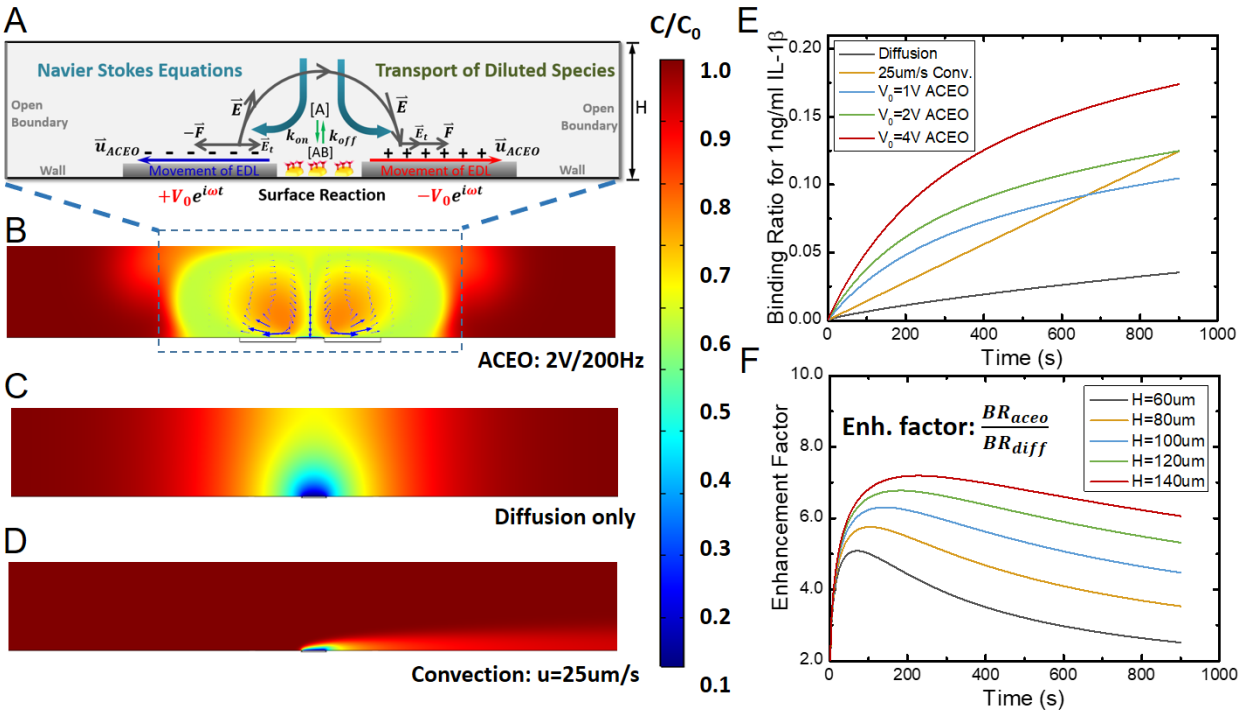

Figure 6.7 2D Finite-element analysis (FEA) simulations on the mass transport and surface reaction in the ACE-LSPR optofluidic device. (A) Simulation setup and boundary conditions. The ACEO velocity was first characterized by calculating the movement of the electrical double layer driven by the tangential component of the electric field using Coulomb's law. This velocity was then coupled with incompressible N-S equation to solve for the flow field, which was subsequently integrated with Fick's law to derive the concentration profile. Finally, the first order Langmuir Absorption was adopted as a boundary condition accounting for the surface reaction at the sensor surface. (B)-(D) Analyte concentration profiles within microfluidic channel of the device operated under ACEO at $V_0 = 2V$ $f = 200Hz$, with diffusion only, and with convection flow at 25 μm/s, respectively. The ACEO velocity direction and magnitude are shown by the blue arrows. The initial concentration for all three cases was set to be $c/c_0 = 1$. The inlet (left edges) and the outlet (right edges) for ACEO and diffusion only cases were defined as open boundaries with no analyte replenishment ($c/c_0 = 1$ at $x = \infty$). (E) Time-course change of binding ratio (BR) for different operating conditions. The BR is defined as the ratio of analyte occupations over the entire available binding sites. (F) Time-course change of enhancement factor for different channel heights under ACEO operation at $V_{p-p} = 2V$ $f = 200Hz$. Here, the enhancement factor is defined as the BR under ACEO over the BR under the condition of diffusion only.

Using the experimentally verified model, we calculated the binding ratio $BR = B/B_0$ (the fraction of binding sites occupied by analyte molecules over the total sensor surface area) after an incubation period of 20 min for three assay conditions: (1) ACEO agitated incubation without forced convection at V_0 = 2V and f = 200Hz (Figure 6.7B), (2) static incubation driven by pure

diffusion without forced convection or ACEO (Figure 6.7C), and (3) forced convection without ACEO (Figure 6.7D). The ACEO operation at 2V/200Hz was later determined to yield the optimal biosensing condition. The value of *BR* was assumed to be proportional to the LSPR scattering light intensity. Figure 6.7B shows that the circular flow generated by ACEO can significantly suppress the depletion zone as compared to the static incubation condition in which sample solution is not replenished at the sensor surface. Figure 6.7E shows numerical results of *BR* over time for human cytokine IL-1β at 1 ng/mL in 1000 times diluted (0.001x) PBS (conductivity: 1.59 mS/m) with an ionic strength of 0.2105 mol/m^3. Here, we chose IL-1β, a proinflammatory cytokine (cell signaling protein) produced by monocytes and macrophages, as the model analyte in our study. IL-1β has a relatively low molecular weight (17 kDa) and a small dissociation constant (10^{-10}-10^{-11}M), and is responsible for systemic inflammatory responses of the host, activation of phagocytes, and production of acute phase proteins by the liver (201).

With the optimum frequency fixed at f = 200Hz, we further varied the applied voltage and channel heights. Since u_{ACEO} scales with V_0^2 (see Equation (3)), our simulation in Figure 6.7E shows that BR is significantly enhanced as V_0 increases from 1V to 4V. Now, we define the enhancement factor as BR_{ACEO}/BR_{Diff}, where BR_{ACEO} and BR_{Diff} are the binding ratios under ACEO agitated incubation (Figure 6.7B) and the diffusion-driven static incubation (Figure 6.7C), respectively. The enhancement factor thus quantifies the ACEO-driven enhancement of the analyte binding at the sensor surface. Figure 6.7F shows the enhancement factor as a function of time and channel height, with its maximum 5-7 fold reached within the first 3-5 min of device operation. When the channel height is small, the confinement of fluid by the channel ceiling suppresses ACEO-induced fluid mixing. Without forced convection of the sample fluid, the analyte depletion zone quickly grows over time since no analytes are replenished at the sensor surface. A larger

channel height prevents the depletion region from reaching the channel ceiling, effectively increasing the enhancement factor. However, the enhancement starts to taper off with the channel height exceeding ~140 μm as ACEO-induced fluid mixing decreases with the distance from the electrode. To keep the fabrication practically easy, we selected a channel height of 80 μm.

6.3.2 Experimental Validation of ACE-LSPR.

We next experimentally demonstrated detection of low-concentration IL-1β using the AuNR optofluidic device and ACEO-induced fluid mixing operation. To this end, we first conjugated anti-IL-1β to AuNR surfaces using a two-step EDC/sulfo-NHS protocol (see 6.2.2). The use of a low conductivity medium, 0.001x PBS buffer (1.59 mS/m), was expected to achieve high ACEO velocity without undesired heat generation and electrolysis. To monitor the real-time binding of IL-1β on the sensor surface, we recorded the scattering intensity change of the line-shaped AuNR sensor patterns every 5s. Figure 6.8 shows time-resolved intensity change upon analyte binding, corresponding to the IL-1β concentration from 50 fg/mL to 100 pg/mL in PBS (0.001x) buffer along with a negative control. The assay started with sample loading for 5 min and incubation for another 5-6 min, followed by applying an AC bias of 180° phase difference for around 15 min. We observed a significantly enhanced intensity shift and a much faster binding speed towards equilibrium after introducing the ACEO flow (indicated by the dashed blue line in Figure 6.8).

As a result, we were able to distinguish the signal indicating the presence of IL-1β in PBS down to 50 fg/mL (2.9 fM) from the signal of the negative control (purple line, Figure 6.8) within 10 min after turning on ACEO. In Figure 6.8B, the end-point intensity increases of the triplicated AuNR line-shaped sensor patterns are mapped at different analyte concentrations with and without ACEO. Figure 6.8C shows a close comparison of sensor responses as a function of IL-1β concentration with and without ACEO. Here, we define the LOD as the analyte concentration

which generates a signal corresponding to 3 standard deviations above the mean of the noise level in the negative control (107). The LOD of the ACE-LSPR device is thus 158.5 fg/mL (9.1 fM) in 0.001x PBS, 100 fold more sensitive than that without ACEO (Figure 6.8C). In addition, enhanced analyte-antibody interaction by ACEO yields a larger number of binding events occurring at the sensor surface, as indicated by the ~2.5 times increase of scattering signal with ACEO (Figure 6.8). This is the key reason for the ACE-LSPR device to achieve such a low LOD value and short assay time. It should be noted that the signal enhancement ratio is around 40% smaller than the theoretical predictions. This discrepancy is acceptable, considering (i) the assumption made to simplify our model, in which the ion charge density on the microelectrode surface induced by the applied AC bias is linearly proportional a potential drop in the electrical double layer, and (ii) uncertainties in model parameters (see 6.2.4 for simulation details).

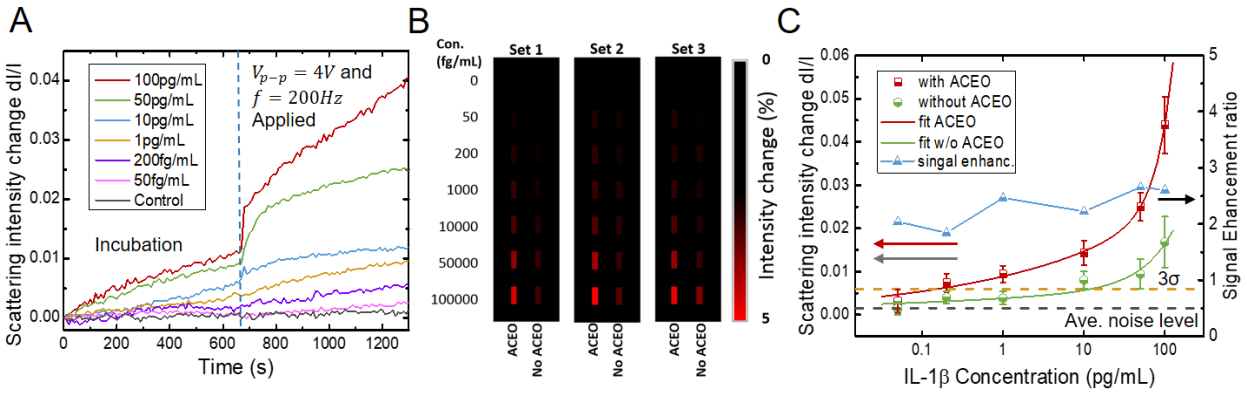

Figure 6.8 Detection of purified IL-1β in 0.001x PBS buffer. (A) Real-time scattering light intensity profiles of the line-shaped ACE-LSPR AuNR sensor patterns at various IL-1β concentrations (50 fg/mL to 100 pg/mL). Here, the operation condition at $V_{p-p} = 4V$ $f = 200Hz$ was applied after 10-11 min of incubation. (B) Darkfield images showing the mapping of the scattering intensities of triplicated sensing patters under conditions with/without ACEO. (C) Calibration curves obtained from the intensity mapping in b (left y axis). The LOD was determined by the intersection of the fitted calibration curve with 3 standard deviations (3σ) above the mean of the background noise. The LOD was calculated to be 158.5 fg/mL (9.1 fM) for "with ACEO" and 15.2pg/mL for "without ACEO". A reduction of LOD by two orders of magnitude was achieved. The signal enhancement ratio (right *y* axis) was calculated by the scattering intensity change for the "with ACEO" condition over the "without ACEO" condition. The "without ACEO" condition data were obtained from the intensity change of the Ref bar shown in Figure 6.1E.

To explore the practical utility of the ACE-LSPR device for clinical diagnosis, we further sought to detect human IL-1β in complex human serum, which has a greater ionic strength and contains a wide spectrum of background proteins. From Equation (3), it is known that ACEO flow velocity decreases with ion concentration, which causes the optimum operating frequency to shift to a higher value. A higher ion concentration also potentially introduces other undesirable effects, such as Joule heating, DEP concentrating, and electrolysis. These additional effects can adversely affect the stability of the sensor performance (184) and are difficult to predict by theory. Therefore, we empirically chose a 50% DI water diluted, cytokine-free heat inactivated and charcoal stripped human serum matrix (HSM, EMD Millipore) as the testing buffer. And we determined the optimum device operation condition to be $V_{p-p} = 1.5V$ at f= 1kHz based on the flow visualization. Following the same protocol described previously, we obtained real-time analyte binding curves from 1 pg/mL to 10 ng/mL of IL-1β spiked-in human serum and the corresponding calibration curves, as shown in Figure 6.9A and B, respectively. A strong binding enhancement was observed immediately at 6 min, which is the time point when the bias was applied. This strong binding enhancement is similar to what we observed in the test using PBS buffer but may not entirely due to the ACEO fluid transport. It should be noted that even for the negative control (human serum without IL-1β spiked), we observed a noticeable enhancement of binding by implementing ACEO. This could be attributed to the non-specific adsorption of free background proteins in serum promoted by the positive DEP effect at the electrode edges, as discussed in previous studies (192). Therefore, we incorporated a washing step with deionized (DI) water at 20 min after the assay, in order to remove the non-specifically adsorbed proteins and to eliminate false signals. Based on the calibration curves, we determined the LOD of the ACE-LSPR device for human serum samples to be <1 pg/mL (58 fM), which is about one order of magnitude higher than the LOD in PBS buffer.

This higher LOD for human serum samples is likely due to the nonspecific binding of the complex human serum background that still partially remains after the washing step.

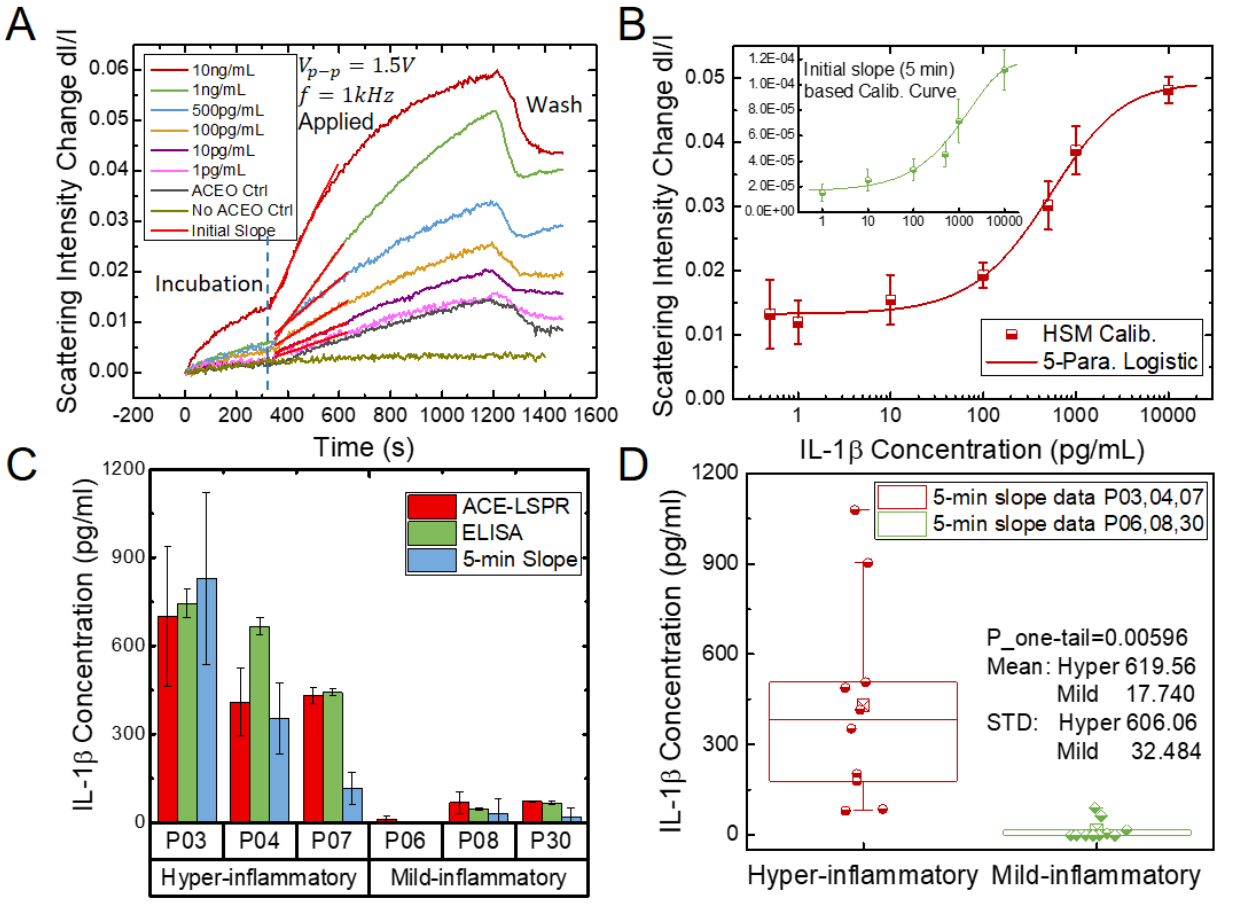

Figure 6.9 Detection of IL-1β in human serum. (A) Real-time scattering light intensity profiles of the line-shaped ACE-LSPR AuNR sensor patterns presenting enhanced signals for 50% human serum matrix (HSM) spiked by IL-1β at concentrations of 1 pg/mL to 10 ng/mL. Here, the operation condition at $V_{p-p} = 1.5V$ $f = 1kHz$ was applied after an incubation period of 5 min. (B) Calibration curves obtained from intensity mapping and 5 min initial slope analysis (shown by the inset). The raw data were fitted by a 5-parameter logistic function. (C) Serum IL-1β concentrations measured by three different methods for 6 pediatric sepsis patients stratified into hyper-inflammatory and mild-inflammatory subgroups. The labels of "ACE-LSPR," "ELISA," and "5-min Slope" indicate data obtained for the clinical samples by ACE-LSPR signal intensity analysis after an incubation period of ~15 min, conventional 96-well plate ELISA, and 5-min initial slope-based analysis, respectively. (D) One-tailed paired difference *t*-test performed for 5-min initial slope measurement between the two patient subgroups. The p-value calculated between the two patient subgroups is < 0.01.

We were able to extract the initial slope values of the binding curves within the first 5 min of sample incubation in the presence of ACEO. As shown by red bold lines in Figure 6.9A, a linear regression was utilized to fit the initial real-time binding curves. Here, we found good linear fits to the initial 5-min regions of the binding curves for IL-1β concentrations from 10 pg/mL to 1000 pg/mL (R^2>0.95) as the Langmuir model predicts. By plotting the initial slopes as a function of IL-1β concentration, a calibration curve with a similar trend to the scattering intensity-based analysis was obtained (Figure 6.9B inset). The selection of the incubation time for initial slope fitting would undoubtedly affect the shape of the calibration curve and the subsequent analysis of the biosensing performance. Here, we decided to use the first 5 min real-time binding data based on a variance analysis after carefully comparing the fitted data at different incubation time periods over the entire real-time dataset. (See 6.2.7). By correlating the analyte concentration with the initial slope of the sensor response curve, we could reduce the assay time down to ~5 min while most of other analyte diffusion-limited biosensor operations require much longer time for the system to reach its equilibrium.

6.3.3 Clinical Demonstration of ACE-LSPR.

Finally, we further measured IL-1β concentrations in serum samples extracted from six sepsis patients. Three of these patients were stratified into a hyper-inflammatory subgroup, and the other three are into a mild-inflammatory subgroup (49). All studies were approved by the University of Michigan Institutional Review Board (IRB) and conducted with informed parental consent. Blood samples were collected from patients younger than 18 years old, meeting criteria for septic shock admitted to the pediatric intensive care unit at the C.S. Mott Children's Hospital within 24 hours of admission. The tests were simultaneously performed using both ELISA and the ACE-LSPR device with 3 to 4 repeats in the same freeze-thaw cycle. Using the ACE-LSPR device, we

measured serum IL-1β across the patient samples from both the scattering intensity images obtained after the entire assay process and the 5-min initial binding curve slopes. These intensity and slope values were converted to IL-1β concentration values by 5-parameter logistic fitting (202), which is a standard fitting method in commercialized immunoassay (203) for plotting a sigmoidal shape calibration curve on the semi-log axes, as shown in Figure 6.9B**.** Figure 6.9C shows that the data obtained from the three different assay methods are consistent for all the patient samples. An excellent linear correlation ($R^2 = 0.947$) was obtained between the results from ACE-LSPR intensity imaging-based analysis and ELISA measurements across both the spiked-in and patient samples for the IL-1β concentration ranging from 1pg/ml to 1000pg/ml (Figure 6.10).

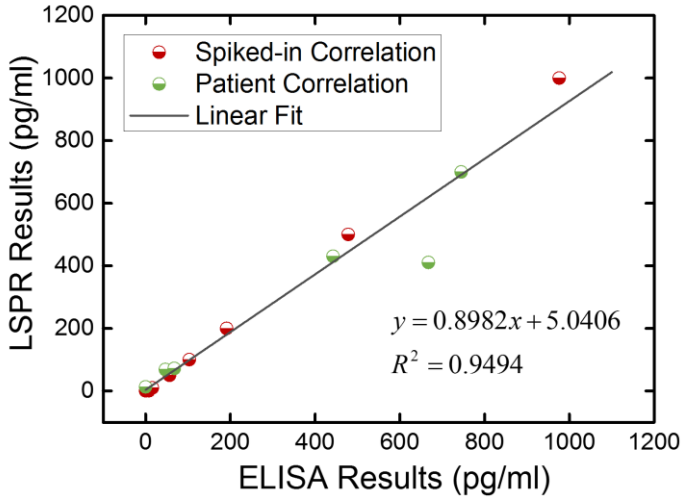

Figure 6.10 Correlation between data obtained from the ACE-LSPR and ELISA for both the spiked-in serum samples and patient samples with the IL-1β concentration ranging from 1 to 1000 pg/mL.

We performed one-tailed paired difference t-tests between the two patient subgroups using the 5-min initial slope data (Figure 6.9D). The result shows a significantly higher level of IL-1β ($P<0.01$) for the hyper-inflammatory subgroup as compared to the mild-inflammatory subgroup. This proves that the 5 min initial-slope assay can reliably distinguish the sepsis patients with either hyper-inflammatory or mild-inflammatory conditions. Although this initial-slope method could

potentially introduce some errors, the ultrafast assay time within 5 min offers unprecedented opportunities in clinical diagnosis to quickly determine the patients' immune conditions and to make timely stratification decisions.

Chapter 7

Conclusions and Future Work

7.1 Thesis Summary

This thesis has developed two ultrafast novel cytokine immunoassay platforms: the PEdELISA platform and the label-free ACE-LSPR platform to advance precision medicine of life-threatening acute illnesses in critical care. We have successfully demonstrated their applications towards near-realtime intervention of cancer immunotherapy, COVID-19, and sepsis-induced cytokine storm, which potentially allow clinicians to tailor the timing, frequency, and dose of the treatment specifically targeting the pathological origin. As a concluding remark, the PEdELISA platform holds great potential in the low-abundance protein profiling scenarios (121, 172) which require rapid turn-around, fine-time resolution, and low-sample volume by providing the combination of high speed, sensitivity, specificity, and multiplexity. Its low-cost and great inter-assay precision enable its application in daily monitoring of patient's biomarker status near the bedside. But meanwhile, we also note that comparing to the plate-based multiplex platforms (e.g. Luminex), the throughput of the assay for retrospective analysis may still need to be further improved. As a label-free immunoassay, the ACE-LSPR platform holds great potential in the application that requires real-time monitoring of molecular binding event, such as cellular immune-phenotyping and cell-to-cell communication mapping (182, 204, 205), or the scenarios for rapid, simple-step

high abundance proteins (e.g. Human Immunoglobulins) screening test, such as the COVID-19 antibody testing (206). The inherited limitation for assay's specificity and the practical viability for mass production are still challenges to be addressed in future clinical translations. The accomplishments of the thesis are summarized in the following sections respectively.

7.1.1 Rapid Single-molecule Digital Detection of Protein Biomarkers for Near-real-time Monitoring of Systemic Immune Disorders

In this study, we have introduced a "quench and snapshot" digital immunoassay approach, PEdELISA, that achieved fast, sensitive, cost-effective, and sample-sparing multiplex protein biomarker detection. We envision that future implementation of the PEdELISA platform will enable point-of-care cytokine profile measurements to guide biomarker data-driven management of CRS and other acute immunological diseases. It can also enable analysis of protein biomarkers in mouse blood samples in a longitudinal fashion within the same animal, which has broad application in studies of animal models of disease.

Digital protein assays have great potential to advance immunodiagnostics because of their single-molecule sensitivity, high precision, and robustness of the measurements. However, translating digital protein assays to acute clinical care has been challenging because existing technologies have a long turnaround time. Herein, we present a technology platform for ultra-fast digital protein biomarker detection by employing single-molecule counting of immune-complex formation events at an early, pre-equilibrium state. This method, which we term "pre-equilibrium digital enzyme-linked immunosorbent assay" (PEdELISA), can quantify a multiplexed panel of protein biomarkers in 10 µL serum within an unprecedented assay incubation time of 15-300 sec over a 10^4 dynamic range. PEdELISA allowed us to perform near-real-time monitoring of protein biomarkers in patients manifesting post-chimeric antigen receptor (CAR) T-cell therapy cytokine

release syndrome (CRS) with ~30 min serum sample to answer time and a ~1pg/mL limit of detection (LOD). The low input volume requirement also enabled high time-resolution, longitudinal serum cytokine measurement in a mouse model of sepsis. The rapid, sensitive and low input volume biomarker quantification enabled by PEdELISA is broadly applicable to timely, personalized management of acute disease in humans, as well as to longitudinal blood biomarker studies in various mouse models of disease.

Early intervention in evolving critical illness requires "real-time" data with high sensitivity. We developed a near-bedside ultrafast multiplex digital immunoassay to quantify serum protein biomarkers in evolving systemic immune disorders. Our study indicates that single-molecule digital counting of antigen-antibody complex reaction quenched at its early pre-equilibrium stage can achieve unprecedented incubation times that are >1000x shorter than gold-standard ELISA with a clinically relevant dynamic range of 10^4 and a sample volume < 5 μL. We applied the assay for real-time monitoring of sepsis biomarkers in mice and cytokines in leukemia patients with CRS due to CAR-T therapy. The captured biomarker dynamics manifest rapid feedback to drug treatment, which may guide individualized management with the optimal dose and timing of immunomodulatory interventions.

7.1.2 Machine Learning-Based Cytokine Microarray Digital Immunoassay Analysis

We expect that extending the multiplex capacity of digital immunoassay would greatly broaden its utility in the continuous monitoring of protein biomarkers for critically ill patients. However, multiplexing the assay becomes enormously difficult with an increasing number of target biomarkers. Multiplexed digital signal counting required over more than a few millions of fL-sized reactors with conventional methods experiences poor sample/reagent handling and declined accuracy due to various error sources. In this study, we developed a highly multiplexed digital

immunoassay platform, namely the PEdELISA microarray, to provide a promising solution for these challenges. The assay platform employs a unique combination of spatial-spectral encoding and machine learning-based image processing on a microfluidic chip. The positional registration of on-chip biosensing patterns, each with more than 40,000 microwell reactors confining sample sub-volumes, fluorescence-encoded analyte-capturing beads, and assay reagents, enabled 14-plex cytokine detection for 10 μL of serum with high sample handling efficiency, small reagent loss, and negligible sensor cross talk. The signal processing and analysis of the 14-plexed PEdELISA microarray analysis employed a novel parallel computing CNN-based machine-learning algorithm. This algorithm achieved autonomous classification and segmentation of image features (e.g. microwells, beads, defects, backgrounds) at high throughput (1 min/analyte). Notably, it yielded 8-10 fold higher accuracy than the conventional GTS-based algorithm without any human-supervised error correction.

We ran the PEdELISA microarray measurement of human serum samples from patients who received CAR-T cancer therapy with an incubation time as short as 5 min. The assay simultaneously detected 14 cytokine biomarkers per sample with a clinically relevant dynamic range of pM-nM, and the entire assay process from sample loading to data delivery was completed within 30 min. We tested blood samples obtained from a CAR-T patient at different time points during the course of the therapy with the short assay turnaround. The longitudinal measurement proved the ability of our assay platform to continuously monitor a large number of cytokine profiles that were rapidly evolving in the circulatory system of a patient manifesting CRS. With its speed, sensitivity, multiplexing capacity, and sample-sparing capability, the PEdELISA microarray is poised for future translation to critical care medicine. This technology could be

applied for guiding the treatment of life-threatening illnesses caused by COVID-19 global pandemic to be timely and tailored with the patient's comprehensive biomarker profiles.

7.1.3 A Digital Protein Microarray for COVID-19 Cytokine Storm Monitoring

Timely intervention of cytokine storm guided by rapid cytokine measurement is critical for the management of severe COVID-19 infections resulting in respiratory failure. To this end, we have developed a microfluidic digital immunoassay platform that enables rapid 4-plex measurement of cytokines in COVID-19 patient serum. Our assay employed single-molecule counting for an antibody sandwich immune-complex formation quenched at an early pre-equilibrium state. The pre-equilibrium approach resulted in a detection limit < 0.4 pg/mL and a linear dynamic range of 10^3 while requiring a total assay incubation time as short as 10 min. The platform incorporates a programmed fluidic dispensing and mixing module and a compact optical reader module for microfluidic analysis using low-cost disposable chips manufacturable at a large scale. Each chip contains spatially encoded microwell array patterns with capture antibody-coated magnetic beads pre-deposited for multiplex cytokine detection. The 4-plex on-chip measurement with a 15 μL sample volume showed negligible sensor cross-talk. The programmed fluidic handling and mixing module permitted high inter-assay repeatability (~10% CV). Our assay platform with the combination of high sensitivity, speed, and fidelity allowed us to complete a whole cytokine profiling test from initial blood draw with critically ill COVID-19 patients to data delivery to physicians within 4 hours.

This rapid cytokine assay was successfully implemented in real-time serial monitoring of two critically ill COVID-19 patients with severe cytokine storm and ARDS, and support their immunomodulatory therapies using the Selective Cytopheretic Device. Meanwhile, anti-IL6 therapy in COVID-19 is under investigation in multiple clinical trials and has been employed in

clinical practice as an off-label use. Preliminary results from trials of the anti-IL6 receptor antibody sarilumab have not demonstrated efficacy in moderately ill patients and trials continue in critically ill patients (207). Notably, our results here highlight the heterogeneity of cytokine response even among critically ill COVID-19 patients and the poor ability of surrogate inflammatory markers to predict an IL-6 response. These results confirm that rapid, reliable and repeatable direct cytokine measurement is needed to facilitate precision administration of anti-cytokine therapies only in patients who are experiencing cytokine storm. Our digital immunoassay platform may provide a promising means to enable such a precision medicine strategy in the pharmacotherapeutic management of life-threatening cytokine storm in COVID-19.

7.1.4 AC Electroosmosis-enhanced Nano-plasmofluidic Detection of Ultra-low-Concentration Cytokine

In this study, we have uniquely integrated AC electroosmosis with nanoplasmonic microfluidic biosensors and demonstrated that effective electrohydrodynamic agitation in bulk solution can significantly improve the label-free sensing performance of the nanoplasmonic biosensors. The ACE-LSPR biofunctional nanoparticle imaging technique applied to our device has achieved femtomolar-level detection of IL-1β, a pro-inflammatory cytokine, in PBS buffer with assay time less than 15 min using a sample volume as small as 5 μL. To the best of our knowledge, it is the most sensitive label-free nanoparticle-based plasmonic cytokine sensor reported so far. A compromised sensing performance is observed for the ACE-LSPR device when operating with high ion-concentration biological medium due to the augmented electrical screening effect. Nonetheless, we have successfully shown that 50% serum dilution still enables the ACE-LSPR device to retain its capability of enhancing the sensing speed and sensitivity even for complex human serum samples. Analyzing initial analyte binding curve slopes obtained from the ACE-

LSPR measurements, we have successfully demonstrated a 5-min cytokine immunoassay for stratifying sepsis patients into statistically distinct inflammatory status groups. The significantly improved sensitivity and shortened assay time clearly indicate the promising potential of the ACE-LSPR device for rapid screening and stratification of acute inflammatory diseases. Using micro-inkjet printing and 3D-stage controlled micro-brush patterning for AuNR patterning and antibody conjugation, we may potentially scale up the manufacturing throughput of the current device. Our future development of a faster, cheaper and smaller CMOS photon detector together with a high NA air condenser would allow our ACE-LSPR devices to be integrated in a handheld system, which would enable point-of-care personalized treatment with timely, precise immunomodulatory drug delivery.

7.2 Future Work

My doctoral research aims to provide a technology-based solution to enable near real-time monitoring of the patient's immune status and early interventions for severe cytokine storm. This thesis has proved the concept of the PEdELISA approach and demonstrated the preliminary setup of the platform for near-realtime monitoring the cytokine profiles of COVID-19 and CAR-T patients. The next critical steps toward the dissemination of PEdELISA to clinical research communities are to develop a fully automated, compact prototype instrument that can potentially be operated in a clinical lab using whole blood or even near the patient bedside. A low-cost mass-producible PEdELISA cartridge will also be explored using hot embossing and laser cutting microfluidic methods. The future direction on the clinical side will be focused on utilizing the developed high-throughput instrumentation to massively collect fine-time resolution cytokine profile data from CAR-T patients and mouse model. The data, together with mRNA sequencing will be used to statistically identify time-series cytokine profile signatures that determine the early

onset of severe CRS and predict the trajectory of the illness for biomarker-guided therapeutic interventions, such as IL-6R antagonist (tocilizumab) and other immunomodulatory approaches.

7.2.1 System Automation and Platform Translation.

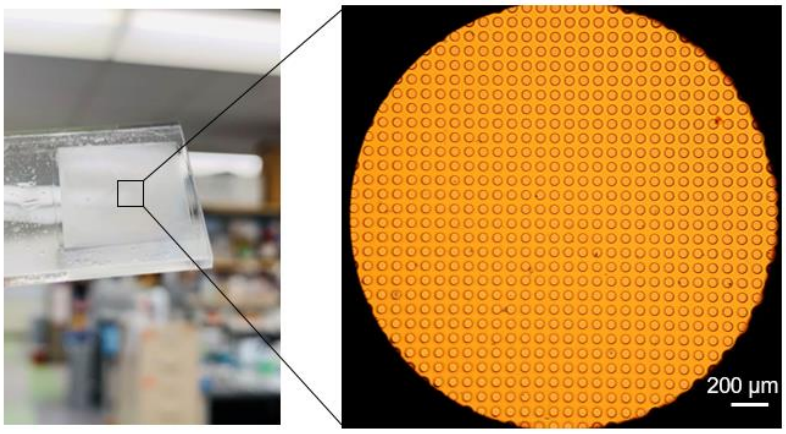

Figure 7.1 Preliminary test of the microwell fabrication on clear PMMA sheet using hot embossing method. The embossed the microwell diameter is 40 µm.

Future work should be performed to design and manufacture a mass-producible low-cost microfluidic cartridge with interfaces for automated microfluidic handling. The PDMS-based fabrication is a standard technique in the microfluidic research field for fast-prototyping with advantages of low-cost and sub-micrometer molding resolution. However, the soft nature of this silicone-based material and the slow curing process made the PDMS unsuitable for mass production and interfacing with automated fluidic pumping instrument. Here, I will explore the fabrication of the microwell structure using PMMA sheet by hot embossing and microfluidic channels by laser cutting. Our preliminary results have shown the success of transferring a 2cm-by-2cm microwell structure (d=40 µm) to the PMMA surface using a PDMS pillar array as the mold by heating to 125 °C for 10 min (Figure 7.1). Further in-depth tests will be performed to explore larger area pattern transfer (4-inch wafer) with smaller microwell sizes (e.g. d=4 µm) by

optimizing the embossing temperature, pressure, and mold type (e.g. PDMS, SU-8). Other materials like cyclic olefin copolymer will also be tested.

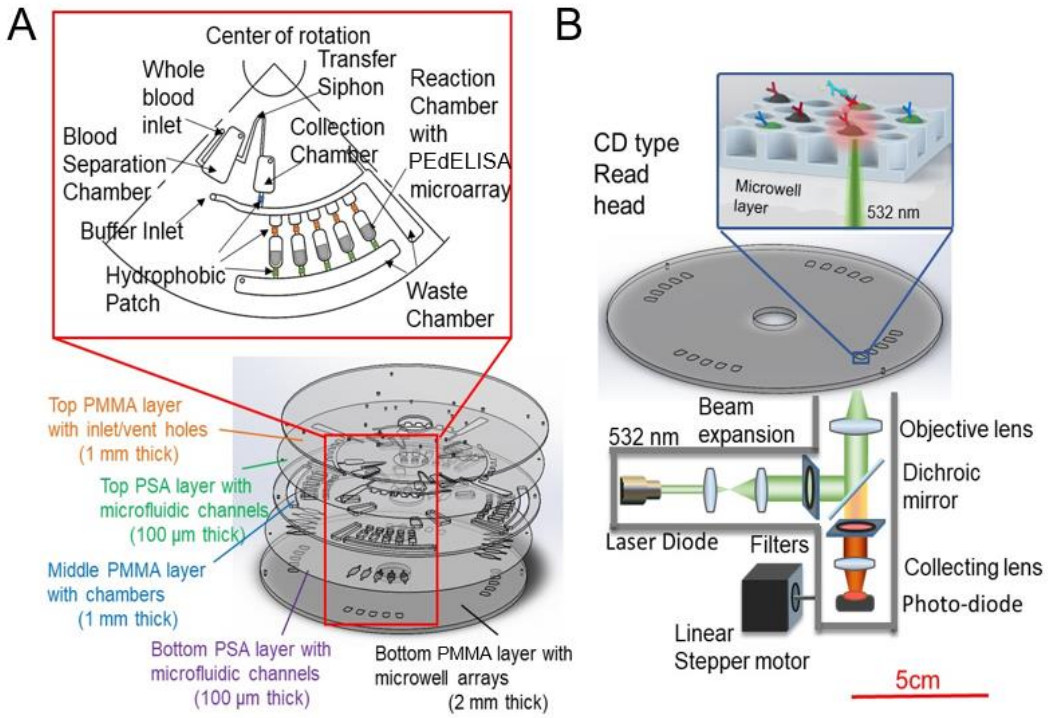

Figure 7.2 (A) Illustration of PEdELISA microarray disk design for integrated blood plasma separation, collection, metering and downstream multiplex PEdELISA analysis. The fabricated PEdELISA microarray disk has a multilayer structure consisting of a top vent layer (PMMA), top pressure sensitive adhesive layer with microfluidic channels (PSA), middle micro-chamber layer for sample storage (PMMA), bottom adhesive layer with microfluidic channels (PSA) and, bottom microwell array layer (PMMA). (b) Illustration of integrated laser scanning optics for high-throughput PEdELISA fluorescence digital counting analysis. The scanning principle is similar to that of a conventional CD-type read head.

Another direction of our future work is to further develop a fully automated, compact prototype instrument that can potentially be operated near-bedside. Lab-on-a-disk or centrifugal microfluidics has been proved to be promising for the development of commercial products for automated biochemical analysis (208-210). Although in Chapter 5, we have developed a 2-part semi-automated system for the COVID-19 study, the system's automation and integration level are still quite limited with bulky fluidic pipetting required. Here, I propose to develop a microfluidic compact disk (CD) device, the "PEdELISA Microarray Disk", which permits the

automated operations of blood plasma separation, reagent metering, PEdELISA assay on a 4-inch-diameter CD cartridge (Figure 7.2A). The device will have primarily three functional components: (i) a blood plasma separator (ii) a PEdELISA assay reactor and (iii) a laser scanning disk reader. The plasma separator will allow for plasma (supernatant of whole blood) processing steps, including sample inlet, blood cell sedimentation and plasma separation in a separation chamber, and plasma transfer into a collection chamber. We will optimize the microfluidic chamber/channel, valve design and operational conditions of our plasma separator according to the sample volume and purity needed for our downstream analysis. The separated plasma will be metered and transferred to the PEdELISA assay reactor which permits multiplex cytokine detection. The programmable fluid transfer on the disk will be activated using passive control valves. More specifically, siphon valves and a series of Teflon coated hydrophobic valves (activation frequency $f_{rot\,1} < f_{rot\,2} < \cdots, f_{rot\,n}$) will be designed and tested. Finally, the digital signal counting will be achieved by the high-speed laser scanner with a feedback position tracking mechanism for the rotating disk (Figure 7.2B). The "0" and "1" nature of digital immunoassay and the small microwell size make the PEdELISA suitable for a high-throughput laser scanning readout like a CD, except that the readout has to be fluorescence-based scanning. Therefore, we will develop a customized fluorescence laser scanning optics for high-throughput PEdELISA digital counting. With a moderate disk rotation speed at 200 rpm, the estimated reading rate will be ~5000 well/sec which will allow us to complete the entire digital counting within 1-min. The anticipated cost for the instrumentation of the new system is much less than that of a bulky high-end system incorporating a fully automated robotic machine for sample/reagent handling (51). I also anticipate this generic platform will have broader applications not only for cytokine storm, but also for a variety of time-sensitive critical illnesses, such as sepsis, systemic inflammatory response syndrome (SIRS), and

acute respiratory distress syndrome (ARDS). By designing and constructing a novel, compact, and mass-producible prototype instrument with a wide spectrum of potential applications will serve as the first step towards the future commercialization process.

7.2.2 Biomarker-guided Clinical Study.

For the CAR-T patient cytokine storm study, I will perform the multiplex analysis of 16 cytokine biomarkers in serum specimens longitudinally collected from >30 CAR-T patients (~400 samples) using the prototype instrument developed in the previous sections. This clinical study, which has already been IRB-approved (HUM00092161) and successfully initiated, collects serum longitudinally up to 5 times a week during pre-treatment, lymphodepleting chemotherapy, and CAR-T cell infusion stages, and the remainder of hospitalization (~2 weeks after CAR-T infusion). This is an on-going collaboration with the department of internal medicine which will focus on biomarker development for near-term prediction of severe CRS, enabling clinical trials for earlier interventions with IL-6R antagonist (tocilizumab) and other immunomodulatory therapeutic approaches.

For the mouse septic model study, I will first verify a novel sepsis biomarker, Citrullination of histone H3 (CitH3), in mouse cecal ligation and puncture (CLP) model and then demonstrate a novel strategy of sepsis treatment guided by real-time biomarker profile data. Previous studies (134, 138) indicates that blood CitH3 shows high specificity and selectivity that can distinguish sepsis from noninfectious conditions and predict sepsis outcomes. The pathological link between CitH3 and sepsis opens up a promising opportunity to establish a precise sepsis screening technique. Here, our treatment strategy is the double blockade of PAD-CitH3 pathway by blocking both intracellular PAD activity and extracellular circulating CitH3 with the hypothesis that this strategy will synergistically improve outcomes of sepsis (Figure 7.3)

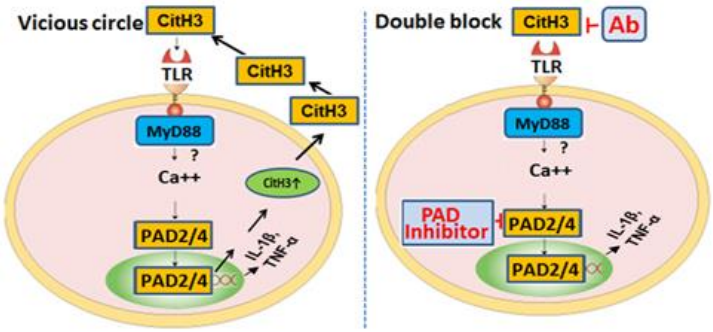

Figure 7.3 Double blockade of PAD-CitH3 pathway for the treatment of sepsis. PAD citrullinates H3 to produce CitH3; CitH3 triggers neutrophil extracellular traps (NETs) cell death (NETosis) to release nuclear contents, which forms a "vicious cycle" (left panel). PAD inhibitor with specific monoclonal anti-CitH3 antibody (Ab) for neutralization of circulating CitH3 (double block, right panel) can suppress PAD-CitH3 pathway and promote survival. TLR: Toll-like receptor; MPO: Myeloperoxidase; MyD88: Myeloid differentiation primary response gene 88; WT: wild type; KO: Knockout.

Briefly, we will first develop a 6-plex mouse biomarker panel which includes four cytokines: IL-6, TNF-α, IL-1β and IL-10, a widely used sepsis clinical marker procalcitonin (PCT) and the novel marker CitH3. We will then perform multi-time-point PEdELISA measurements of the 6 biomarkers from two groups of mice: 1) sham; 2) CLP (septic shock; ligated at 50%, 75%, and 100% of the total cecum length) mice and obtain high-resolution temporal biomarker profiles. Lastly, we will carry out the "double blockade of PAD-CitH3 pathway" study. Mice will be subject to various groups treated with different drugs, such as PAD inhibitor, Anti-CitH3 monoclonal antibody, or both etc. The drug(s) in each group will be administered at any measurement time point if the real-time CitH3 profile measured by PEdELISA reaches or exceeds the threshold value (in human patients it is 79 pg/mL for circulating CitH3) determined for each time point and the results represent novel CitH3-guided real-time interventions. We will monitor the survival rate and compare the therapeutic outcomes among them. The mice treated with vehicle serve as a control. Successful completion of this study will provide evidence that identifies biomarker-guided CitH3 blocking as a novel therapy for sepsis in a critical care setting which potentially supports a future clinical test for human patients.

Appendices

Appendix A. CAR-T patient clinical information

Patient A: Blood collection summary.

Subject ID	Day #	Serum Clot Time (min)
SC06	Baseline	42
SC06	-2	90
SC06	0	51
SC06	1	80
SC06	2	33
SC06	5	35
SC06	6	31
SC06	7	31
SC06	8	40
SC06	9	30
SC06	13	47
SC06	14	38
SC06	15	40
SC06	16	58

Patient A: Clinical intervention summary.

Patient A	Day #	Administer Time	Dose	Administer Type
Tocilizumab (ACTEMRA)	1	-	720 mg	Intravenous
Tocilizumab (ACTEMRA)	7	-	800 mg	Intravenous
Tocilizumab (ACTEMRA)	7	-	800 mg	Intravenous
Infliximab (REMICADE)	8	-	1100 mg	Intravenous
Infliximab (REMICADE)	11	-	500 mg	Intravenous
Methylprednisone	7	-	1000 mg	Intravenous
Methylprednisone	8	-	1000 mg	Intravenous
Methylprednisone	9	-	1000 mg	Intravenous
Dexamethasone (DECADRON)	11-16	Every 6 hrs	10 mg	Intravenous

Patient B: Blood collection summary

Subject ID	Day #	Serum Clot Time (min)
SC02	Baseline	52
SC02	0	121
SC02	1	47
SC02	3	60
SC02	9	45
SC02	11	33
SC02	14	36
SC02	15	36
SC02	17	68
SC02	24	60
SC02	31	57
SC02	37	43

Patient C: Blood collection summary

Subject ID	Day #	Serum Clot Time (min)
SC05	Baseline	42
SC05	0	50
SC05	1	50
SC05	3	46
SC05	7	55
SC05	9	35
SC05	11	45
SC05	14	30
SC05	21	32
SC05	23	32
SC05	28	51
SC05	35	50
SC05	38	40
SC05	43	33
SC05	50	45

Patient B: Clinical intervention summary

Patient B	Day #	Administer Time	Dose	Administer Type
Tocilizumab (ACTEMRA)	2	-	800 mg	Intravenous
Tocilizumab (ACTEMRA)	4	-	800 mg	Intravenous
Tocilizumab (ACTEMRA)	5	-	800 mg	Intravenous
Dexamethasone (DECADRON)	6	Every 6 hrs	8 mg	Intravenous
Dexamethasone (DECADRON)	7-11	Every 6 hrs	10 mg	Intravenous

Patient C: Clinical intervention summary

Patient C	Day #	Administer Time	Dose	Administer Type
Dexamethasone (DECADRON)	9-32	Every 6 hrs	10 mg	Intravenous

Appendix B. Procedures of PEdELISA Cytokine Measurement for COVID-19 Patients

Section 1. Multiplex Chip Patterning

Safety Protection:

- PPE: Lab coat, single layer surgical face mask, safety glasses, single layer nitrile exam gloves
- Only 1 person is needed (the other person stay 6-feet away for emergency help)
- Perform all the procedures on the wet bench
- No biohazard is generated for this section, standard waste collection.

Reagent Prep:

- EtOH – 1.5 mL in Eppendorf Tube
- Reagent PBST – 2 mL in Eppendorf Tube
- Superblock – 1.5 mL in Eppendorf Tube
- Capture Ab Beads. Stock is in 4C glass door fridge in COVID-19 box.
- IL-1B, TNF-a, IL-10, IL-6 BEADS – Dilute beads in 0.6mL Tube.
    - All: 4uL stock +21uL PBST

Procedure:

1. Clean and attach a multiplex loading channel to a NEW multiplex chip.
2. Wet the channels with PBST
3. Load Beads
    a. Slowly load 25uL beads into each channel in top-to-bottom order:
        i. IL-1B
        ii. TNF-a
        iii. IL-10
        iv. IL-6
    b. Check beads quality on microscope
    c. If loading is good, **gently** wash each channel with 200uL PBST **changing tip each time**
4. Change to sample loading channel and seal
    a. Load PBST into each loading channel slowly
5. Load 100uL superblock into each channel. Cover inlet and outlet with a cap. No need to change tip.
6. Incubate for at least 1 hour (or 4C over-night for the next day assay)

Section 2. Assay Preparation

Safety Protection:

- PPE: Lab coat, single layer surgical face mask, safety glasses, single layer nitrile exam gloves, protection disposable bouffant caps

- Two people are needed: stay 6-feet away from each other
- Perform all the procedures on the wet bench
- No biohazard is generated for this section, standard waste collection.
- Turn on the UV light in the biosafety cabinet at least 1hr before the assay for sterilization

Transfer COVID-19 Patient Sample to the biocabinet (right after received!):

- Wear all the PPE required plus **double gloves**
- Spray 75% EtOH on the biosafety cabinet surface, and sample bag/box surface (unopened)
- Place the unopened sample bag/box into the cabinet on Wet ice (0C)
- **Change gloves! Do not open the sample bag/box during this entire section!!!**

Reagents Needed:

- 100uL 100% FBS Aliquot (Frozen, -20C)
- Detection antibody cocktail stock (4-plex, 4C)
- Antigen cocktail stock (10ng/mL, 4-plex, -80C)
- HRP Stock (4C)
- Superblock (4C)
- 0.1% BSA Buffer (4C)

Procedure:

1. Label a 4x8 tube rack: assay standard unit: pg/mL

1								
2	**HRP**							
3	**1000**	**200**	**Sample 1**	**Sample 2**	**Sample 3**	**Sample 4**	**40**	**8**
4	**Detection Antibody**							

2. Add 20uL sterilized FBS from FBS COV aliquots to each standard in row 3
3. Perform serial dilution: (Mix 30x with pipette each time, do not change tip)
    a. Add 5uL antigen cocktail to 1000 pg/mL standard
    b. Take 5uL from 1ng and add to 200 pg/mL
    c. Take 5uL from 200 and add to 40 pg/mL
    d. Take 5 uL from 40 ng and add to 8 pg/mL
4. Add 15 uL Detection antibody cocktail stock to each tube in row 4
5. Dilute HRP 2.5uL stock + 372.5uL Superblock. Add 45uL to each tube.
6. Leave the Sample 1-4 empty for the next section
7. Seal each row individually and transfer the tube rack into the biosafety cabinet (on wet ice)

Section 3. Assay

Safety Protection:

- PPE: **Disposable Lab coat**, **Double-layer** surgical face mask (**N95 mask** is strongly suggested for this section if available), safety glasses, **face shield**, nitrile exam glove (as an inner layer), **long latex gloves (as the outer layer, seal the lab coat cuff),** protection disposable bouffant caps, **Protective Polyethylene Sleeve Covers**, Shoe cover (if available)
- Two people are needed! Later referred as **USER** and **HELPER**
- Perform all the procedures **inside the biosafety cabinet**
- **COVID-19 patient biohazards are generated in this section**, biohazard waste collection.

Biocabinet Prep:

- **Check all the reagents, washing buffer tray, and patient samples stored in the biosafety cabinet**
- Biowaste disposal bag in hood with enough room
- Paper towels in hood
- Hospital-grade disinfectant wash beaker in hood
- Plastic cup for wash lines
- A single 20uL pipette and three multi-pipettes in hood
- Prepare automated PEdELISA system:
    1. Motor power OFF, Arduino power (USB) OFF
    2. MultiCH-pipette set to 28.5uL.
    3. Reset motor starting location to the pipette plunger.
    4. Motor power ON
    5. Attaches sample loading lines.

Procedure:

1. Add 15uL patient samples (determine dilution ratio here!) to tube rack using 20uL gray pipette
2. Use a multichannel pipette to take 15uL from sample row and add to DeAb row. Mix 20x.
3. Start the automated system Arduino.
4. 10 second delay, then the system presses multichannel pipette plunger down
5. Plugin mixer lines to tube rack. The system draws up sample.
6. Plug into the chip.
7. Samples are dispensed into the chip. WIPE AWAY caps at the outlet side. IMMEDIATELY Spray EtOH on it and discard it into the biowaste bag.
8. Samples are mixed on-chip (for 8 minutes).
9. Mixer pushes the plunger halfway when done. Unplug mixer lines.
10. Insert washing lines.
11. 2 min washing start
12. After washing the system pusher will move back. USER adjusts the multichannel pipette to 40uL and ejects sample lines. (5 min)
    a. Immediately immerse the sample lines in a disinfectant beaker (75% EtOH)
    b. Install HRP lines to mixer
13. The system pushes down on pipette.

14. Plugin HRP lines into HRP tube row. The system draws up HRP.
15. DISCARD tube rack and plugin HRP lines to chip
16. The system quickly dispenses enough volume to displace PBST. Wipe away caps.
17. The system microsteps HRP into the device.
18. Microstepping is done after 1 min. Remove HRP lines and insert washing lines
19. Wash for 5 min.
20. During the wash, remove HRP lines and wash in disinfectant. Give both lines to HELPER to wash 5x in EtOH and DI water. Clean up the rest of the biosafety hood. HELPER leaves to turn on the PEdELISA reader and begin quanta red prep.
21. After the wash is done, leave the chip inside the hood, and wait for the QuantaRed reagent loading (prepared by the HELPER in the next section)

Section 4. Reagents Preparation for Imaging

Safety Protection:

- PPE: **Continue the PPE from the previous section!**
- Two people are needed: stay 6-feet away from each other
- Perform all the procedures on the wet bench
- No biohazard is generated for this section, standard waste collection.

Reagent Prep:

- QuantaRed Kit
- 1x PBS (not PBST!)
- HFE Oil

Equipment Prep:

- Turn on the PEdELISA reader, including light source, cameras, the scanning stage (UGS) and creating file path

Procedure

Done by HELPER during final assay wash (wet bench):

1. Add 100uL PBS to a 1.5mL tube
2. From Quanta Red Kit:
    a. Add 100uL H2O2 from glass bottle aliquot
    b. Add 100uL QRED enhancer from foil-covered aliquot
    c. Add 2uL QRED ADHP from foil-covered aliquot
3. Vortex well
4. Bring the QuantaRed solution and HFE Oil to the biosafety hood for the USER

The following will be Done by the USER (**biosafety cabinet!)**

At quick but controlled speed:

1. Add 30uL Quanta Red Solution to each channel (the chip) in order of imaging
2. Seal with 35uL oil into each channel in order of imaging
3. Cover inlets and outlets
4. Place the chip inside a petri dish and transfer it to the optics room.

Done by HELPER: while the USER is doing the imaging

1. Clean remaining surfaces in biosafety hood and turn on UV for >1 hour.
2. Spray 75% EtOH on all the biohazard's waste, seal the bag carefully and took them outside the biocabinet for autoclave.
3. Change gloves, take off the face shield but keep all the other PPE on!
4. Go and check if the USER need any help

Section 5. Image and Data Analysis

Safety Protection:

- PPE: **Continue the PPE from the previous section!** Except for no face shield
- Two people are needed: stay 6-feet away from each other
- Perform all the procedures on the wet bench
- The assay chip is the only biohazard that needs to be collected.

Procedure:

1. Set camera parameters: ISO 3200, Large, 1/8 sec EXP
2. Create a new file folder with assay date labeled on google drive
3. Save sensor spot positions: MATLAB code and UGS
4. Acquire fluorescence images
5. Acquire bright-field images
6. Run convolutional neural networks on the data (stored in the cloud)
7. Clean up and collect the chip as a biohazard.

Bibliography

1. Meager T. *The Molecular Biology of Cytokines.* New York, NY: John Wiley & Sons; 1998.
2. Thompson AW, and Lotze MT. *The Cytokine Handbook 4th Edition.* Amsterdam, Netherlands: Academic Press; 2003.
3. Dinarello CA. Historical insights into cytokines. *European Journal of Immunology.* 2007.
4. Schulte W, Bernhagen J, and Bucala R. Cytokines in Sepsis: Potent Immunoregulators and Potential Therapeutic Targets-An Updated View. *Mediators of Inflammation.* 2013.
5. Pai M, Riley LW, and Colford JM. Interferonn assays-gamma in the immunodiagnosis of tuberculosis: a systematic review. *Lancet Infectious Diseases.* 2004;4(12):761-76.
6. Lin CY, Roberts GW, Kift-Morgan A, Donovan KL, Topley N, and Eberl M. Pathogen-Specific Local Immune Fingerprints Diagnose Bacterial Infection in Peritoneal Dialysis Patients. *Journal of the American Society of Nephrology.* 2013;24(12):2002-9.
7. Payen D, Monneret G, and Hotchkiss R. Immunotherapy - a potential new way forward in the treatment of sepsis. *Crit Care.* 2013;17(1).
8. Rosenberg SA, Yang JC, and Restifo NP. Cancer immunotherapy: moving beyond current vaccines. *Nat Med.* 2004;10(9):909-15.
9. Ludewig B, Ochsenbein AF, Odermatt B, Paulin D, Hengartner H, and Zinkernagel RM. Immunotherapy with dendritic cells directed against tumor antigens shared with normal host cells results in severe autoimmune disease. *J Exp Med.* 2000;191(5):795-803.
10. Valenta R. The future of antigen-specific immunotherapy of allergy. *Nature Reviews Immunology.* 2002;2(6):446-53.
11. Targan SR, Hanauer SB, vanDeventer SJH, Mayer L, Present DH, Braakman T, et al. A short-term study of chimeric monoclonal antibody cA2 to tumor necrosis factor alpha for Crohn's disease. *New England Journal of Medicine.* 1997;337(15):1029-35.
12. Siebert S, Tsoukas A, Robertson J, and McInnes I. Cytokines as Therapeutic Targets in Rheumatoid Arthritis and Other Inflammatory Diseases. *Pharmacological Reviews.* 2015;67(2):280-309.
13. Ascierto PA, Fox BA, Urba WJ, Anderson AC, Atkins M, Borden EC, et al. Insights from immuno-oncology: The Society for Immunotherapy of Cancer statement on access to IL-6-targeting therapies for COVID-19. *Journal for ImmunoTherapy of Cancer.* 2020:in press.
14. Bienvenu J, Monneret G, Fabien N, and Revillard JP. The clinical usefulness of the measurement of cytokines. *Clinical Chemistry and Laboratory Medicine.* 2000;38(4):267-85.
15. de Jager W, te Velthuis H, Prakken BJ, Kuis W, and Rijkers GT. Simultaneous detection of 15 human cytokines in a single sample of stimulated peripheral blood mononuclear cells. *Clin Diagn Lab Immunol.* 2003;10(1):133-9.

16. Huang C, Wang Y, Li X, Ren L, Zhao J, Hu Y, et al. Clinical features of patients infected with 2019 novel coronavirus in Wuhan, China. *Lancet.* 2020;395(10223):497-506.
17. Collins FS, and Varmus H. A New Initiative on Precision Medicine *The New England Journal of Medicine.* 2015;372:793-5.
18. Piccart-Gebhart MJ, Procter M, Leyland-Jones B, Goldhirsch A, Untch M, Smith I, et al. Trastuzumab after adjuvant chemotherapy in HER2-positive breast cance. *The New England Journal of Medicine.* 2005;353:1659–72.
19. Politi K, and Herbst RS. Lung Cancer in the Era of Precision Medicine. *Clin Cancer Res.* 2015;21(10):2213–20.
20. Gladfelter P, Darwish NHE, and Mousa SA. Current status and future direction in the management of malignant melanoma. *Melanoma Res* 2017;27(5):403–10.
21. Lander ES, Linton LM, Birren B, Nusbaum C, Zody MC, Baldwin J, et al. Initial sequencing and analysis of the human genome. . *Nature.* 2001;409:860–921.
22. CancerGenomeAtlasN. Genomic classification of cutaneous melanoma. *Cell* 2015;161:1681–96.
23. Halpern NA, and Pastores SM. Critical care medicine in the United States 2000–2005: An analysis of bed numbers, occupancy rates, payer mix, and costs. *Crit Care Med.* 2010;38(1):65–71.
24. Laffey JG, and Kavanagh BP. Negative trials in critical care: why most research is probably wrong. *Lancet Respir Med.* 2018;6(9):659–60.
25. Seymour C, Gomez H, Chang C, Clermont G, Kellum J, Kennedy J, et al. Precision medicine for all? Challenges and opportunities for a precision medicine approach to critical illness. *Crit Care.* 2017;21:257.
26. Singer M, Deutschman CS, Seymour CW, Shankar-Hari M, Annane D, Bauer M, et al. The Third International Consensus Definitions for Sepsis and Septic Shock (Sepsis-3). *Journal of the American Medical Association.* 2016;315(8):801-10.
27. Sinha M, Jupe J, Mack H, Coleman TP, Lawrence SM, and Fraley SI. Emerging Technologies for Molecular Diagnosis of Sepsis. *Clin Microbiol Rev.* 2018;31(2):26.
28. Giannakopoulos K, Hoffmann U, Ansari U, Bertsch T, Borggrefe M, Akin I, et al. The Use of Biomarkers in Sepsis: A Systematic Review. *Curr Pharm Biotechnol.* 2017;18(6):499-507.
29. Pierrakos C, and Vincent JL. Sepsis biomarkers: a review. *Critical Care.* 2010;14(1).
30. Usuba R, Yokokawa M, Ackermann TN, Llobera A, Fukunaga K, Murata S, et al. Photonic Lab-on-a-Chip for Rapid Cytokine Detection. *Acs Sensors.* 2016;1(8):979-86.
31. Chen PY, Chung MT, McHugh W, Nidetz R, Li YW, Fu JP, et al. Multiplex Serum Cytokine Immunoassay Using Nanoplasmonic Biosensor Microarrays. *Acs Nano.* 2015;9(4):4173-81.
32. Park Y, Ryu B, Oh BR, Song YJ, Liang XG, and Kurabayashi K. Biotunable Nanoplasmonic Filter on Few-Layer MoS2 for Rapid and Highly Sensitive Cytokine Optoelectronic lmmunosensing. *Acs Nano.* 2017;11(6):5697-705.
33. Ryu B, Nam H, Oh BR, Song YJ, Chen PY, Park Y, et al. Cyclewise Operation of Printed MoS2 Transistor Biosensors for Rapid Biomolecule Quantification at Femtomolar Levels. *Acs Sensors.* 2017;2(2):274-81.
34. Hakim MMA, Lombardini M, Sun K, Giustiniano F, Roach PL, Davies DE, et al. Thin Film Polycrystalline Silicon Nanowire Biosensors. *Nano Lett.* 2012;12(4):1868-72.

35. Luchansky MS, and Bailey RC. Rapid, Multiparameter Profiling of Cellular Secretion Using Silicon Photonic Microring Resonator Arrays. *Journal of the American Chemical Society.* 2011;133(50):20500-6.
36. Min J, Nothing M, Coble B, Zheng H, Park J, Im H, et al. Integrated Biosensor for Rapid and Point-of-Care-Sepsis Diagnosis. *Acs Nano.* 2018;12(4):3378-84.
37. Tan XT, Oo MKK, Gong Y, Li YX, Zhu HB, and Fan XD. Glass capillary based microfluidic ELISA for rapid diagnostics. *Analyst.* 2017;142(13):2378-85.
38. McRae MP, Simmons G, Wong J, and McDevitt JT. Programmable Bio-nanochip Platform: A Point-of-Care Biosensor System with the Capacity To Learn. *Accounts of Chemical Research.* 2016;49(7):1359-68.
39. Song YJ, Chen PY, Chung MT, Nidetz R, Park Y, Liu ZH, et al. AC Electroosmosis-Enhanced Nanoplasmofluidic Detection of Ultralow-Concentration Cytokine. *Nano Lett.* 2017;17(4):2374-80.
40. Wang Y, Vaidyanathan R, Shiddiky MJA, and Trau M. Enabling Rapid and Specific Surface-Enhanced Raman Scattering Immunoassay Using Nanoscaled Surface Shear Forces. *Acs Nano.* 2015;9(6):6354-62.
41. Sanghavi BJ, Varhue W, Rohani A, Liao KT, Bazydlo LAL, Chou CF, et al. Ultrafast immunoassays by coupling dielectrophoretic biomarker enrichment in nanoslit channel with electrochemical detection on graphene (vol 15, pg 4563, 2015). *Lab Chip.* 2015;15(24):4626-.
42. Barik A, Otto LM, Yoo D, Jose J, Johnson TW, and Oh SH. Dielectrophoresis-Enhanced Plasmonic Sensing with Gold Nanohole Arrays. *Nano Lett.* 2014;14(4):2006-12.
43. Squires TM, Messinger RJ, and Manalis SR. Making it stick: convection, reaction and diffusion in surface-based biosensors. *Nat Biotechnol.* 2008;26(4):417-26.
44. Kanthor R. DIAGNOSTICS Detection drives defence. *Nature.* 2014;509(7498):S14-S5.
45. Abraham E. Why immunomodulatory therapies have not worked in sepsis. *Intensive Care Medicine.* 1999;25:556-66.
46. J.Kox W, T.Volk, S.N.Kox, and H.-D.Volk. Immunomodulatory therapies in sepsis. *Intensive Care Medicine.* 2000;26:S124-S8.
47. Osuchowski MF, Connett J, Welch K, Granger J, and Remick DG. Stratification is the key: Inflammatory biomarkers accurately direct immunomodulatory therapy in experimental sepsis. *Critical Care Medicine.* 2009;37(5):1567-73.
48. Fink MP, and Warren HS. Strategies to improve drug development for sepsis. *Nature Reviews Drug Discovery.* 2014;13(10):741-58.
49. Wong HR, Weiss SL, Giuliano JS, Wainwright MS, Cvijanovich NZ, Thomas NJ, et al. Testing the Prognostic Accuracy of the Updated Pediatric Sepsis Biomarker Risk Model. *Plos One.* 2014;9(1).
50. P. P, and M. K. Towards precision medicine for sepsis patients. *Crit Care* 2017;;21(1):11.
51. Wilson DH, Rissin DM, Kan CW, Fournier DR, Piech T, Campbell TG, et al. The Simoa HD-1 Analyzer: A Novel Fully Automated Digital Immunoassay Analyzer with Single-Molecule Sensitivity and Multiplexing. *Jala-J Lab Autom.* 2016;21(4):533-47.
52. Rissin DM, Kan CW, Campbell TG, Howes SC, Fournier DR, Song L, et al. Single-molecule enzyme-linked immunosorbent assay detects serum proteins at subfemtomolar concentrations. *Nature Biotechnology.* 2010;28(6):595-9.

53. Kim SH, Iino R, Iwai S, Araki S, Sakakihara S, and Noji H. Large-scale femtoliter droplet array for digital counting of single biomolecules (vol 12, pg 4986, 2012). *Lab Chip.* 2012;12(24):5284-.
54. Shim JU, Ranasinghe RT, Smith CA, Ibrahim SM, Hollfelder F, Huck WTS, et al. Ultrarapid Generation of Femtoliter Microfluidic Droplets for Single-Molecule-Counting Immunoassays. *Acs Nano.* 2013;7(7):5955-64.
55. Akama K, Shirai K, and Suzuki S. Droplet-Free Digital Enzyme-Linked Immunosorbent Assay Based on a Tyramide Signal Amplification System. *Anal Chem.* 2016;88(14):7123-9.
56. Zhang Y, and Noji H. Digital Bioassays: Theory, Applications, and Perspectives (vol 89, pg 92, 2017). *Anal Chem.* 2017;89(24):13675-.
57. Cretich M, Daaboul GG, Sola L, Unlu MS, and Chiari M. Digital detection of biomarkers assisted by nanoparticles: application to diagnostics. *Trends in Biotechnology.* 2015;33(6):343-51.
58. Engvall E, and Perlmann P. Enzyme-Linked Immunosorbent Assay, Elisa. *Journal of Immunology.* 1972;109(1):129-35.
59. Balci C, Sungurtekin H, Gurses E, Sungurtekin U, and Kaptanoglu B. Usefulness of procalcitonin for diagnosis of sepsis in the intensive care unit. *Critical Care.* 2003;7(1):85-90.
60. Cesaro-Tadic S, Dernick G, Juncker D, Buurman G, Kropshofer H, Michel B, et al. High-sensitivity miniaturized immunoassays for tumor necrosis factor a using microfluidic systems. *Lab on a Chip.* 2004;4(6):563-9.
61. Castanheira AP, Barbosa AI, Edwardsa AD, and Reis NM. Multiplexed femtomolar quantitation of human cytokines in a fluoropolymer microcapillary film. *Analyst.* 2015;140(16):5609-18.
62. Volpetti F, Garcia-Cordero J, and Maerkl SJ. A Microfluidic Platform for High-Throughput Multiplexed Protein Quantitation. *Plos One.* 2015;10(2).
63. Fan R, Vermesh O, Srivastava A, Yen BKH, Qin LD, Ahmad H, et al. Integrated barcode chips for rapid, multiplexed analysis of proteins in microliter quantities of blood. *Nat Biotechnol.* 2008;26(12):1373-8.
64. Sasso LA, Johnston IH, Zheng M, Gupte RK, Undar A, and Zahn JD. Automated microfluidic processing platform for multiplexed magnetic bead immunoassays. *Microfluidics and Nanofluidics.* 2012;13(4):603-12.
65. Garcia-Cordero JL, and Maerkl SJ. A 1024-sample serum analyzer chip for cancer diagnostics. *Lab on a Chip.* 2014;14(15):2642-50.
66. Yelleswarapu V, Buser JR, Haber M, Baron J, Inapuri E, and Issadore D. Mobile platform for rapid sub-picogram-per-milliliter, multiplexed, digital droplet detection of proteins. *Proceedings of the National Academy of Sciences of the United States of America.* 2019;116(10):4489-95.
67. Song YJ, Sandford E, Tian Y, Yin Q, Kozminski AG, Su SH, et al. *Submitted to Blood.* 2020:Under Review.
68. Prakadan SM, Shalek AK, and Weitz DA. Scaling by shrinking: empowering single-cell 'omics' with microfluidic devices. *Nat Rev Genet.* 2017;18(6).
69. Pekin D, Skhiri Y, Baret J-C, Le Corre D, Mazutis L, Ben Salem C, et al. Quantitative and sensitive detection of rare mutations using droplet-based microfluidics. *Lab on a Chip.* 2011;11(13):2156-66.

70. Hindson CM, Chevillet JR, Briggs HA, Gallichotte EN, Ruf IK, Hindson BJ, et al. Absolute quantification by droplet digital PCR versus analog real-time PCR. *Nature Methods.* 2013;10(10):1003-+.
71. Chang L, Song L, Fournier DR, Kan CW, Patel PP, Ferrell EP, et al. Simple diffusion-constrained immunoassay for p24 protein with the sensitivity of nucleic acid amplification for detecting acute HIV infection. *Journal of Virological Methods.* 2013;188(1-2):153-60.
72. Leirs K, Kumar PT, Decrop D, Perez-Ruiz E, Leblebici P, Van Kelst B, et al. Bioassay Development for Ultrasensitive Detection of Influenza A Nucleoprotein Using Digital ELISA. *Analytical Chemistry.* 2016;88(17):8450-8.
73. Obayashi Y, Iino R, and Noji H. A single-molecule digital enzyme assay using alkaline phosphatase with a cumarin-based fluorogenic substrate. *Analyst.* 2015;140(15):5065-73.
74. Rissin DM, and Walt DR. Digital readout of target binding with attomole detection limits via enzyme amplification in femtoliter arrays. *Journal of the American Chemical Society.* 2006;128(19):6286-7.
75. Shim J-u, Ranasinghe RT, Smith CA, Ibrahim SM, Hollfelder F, Huck WTS, et al. Ultrarapid Generation of Femtoliter Microfluidic Droplets for Single-Molecule-Counting Immunoassays. *Acs Nano.* 2013;7(7):5955-64.
76. Shembekar N, Hu H, Eustace D, and Merten CA. Single-Cell Droplet Microfluidic Screening for Antibodies Specifically Binding to Target Cells. *Cell Reports.* 2018;22(8):2206-15.
77. Liu C, Xu X, Li B, Situ B, Pan W, Hu Y, et al. Single-Exosome-Counting Immunoassays for Cancer Diagnostics. *Nano Letters.* 2018;18(7):4226-32.
78. Piraino F, Volpetti F, Watson C, and Maerkl SJ. A Digital-Analog Microfluidic Platform for Patient-Centric Multiplexed Biomarker Diagnostics of Ultralow Volume Samples. *Acs Nano.* 2016;10(1):1699-710.
79. Dutta PS, J.; Datskos, P. G.; Sepaniak, M. J. Nanostructured Cantilevers as Nanomechanical Immunosensors for Cytokine Detection. *NanoBiotechnology.* 2005;1:237-44.
80. Krishnamoorthy S, Iliadis AA, Bei T, and Chrousos GP. An interleukin-6 ZnO/SiO2/Si surface acoustic wave biosensor. *Biosens Bioelectron.* 2008;24(2):313-8.
81. Bahk YK, Kim HH, Park D-S, Chang S-C, and Go JS. A New Concept for Efficient Sensitivity Amplification of a QCM Based Immunosensor for TNF-alpha by Using Modified Magnetic Particles under Applied Magnetic Field. *Bulletin of the Korean Chemical Society.* 2011;32(12):4215-20.
82. Kongsuphol P, Ng HH, Pursey JP, Arya SK, Wong CC, Stulz E, et al. EIS-based biosensor for ultra-sensitive detection of TNF-alpha from non-diluted human serum. *Biosens Bioelectron.* 2014;61:274-9.
83. Pui TS, Kongsuphol P, Arya SK, and Bansal T. Detection of tumor necrosis factor (TNF-alpha) in cell culture medium with label free electrochemical impedance spectroscopy. *Sensors and Actuators B-Chemical.* 2013;181:494-500.
84. Liu Y, Tuleouva N, Ramanculov E, and Revzin A. Aptamer-Based Electrochemical Biosensor for Interferon Gamma Detection. *Anal Chem.* 2010;82(19):8131-6.
85. Qureshi A, Niazi JH, Kallempudi S, and Gurbuz Y. Label-free capacitive biosensor for sensitive detection of multiple biomarkers using gold interdigitated capacitor arrays. *Biosens Bioelectron.* 2010;25(10):2318-23.

86. Pui TS, Agarwal A, Ye F, Huang YX, and Chen P. Nanoelectronic detection of triggered secretion of pro-inflammatory cytokines using CMOS compatible silicon nanowires. *Biosens Bioelectron.* 2011;26(5):2746-50.
87. Mandal S, Goddard JM, and Erickson D. A multiplexed optofluidic biomolecular sensor for low mass detection. *Lab on a Chip.* 2009;9(20):2924-32.
88. Choi CJ, Belobraydich AR, Chan LL, Mathias PC, and Cunningham BT. Comparison of label-free biosensing in microplate, microfluidic, and spot-based affinity capture assays. *Anal Biochem.* 2010;405(1):1-10.
89. Luchansky MS, and Bailey RC. Silicon Photonic Microring Resonators for Quantitative Cytokine Detection and T-Cell Secretion Analysis. *Anal Chem.* 2010;82(5):1975-81.
90. Armani AM, Kulkarni RP, Fraser SE, Flagan RC, and Vahala KJ. Label-free, single-molecule detection with optical microcavities. *Science.* 2007;317(5839):783-7.
91. Chou T-H, Chuang C-Y, and Wu C-M. Quantification of Interleukin-6 in cell culture medium using surface plasmon resonance biosensors. *Cytokine.* 2010;51(1):107-11.
92. Martinez-Perdiguero J, Retolaza A, Bujanda L, and Merino S. Surface plasmon resonance immunoassay for the detection of the TNFα biomarker in human serum. *Talanta.* 2014;119(0):492-7.
93. Battaglia TM, Masson JF, Sierks MR, Beaudoin SP, Rogers J, Foster KN, et al. Quantification of cytokines involved in wound healing using surface plasmon resonance. *Anal Chem.* 2005;77(21):7016-23.
94. Anker JN, Hall WP, Lyandres O, Shah NC, Zhao J, and Van Duyne RP. Biosensing with plasmonic nanosensors. *Nat Mater.* 2008;7(6):442-53.
95. Sepulveda B, Angelome PC, Lechuga LM, and Liz-Marzan LM. LSPR-based nanobiosensors. *Nano Today.* 2009;4(3):244-51.
96. Szunerits S, and Boukherroub R. Sensing using localised surface plasmon resonance sensors. *Chem Commun.* 2012;48(72):8999-9010.
97. Guo XW. Surface plasmon resonance based biosensor technique: A review. *J Biophotonics.* 2012;5(7):483-501.
98. Ferhan AR, Jackman JA, Park JH, Cho NJ, and Kim DH. Nanoplasmonic sensors for detecting circulating cancer biomarkers. *Advanced Drug Delivery Reviews.* 2018;125:48-77.
99. Wang YY, Zhou JH, and Li JH. Construction of Plasmonic Nano-Biosensor-Based Devices for Point-of-Care Testing. *Small Methods.* 2017;1:UNSP 1700197.
100. Dutta S, Saikia K, and Nath P. Smartphone based LSPR sensing platform for bio-conjugation detection and quantification. *Rsc Advances.* 2016;6(26):21871-80.
101. Wang YL, X.; Chen, P.; Nhung Thi, T.; Zhang, J.; Chia, W. S.; Boujday, S.; Liedberg, B. Smartphone spectrometer for colorimetric biosensing. *Analyst.* 2016;141(11):3233-8.
102. Wang XC, T.-W.; Lin, G.; Gartia, M. R.; Liu, G. L. Self-Referenced Smartphone-Based Nanoplasmonic Imaging Platform for Colorimetric Biochemical Sensing. *Analytical Chemistry.* 2017;89(1):611-5.
103. Russell SMdlR, R. Paper transducers to detect plasmon variations in colorimetric nanoparticle biosensors. *Sensors and Actuators B-Chemical* 2018;270:327-32.
104. Yesilkoy F, Terborg RA, Pello J, Belushkin AA, Jahani Y, Pruneri V, et al. Phase-sensitive plasmonic biosensor using a portable and large field-of-view interferometric microarray imager. *Light-Science & Applications.* 2018;7:17152.

105. Park Y, Ryu B, Deng QF, Pan BH, Song YJ, Tian YZ, et al. An Integrated Plasmo-Photoelectronic Nanostructure Biosensor Detects an Infection Biomarker Accompanying Cell Death in Neutrophils. *Small.* 2020;16(1).
106. Wang CY, Cai YX, MacLachlan A, and Chen PY. Novel Nanoplasmonic-Structure-Based Integrated Microfluidic Biosensors for Label-Free In Situ Immune Functional Analysis: A review of recent progress. *Ieee Nanotechnol Mag.* 2020;14(2):46-53.
107. Homola J. Surface plasmon resonance sensors for detection of chemical and biological species. *Chem Rev.* 2008;108(2):462-93.
108. Bolduc OR, Live LS, and Masson JF. High-resolution surface plasmon resonance sensors based on a dove prism. *Talanta.* 2009;77(5):1680-7.
109. Chou TH, Chuang CY, and Wu CM. Quantification of Interleukin-6 in cell culture medium using surface plasmon resonance biosensors. *Cytokine.* 2010;51(1):107-11.
110. Martinez-Perdiguero J, Retolaza A, Bujanda L, and Merino S. Surface plasmon resonance immunoassay for the detection of the TNF alpha biomarker in human serum. *Talanta.* 2014;119:492-7.
111. Law WC, Yong KT, Baev A, and Prasad PN. Sensitivity Improved Surface Plasmon Resonance Biosensor for Cancer Biomarker Detection Based on Plasmonic Enhancement. *Acs Nano.* 2011;5(6):4858-64.
112. Regatos D, Sepulveda B, Farina D, Carrascosa LG, and Lechuga LM. Suitable combination of noble/ferromagnetic metal multilayers for enhanced magneto-plasmonic biosensing. *Optics Express.* 2011;19(9):8336-46.
113. Huang T, Nallathamby PD, and Xu XHN. Photostable Single-Molecule Nanoparticle Optical Biosensors for Real-Time Sensing of Single Cytokine Molecules and Their Binding Reactions. *Journal of the American Chemical Society.* 2008;130(50):17095-105.
114. Chiang CY, Hsieh ML, Huang KW, Chau LK, Chang CM, and Lyu SR. Fiber-optic particle plasmon resonance sensor for detection of interleukin-1 beta in synovial fluids. *Biosensors & Bioelectronics.* 2010;26(3):1036-42.
115. Huang YC, Chiang CY, Li CH, Chang TC, Chiang CS, Chau LK, et al. Quantification of tumor necrosis factor-alpha and matrix metalloproteinases-3 in synovial fluid by a fiber-optic particle plasmon resonance sensor. *Analyst.* 2013;138(16):4599-606.
116. Ginsburg GS, and Phillips KA. Precision Medicine: From Science To Value. *Health Aff (Millwood).* 2018;37(5):694-701.
117. Simon R, and Roychowdhury S. Implementing personalized cancer genomics in clinical trials. *Nat Rev Drug Discov.* 2013;12(5):359-70.
118. Seymour CW, Gomez H, Chang CCH, Clermont G, Kellum JA, Kennedy J, et al. Precision medicine for all? Challenges and opportunities for a precision medicine approach to critical illness. *Critical Care.* 2017;21.
119. Evans LE. Progress Toward "Ruling Out" Sepsis. *Critical Care Medicine.* 2018;46(9):1553-4.
120. Calfee CS, Delucchi KL, Sinha P, Matthay MA, Hackett J, Shankar-Hari M, et al. Acute respiratory distress syndrome subphenotypes and differential response to simvastatin: secondary analysis of a randomised controlled trial. *Lancet Respiratory Medicine.* 2018;6(9):691-8.
121. Neelapu SS, Tummala S, Kebriaei P, Wierda W, Gutierrez C, Locke FL, et al. Chimeric antigen receptor T-cell therapy - assessment and management of toxicities. *Nature Reviews Clinical Oncology.* 2018;15(1):47-62.

122. Yelleswarapu V, Buser JR, Haber M, Baron J, Inapuri E, and Issadore D. Mobile platform for rapid sub-picogram-per-milliliter, multiplexed, digital droplet detection of proteins. *Proc Natl Acad Sci U S A.* 2019.
123. Akama K, Shirai K, and Suzuki S. Highly sensitive multiplex protein detection by droplet-free digital ELISA. *Electr Commun Jpn.* 2019;102(2):43-7.
124. Sun J, Hu J, Gou T, Ding X, Song Q, Wu W, et al. Power-free polydimethylsiloxane femtoliter-sized arrays for bead-based digital immunoassays. *Biosens Bioelectron.* 2019;139:111339.
125. Wu Z, Zeng T, Guo WJ, Bai YY, Pang DW, and Zhang ZL. Digital Single Virus Immunoassay for Ultrasensitive Multiplex Avian Influenza Virus Detection Based on Fluorescent Magnetic Multifunctional Nanospheres. *Acs Appl Mater Inter.* 2019;11(6):5762-70.
126. Liu CC, Xu XN, Li B, Situ B, Pan WL, Hu Y, et al. Single-Exosome-Counting Immunoassays for Cancer Diagnostics. *Nano Lett.* 2018;18(7):4226-32.
127. Rissin DM, Fournier DR, Piech T, Kan CW, Campbell TG, Song LA, et al. Simultaneous Detection of Single Molecules and Singulated Ensembles of Molecules Enables Immunoassays with Broad Dynamic Range. *Anal Chem.* 2011;83(6):2279-85.
128. Lipták BlG. *Instrument engineers' handbook.* Boca Raton, FL: CRC Press; 2003.
129. Duan XX, Li Y, Rajan NK, Routenberg DA, Modis Y, and Reed MA. Quantification of the affinities and kinetics of protein interactions using silicon nanowire biosensors. *Nature Nanotechnology.* 2012;7(6):401-7.
130. Dinh TL, Ngan KC, Shoemaker CB, and Walt DR. Using Antigen-antibody Binding Kinetic Parameters to Understand Single-Molecule Array Immunoassay Performance. *Anal Chem.* 2016;88(23):11335-9.
131. Hay KA, Hanafi LA, Li D, Gust J, Liles WC, Wurfel MM, et al. Kinetics and biomarkers of severe cytokine release syndrome after CD19 chimeric antigen receptor-modified T-cell therapy. *Blood.* 2017;130(21):2295-306.
132. Teachey DT, Lacey SF, Shaw PA, Melenhorst JJ, Maude SL, Frey N, et al. Identification of Predictive Biomarkers for Cytokine Release Syndrome after Chimeric Antigen Receptor T-cell Therapy for Acute Lymphoblastic Leukemia. *Cancer Discovery.* 2016;6(6):664-79.
133. Jin H, Liu Z, Xiao Y, Fan X, Yan J, and Liang H. Prediction of sepsis in trauma patients. *Burns Trauma.* 2014;2(3):106-13.
134. Li YQ, Liu BL, Fukudome EY, Lu J, Chong W, Jin G, et al. Identification of citrullinated histone H3 as a potential serum protein biomarker in a lethal model of lipopolysaccharide-induced shock. *Surgery.* 2011;150(3):442-51.
135. Lee DW, Gardner R, Porter DL, Louis CU, Ahmed N, Jensen M, et al. Current concepts in the diagnosis and management of cytokine release syndrome. *Blood.* 2014;124(2):188-95.
136. Chen F, Teachey DT, Pequignot E, Frey N, Porter D, Maude SL, et al. Measuring IL-6 and sIL-6R in serum from patients treated with tocilizumab and/or siltuximab following CAR T cell therapy. *J Immunol Methods.* 2016;434:1-8.
137. Hudson TJ, Anderson W, Aretz A, Barker AD, Bell C, Bernabe RR, et al. International network of cancer genome projects. *Nature.* 2010;464(7291):993-8.
138. Pan BH, Alam HB, Chong W, Mobley J, Liu BL, Deng QF, et al. CitH3: a reliable blood biomarker for diagnosis and treatment of endotoxic shock. *Sci Rep-Uk.* 2017;7.

139. Li YQ, Liu ZC, Liu BL, Zhao T, Chong W, Wang YM, et al. Citrullinated histone H3: A novel target for the treatment of sepsis. *Surgery.* 2014;156(2):229-34.
140. Sarma A, Calfee CS, and Ware LB. Biomarkers and Precision Medicine: State of the Art. *Crit Care Clin.* 2020;36(1):155-65.
141. van der Poll T, van de Veerdonk FL, Scicluna BP, and Netea MG. The immunopathology of sepsis and potential therapeutic targets. *Nat Rev Immunol.* 2017;17(7):407-20.
142. Wong HR, Cvijanovich N, Wheeler DS, Bigham MT, Monaco M, Odoms K, et al. Interleukin-8 as a stratification tool for interventional trials involving pediatric septic shock. *Am J Resp Crit Care.* 2008;178(3):276-82.
143. Faix JD. Biomarkers of sepsis. *Crit Rev Clin Lab Sci.* 2013;50(1):23-36.
144. Kibe S, Adams K, and Barlow G. Diagnostic and prognostic biomarkers of sepsis in critical care. *J Antimicrob Chemother.* 2011;66 Suppl 2:ii33-40.
145. Schuetz P, Wirz Y, Sager R, Christ-Crain M, Stolz D, Tamm M, et al. Effect of procalcitonin-guided antibiotic treatment on mortality in acute respiratory infections: a patient level meta-analysis. *Lancet Infect Dis.* 2018;18(1):95-107.
146. Chen N, Zhou M, Dong X, Qu J, Gong F, Han Y, et al. Epidemiological and clinical characteristics of 99 cases of 2019 novel coronavirus pneumonia in Wuhan, China: a descriptive study. *Lancet.* 2020;395(10223):507-13.
147. Cohen L, and Walt DR. Highly Sensitive and Multiplexed Protein Measurements. *Chem Rev.* 2019;119(1):293-321.
148. Jing WW, Wang Y, Yang YZ, Wang Y, Ma GZ, Wang SP, et al. Time-Resolved Digital Immunoassay for Rapid and Sensitive Quantitation of Procalcitonin with Plasmonic Imaging. *Acs Nano.* 2019;13(8):8609-17.
149. Reddy B, Hassan U, Seymour C, Angus DC, Isbell TS, White K, et al. Point-of-care sensors for the management of sepsis. *Nat Biomed Eng.* 2018;2(9):640-8.
150. Rivnak AJ, Rissin DM, Kan CW, Song LA, Fishburn MW, Piech T, et al. A fully-automated, six-plex single molecule immunoassay for measuring cytokines in blood. *J Immunol Methods.* 2015;424:20-7.
151. Rissin DM, Kan CW, Song LN, Rivnak AJ, Fishburn MW, Shao QC, et al. Multiplexed single molecule immunoassays. *Lab Chip.* 2013;13(15):2902-11.
152. Hu ZM, Fang WB, Gou T, Wu WS, Hu JM, Zhou SF, et al. A novel method based on a Mask R-CNN model for processing dPCR images. *Anal Methods-Uk.* 2019;11(27):3410-8.
153. Gou T, Hu JM, Zhou SF, Wu WS, Fang WB, Sun JJ, et al. A new method using machine learning for automated image analysis applied to chip-based digital assays. *Analyst.* 2019;144(10):3274-81.
154. Henley WH, Dennis PJ, and Ramsey JM. Fabrication of Microfluidic Devices Containing Patterned Microwell Arrays. *Anal Chem.* 2012;84(3):1776-80.
155. Huang N-T, Hwong Y-J, and Lai RL. A microfluidic microwell device for immunomagnetic single-cell trapping. *Microfluidics and Nanofluidics.* 2018;22(2):16.
156. Akama K, Iwanaga N, Yamawaki K, Okuda M, Jain K, Ueno H, et al. Wash- and Amplification-Free Digital Immunoassay Based on Single-Particle Motion Analysis. *Acs Nano.* 2019;13(11):13116-26.
157. Maude SL, Laetsch TW, Buechner J, Rives S, Boyer M, Bittencourt H, et al. Tisagenlecleucel in Children and Young Adults with B-Cell Lymphoblastic Leukemia. *N Engl J Med.* 2018;378(5):439-48.

158. Neelapu SS, Locke FL, Bartlett NL, Lekakis LJ, Miklos DB, Jacobson CA, et al. Axicabtagene Ciloleucel CAR T-Cell Therapy in Refractory Large B-Cell Lymphoma. *N Engl J Med.* 2017;377(26):2531-44.
159. Kotch C, Barrett D, and Teachey DT. Tocilizumab for the treatment of chimeric antigen receptor T cell-induced cytokine release syndrome. *Expert Rev Clin Immunol.* 2019;15(8):813-22.
160. Mehta P, McAuley DF, Brown M, Sanchez E, Tattersall RS, Manson JJ, et al. COVID-19: consider cytokine storm syndromes and immunosuppression. *Lancet.* 2020;395(10229):1033-4.
161. Moore JB, and June CH. Cytokine release syndrome in severe COVID-19. *Science.* 2020;368(6490):473-4.
162. Griffin G, Shenoi S, and Hughes GC. Hemophagocytic lymphohistiocytosis: An update on pathogenesis, diagnosis, and therapy. *Best Pract Res Clin Rheumatol.* 2020:101515.
163. Alcamo AM, Pang D, Bashir DA, Carcillo JA, Nguyen TC, and Aneja RK. Role of Damage-Associated Molecular Patterns and Uncontrolled Inflammation in Pediatric Sepsis-Induced Multiple Organ Dysfunction Syndrome. *J Pediatr Intensive Care.* 2019;8(1):25-31.
164. Mehta P, Cron RQ, Hartwell J, Manson JJ, and Tattersall RS. Silencing the cytokine storm: the use of intravenous anakinra in haemophagocytic lymphohistiocytosis or macrophage activation syndrome. *Lancet Rheumatol.* 2020.
165. Giamarellos-Bourboulis EJ, Netea MG, Rovina N, Akinosoglou K, Antoniadou A, Antonakos N, et al. Complex Immune Dysregulation in COVID-19 Patients with Severe Respiratory Failure. *Cell Host Microbe.* 2020.
166. . clinicaltrials.gov.
167. Araci IE, Robles M, and Quake SR. A reusable microfluidic device provides continuous measurement capability and improves the detection limit of digital biology. *Lab Chip.* 2016;16(9):1573-8.
168. Chen PY, Huang NT, Chung MT, Cornell TT, and Kurabayashi K. Label-free cytokine micro- and nano-biosensing towards personalized medicine of systemic inflammatory disorders. *Adv Drug Deliver Rev.* 2015;95:90-103.
169. Vlachopoulou ME, Tserepi A, Pavli P, Argitis P, Sanopoulou M, and Misiakos K. A low temperature surface modification assisted method for bonding plastic substrates. *J Micromech Microeng.* 2009;19(1).
170. Song Y, Ye Y, Su S-H, Stephens A, Cai T, Chung M-T, et al. A Digital Protein Microarray for COVID-19 Cytokine Storm Monitoring. *medRxiv.* 2020.
171. Pino CJ, Westover AJ, Johnston KA, Buffington DA, and Humes HD. Regenerative Medicine and Immunomodulatory Therapy: Insights From the Kidney, Heart, Brain, and Lung. *Kidney Int Rep.* 2018;3(4):771-83.
172. Yessayan L, Szamosfalvi B, Napolitano L, Singer B, Kurabayashi K, Song Y, et al. Treatment of Cytokine Storm in COVID-19 Patients with Immunomodulatory Therapy. *ASAIO Journal.* 2020;Online First.
173. Nishimoto N, Terao K, Mima T, Nakahara H, Takagi N, and Kakehi T. Mechanisms and pathologic significances in increase in serum interleukin-6 (IL-6) and soluble IL-6 receptor after administration of an anti-IL-6 receptor antibody, tocilizumab, in patients with rheumatoid arthritis and Castleman disease. *Blood.* 2008;112(10):3959-64.

174. Mayer KM, and Hafner JH. Localized Surface Plasmon Resonance Sensors. *Chem Rev.* 2011;111(6):3828-57.
175. Petryayeva E, and Krull UJ. Localized surface plasmon resonance: Nanostructures, bioassays and biosensing-A review. *Anal Chim Acta.* 2011;706(1):8-24.
176. Estevez MC, Otte MA, Sepulveda B, and Lechuga LM. Trends and challenges of refractometric nanoplasmonic biosensors: A review. *Anal Chim Acta.* 2014;806:55-73.
177. Unser S, Bruzas I, He J, and Sagle L. Localized Surface Plasmon Resonance Biosensing: Current Challenges and Approaches. *Sensors-Basel.* 2015;15(7):15684-716.
178. Ament I, Prasad J, Henkel A, Schmachtel S, and Sonnichsen C. Single Unlabeled Protein Detection on Individual Plasmonic Nanoparticles. *Nano Lett.* 2012;12(2):1092-5.
179. Zijlstra P, Paulo PMR, and Orrit M. Optical detection of single non-absorbing molecules using the surface plasmon resonance of a gold nanorod. *Nat Nanotechnol.* 2012;7(6):379-82.
180. Beuwer MA, Prins MWJ, and Zijlstra P. Stochastic Protein Interactions Monitored by Hundreds of Single-Molecule Plasmonic Biosensors. *Nano Lett.* 2015;15(5):3507-11.
181. Acimovic SS, Ortega MA, Sanz V, Berthelot J, Garcia-Cordero JL, Renger J, et al. LSPR Chip for Parallel, Rapid, and Sensitive Detection of Cancer Markers in Serum. *Nano Lett.* 2014;14(5):2636-41.
182. Oh BR, Chen PY, Nidetz R, McHugh W, Fu JP, Shanley TP, et al. Multiplexed Nanoplasmonic Temporal Profiling of T-Cell Response under Immunomodulatory Agent Exposure. *Acs Sensors.* 2016;1(7):941-8.
183. Huang PH, Xie YL, Ahmed D, Rufo J, Nama N, Chen YC, et al. An acoustofluidic micromixer based on oscillating sidewall sharp-edges. *Lab Chip.* 2013;13(19):3847-52.
184. Oh J, Hart R, Capurro J, and Noh H. Comprehensive analysis of particle motion under non-uniform AC electric fields in a microchannel. *Lab Chip.* 2009;9(1):62-78.
185. Ahmed D, Mao XL, Shi JJ, Juluri BK, and Huang TJ. A millisecond micromixer via single-bubble-based acoustic streaming. *Lab Chip.* 2009;9(18):2738-41.
186. Hellman AN, Rau KR, Yoon HH, Bae S, Palmer JF, Phillips KS, et al. Laser-induced mixing in microfluidic channels. *Anal Chem.* 2007;79(12):4484-92.
187. Morgan H, and Green NG. *AC electrokinetics : colloids and nanoparticles.* Philadelphia, PA: Research Studies Press; 2003.
188. Castellanos A, Ramos A, Gonzalez A, Green NG, and Morgan H. Electrohydrodynamics and dielectrophoresis in microsystems: scaling laws. *J Phys D Appl Phys.* 2003;36(20):2584-97.
189. Sigurdson M, Wang DZ, and Meinhart CD. Electrothermal stirring for heterogeneous immunoassays. *Lab Chip.* 2005;5(12):1366-73.
190. Song Y, Goto K, Stephens A, Chung MT, Park YG, and Kurabayashi K. *2017 19th International Conference on Solid-State Sensors, Actuators and Microsystems (TRANSDUCERS).* IEEE; 2017:858-61.
191. Gong JR. Label-Free Attomolar Detection of Proteins Using Integrated Nanoelectronic and Electrokinetic Devices. *Small.* 2010;6(8):967-73.
192. Cheng IF, Yang HL, Chung CC, and Chang HC. A rapid electrochemical biosensor based on an AC electrokinetics enhanced immuno-reaction. *Analyst.* 2013;138(16):4656-62.
193. Wang MS, Zhao CL, Miao XY, Zhao YH, Rufo J, Liu YJ, et al. Plasmofluidics: Merging Light and Fluids at the Micro-/Nanoscale. *Small.* 2015;11(35):4423-44.

194. Nusz GJ, Curry AC, Marinakos SM, Wax A, and Chilkoti A. Rational Selection of Gold Nanorod Geometry for Label-Free Plasmonic Biosensors. *Acs Nano.* 2009;3(4):795-806.
195. Petrova H, Juste JP, Pastoriza-Santos I, Hartland GV, Liz-Marzan LM, and Mulvaney P. On the temperature stability of gold nanorods: comparison between thermal and ultrafast laser-induced heating. *Phys Chem Chem Phys.* 2006;8(7):814-21.
196. Ramos A, Morgan H, Green NG, and Castellanos A. AC electric-field-induced fluid flow in microelectrodes. *J Colloid Interf Sci.* 1999;217(2):420-2.
197. Thielicke W, and Stamhuis E. PIVlab–towards user-friendly, affordable and accurate digital particle image velocimetry in MATLAB. *Journal of Open Research Software.* 2014;2(1).
198. Green NG, Ramos A, Gonzalez A, Morgan H, and Castellanos A. Fluid flow induced by nonuniform ac electric fields in electrolytes on microelectrodes. I. Experimental measurements. *Phys Rev E.* 2000;61(4):4011-8.
199. Nam H, Oh BR, Chen PY, Chen MK, Wi SJ, Wan WJ, et al. Multiple MoS2 Transistors for Sensing Molecule Interaction Kinetics. *Sci Rep-Uk.* 2015;5.
200. Shiddiky MJA, Vaidyanathan R, Rauf S, Tay Z, and Trau M. Molecular Nanoshearing: An Innovative Approach to Shear off Molecules with AC-Induced Nanoscopic Fluid Flow. *Sci Rep-Uk.* 2014;4.
201. Dinarello CA. Interleukin-1 and Interleukin-1 Antagonism. *Blood.* 1991;77(8):1627-52.
202. Press WH, Flannery BP, Teukolsky SA, Vetterling WT, and Kramer PB. AIP; 1987.
203. . SoftMax® Pro Microplate Software User Manual http://mdc.custhelp.com/app/answers/detail/a_id/19550.
204. Stephens A, Nidetz R, Mesyngier N, Chung MT, Song YJ, Fu JP, et al. Mass-producible microporous silicon membranes for specific leukocyte subset isolation, immunophenotyping, and personalized immunomodulatory drug screening in vitro. *Lab Chip.* 2019;19(18):3065-76.
205. Raphael M, Christodoulides J, Delehanty J, Long J, and Byers J. Quantitative Imaging of Protein Secretions from Single Cells in Real Time. *Biophys J.* 2014;106(2):607a-a.
206. Bhalla N, Pan Y, Yang Z, and Payam AF. Opportunities and Challenges for Biosensors and Nanoscale Analytical Tools for Pandemics: COVID-19. *ACS nano.* 2020.
207. . REGENERON AND SANOFI PROVIDE UPDATE ON U.S. PHASE 2/3 ADAPTIVE-DESIGNED TRIAL OF KEVZARA® (SARILUMAB) IN HOSPITALIZED COVID-19 PATIENTS. https://newsroom.regeneron.com/index.php/news-releases/news-release-details/regeneron-and-sanofi-provide-update-us-phase-23-adaptive.
208. Smith S, Mager D, Perebikovsky A, Shamloo E, Kinahan D, Mishra R, et al. CD-Based Microfluidics for Primary Care in Extreme Point-of-Care Settings. *Micromachines-Basel.* 2016;7(2).
209. Strohmeier O, Keller M, Schwemmer F, Zehnle S, Mark D, von Stetten F, et al. Centrifugal microfluidic platforms: advanced unit operations and applications. *Chem Soc Rev.* 2015;44(17):6187-229.
210. Tang MH, Wang GH, Kong SK, and Ho HP. A Review of Biomedical Centrifugal Microfluidic Platforms. *Micromachines-Basel.* 2016;7(2).